Spectroscopic Investigations of Functional Bulk and Thin Film Heusler Alloys

Dissertation zur Erlangung des Grades
Doktor der Naturwissenschaften
am Fachbereich Physik
der Johannes Gutenberg-Universität Mainz

Peter Klaer
geb. in Bielsko-Biala (Schlesien)

JOHANNES GUTENBERG
UNIVERSITÄT MAINZ

Mainz, 2012

1. Berichterstatter:

2. Berichterstatter:

Tag der mündlichen Prüfung: 15.Juni 2012

Die Forschung lebt vom Austausch des Wissens.

Albert Einstein

Kurzfassung

Funktionale und smarte Materialien haben in der heutigen Forschung und Entwicklung einen sehr hohen Stellenwert erreicht. Eine wichtige Klasse von funktionalen Materialien bilden die sogenannten Heusler Verbindungen, welche unter anderem in der Spintronik, Thermoelektrik oder als Formgedächtnislegierung eine Anwendung finden. Ein wichtiger Aspekt von funktionalen Materialien ist die Anpassungsfähigkeit ihrer physikalischer Eigenschaften.

In dieser Arbeit sind elektronische und magnetische Eigenschaften für funktionale polykristalline Volumenproben und einkristalline Filme von Heusler-Legierungen mittels spektroskopischer Untersuchungsmethoden, magnetischer Röntgenzirkulardichroismus (XMCD) und eine energiedispersive Röntgenanalyse (EDX), bestimmt worden.

Mit der energiedispersiven Röntgenanalyse wurde die Homogenität der Proben untersucht. Einige quarternäre Proben, wie zum Beipiel $Co_2(Mn_xTi_{1-x})Sn$ und $Co_2(Mn_{0.5}Dy_{0.5})Sn$ zeigen eine interessante Phasenentmischung in zwei nahezu vollständig separierte ternäre Phasen. Bei den genannten Verbindungen führt die beobachtete Phasenseparation zu einer Verbesserung der thermoelektrischen Effizienz.

Mit der Hauptuntersuchungsmethode XMCD sind Co_2TiZ (Z = Si, Ge, Sn, and Sb), $Co_2(Mn_xTi_{1-x})Si$, $Co_2(Mn_xTi_{1-x})Ge$ und $Co_2Mn(Ga_{1-x}Ge_x)$ Heusler Legierungen untersucht worden. Einige dieser Co-basierten Verbindungen sind laut theoretischen Vorhersagen halbmetalische Ferromagnete, d.h. sie besitzen an der Fermi-Energie eine Bandlücke für Minoritätselektronen. Neben der Bestimmung der elementspezifischen magnetischen Momente wird auch die elektronische spinabhängige unbesetzte Zustandsdichte aus den Messdaten abgeleitet. Durch die gezielte Veränderung der Zusammensetzung kann eine systematische Veränderung der magnetischen Momente und eine Verschiebung der Fermi-Energie in der Minoritäts-Bandlücke festgestellt werden, die von *ab initio* Rechnungen vorhergesagt wurden. Das ist ein experimenteller Beweis, dass sich Heusler Legierungen für eine kontrollierte Einstellung von physikalischen Eigenschaften eignen. Die Messungen geben starke experimentelle Hinweise auf eine Bandlücke für Minoritäts-Elektronen und bestätigen damit theoretische Vorhersagen.

Darüber hinaus werden Messungen an CoFeMnZ (Z = Al, Ga; Si, Ge) mit 1:1:1:1 Zusammensetzung, die den Heusler Verbindungen sehr verwandt sind, diskutiert. Diese quaternären Verbindungen erweitern die ohnehin schon sehr große Palette ternärer Heusler-Legierungen.

Bei den epitaktischen Co_2FeAl und Mn_2VAl Filmen wurde eine volumen- und oberflächensensitve XMCD Untersuchungsmethode angewendet. Damit können Unterschiede von Oberflächen- und Volumeneigenschaften festgestellt werden, die unter anderem auf die Probenherstellung zurückzuführen sind. Anhand von temperaturabhängigen Messungen wird ein Vielteilchen-Modell diskutiert, das eine mögliche Erklärung für die starke Temperaturabhängigkeit der Spinpolarisation von Heusler-Legierungen gibt.

Temperatur- und winkelabhängige XMCD Messungen an Ni_2MnGa liefern ein vertieftes Verständnis für die große Kristallanisotropie, die für den ferromagnetischen 'Shape Memory' Effekt eine notwendige Bedingung ist. Die winkelabhängigen XMCD Messungen in der Martensitphase zeigen eine spektrale Veränderung, die durch die Rotation der Magnetisierung von der leichten in die schwere magnetische Achse verursacht wird. Dabei werden elektronische Zustände zu höheren kinetischen Energien verschoben, was die freie Energie des Systems anhebt und unmittelbare Ursache der magnetischen Anisotropie ist.

Der Vergleich der spektroskopischen Ergebnisse mit der Theorie, wie es in der gesamten Arbeit durchgeführt wird, ist ein Schlüssel um komplexe Materialen besser zu verstehen und funktionale Materialien wie die Heusler-Legierungen zu optimieren.

Abstract

Functional and smart materials have gained large scientific and practical interest in current research and development. The so-called Heusler alloys form an important class of functional materials used in spintronics, thermoelectrics, or for shape memory alloy applications. An important aspect of functional materials is the adaptability of their physical properties.

In this work functional polycrystalline bulk and epitaxial thin film Heusler alloys are characterized by means of spectroscopic investigation methods, X-ray magnetic circular dichroism (XMCD) and energy dispersive X-ray analysis (EDX).

With the EDX analysis the homogeneity of the samples is studied extensively and for some cases of quaternary compounds, for example $\mathrm{Co_2(Mn_xTi_{1-x})Sn}$ and $\mathrm{Co_2(Mn_{0.5}Dy_{0.5})Sn}$, an interesting phase separation in two nearly pure ternary Heusler phases is formed. For these samples the phase separation leads to an improvement of thermoelectric properties.

XMCD as the main investigation method is used to study $\mathrm{Co_2Ti}Z$ (Z = Si, Sn, and Sb), $\mathrm{Co_2(Mn_xTi_{1-x})Si}$, $\mathrm{Co_2(Mn_xTi_{1-x})Ge}$ and $\mathrm{Co_2Mn(Ga_{1-x}Ge_x)}$ Heusler compounds. Some of these Co-based Heusler alloys are promising half-metallic ferromagnets as predicted by theory, i.e., they show a band gap at the Fermi energy for one of the two spin channels. In addition to the evaluation of the element-specific magnetic moments for the constituents, the spin-resolved unoccupied density of states is determined. A systematic change of the magnetic moments and a shift of the Fermi energy in the minority band gap is measured in accordance with *ab initio* calculations by selective variation of the composition. This is a proof that Heusler alloys are suitable for a controlled tailoring of physical properties. A strong experimental indication of the existence of half-metallicity results from deconvolution of XMCD spectra in the case of $\mathrm{Co_2MnSi}$.

Results of CoFeMnZ (Z = Al, Ga; Si, Ge) compounds with 1:1:1:1 composition, resembling the Heusler $L2_1$ structure, are presented and discussed. These potential half-metallic ferromagnetic materials extend the class of intermetallic spintronic materials.

For the epitaxial Heusler films of the alloys $\mathrm{Co_2FeAl}$ and $\mathrm{Mn_2VAl}$ a bulk and surface sensitive XMCD investigation method is applied. Differences of the surface and bulk properties occurring in a few cases can be traced back to the deposition process. XMCD measurements support a many-body model that predicts the occurrence of non-quasiparticles states near the Fermi energy. The experimental results thus may explain the yet unexplained strong temperature dependence of the spin polarization in Heusler alloys.

Temperature and angular-dependent XMCD measurements of $\mathrm{Ni_2MnGa}$ provide an understanding of the large magnetic anisotropy which is a necessary condition for the magnetic shape memory effect. The angular dependence of XMCD spectra measured in the martensitic phase shows a spectral change upon rotation of the magnetization from the easy axis into the hard axis. The spectral change indicates a shift of electronic states with d_{z^2} symmetry towards higher energy, which increases the total energy of the system.

The comparison of the experimental results with theoretical results as it is carried out extensively in this thesis is a key to improve the understanding of complex materials and to optimize functional materials like the Heusler alloys.

Publications

Publications included in this thesis

- *Tailoring the electronic structure of half-metallic Heusler alloys*
  P. Klaer, M. Kallmayer, C. G. F. Blum, T. Graf, J. Barth, B. Balke, G. H. Fecher, C. Felser, and H. J. Elmers: Phys. Rev. B, 80:144405, 2009.

- *Charge transfer and tunable minority band gap at the Fermi energy of a quaternary* $Co_2(Mn_xTi_{1-x})Ge$ *Heusler alloy*
  P. Klaer, T. Bos, M. Kallmayer, C. G. F. Blum, T. Graf, J. Barth, B. Balke, G. H. Fecher, C. Felser, and H. J. Elmers: Phys. Rev. B, 82:104410, 2010.

- *Temperature dependence of X-ray absorption spectra in the ferromagnetic Heusler alloys* Mn_2VAl *and* Co_2FeAl
  P. Klaer, E. Arbelo-Jorge, M. Jourdan, W. H. Wang, H. Sukegawa, K. Inomata, and H. J. Elmers: Phys. Rev. B, 82:024418, 2010.

- *Microscopic origin of magnetic anisotropy in martensitic* Ni_2MnGa
  P. Klaer, T. Eichhorn, G. Jakob, and H. J. Elmers: Phys. Rev. B, 83:214419, 2011.

- *Element-specific magnetic moments and spin-resolved density of states in CoFeMnZ (Z = Al, Ga; Si, Ge)*
  P. Klaer, B. Balke, V. Alijani, J. Winterlik, G. H. Fecher, C. Felser, and H. J. Elmers: Phys. Rev. B, 84:144413, 2011.

- *Thermomagnetic properties improved by self-organized flower-like phase separation of ferromagnetic* $Co_2Dy_{0.5}Mn_{0.5}Sn$
  M. Schwall, L. M. Schoop, S. Ouardi, B. Balke, C. Felser, P. Klaer, and H. J. Elmers: Advanced Functional Materials, published online, 2012.

Publications related to this thesis

- *Localized magnetic moments in the Heusler alloy* Rh_2MnGe
  P. Klaer, M. Kallmayer, H. J. Elmers, L. Basit, J. Thöne, S. Chadov, and C. Felser: J. Phys. D, 42:084001, 2009.

- *Spin-resolved unoccupied density of states in epitaxial Heusler-alloy films*
  M. Kallmayer, P. Klaer, H. Schneider, E. Arbelo-Jorge, C. Herbort, G. Jakob, M. Jourdan, and H. J. Elmers: Phys. Rev. B, 80:020406(R), 2009.

- *Full tunability of strain along the fcc-bcc bain path in epitaxial films and consequences for magnetic properties*
  J. Buschbeck, I. Opahle, M. Richter, U. K. Rößler, P. Klaer, M. Kallmayer, H. J. Elmers, G. Jakob, L. Schultz, and S. Fähler: Phys. Rev. Lett., 103:216101, 2009.

- *Interface and bulk magnetism of $Co_2Cr_{0.6}Fe_{0.4}Al$ and Co_2CrAl thin films*
  M. Jourdan, E. Arbelo-Jorge, C. Herbort, M. Kallmayer, P. Klaer, and H. J. Elmers: Appl. Phys. Lett., 95:172504, 2009.

- *Phase-separation-induced changes in the magnetic and transport properties of the quaternary Heusler alloy $Co_2Mn_{1-x}Ti_xSn$*
  T. Graf, J. Barth, C. G. F. Blum, B. Balke, C. Felser, P. Klaer, and H. J. Elmers: Phys. Rev. B, 82:194420, 2010.

- *Phase separation in the quaternary Heusler compound $CoTi_{(1-x)}Mn_xSb$ - A reduction in the thermal conductivity for thermoelectric applications*
  T. Graf, P. Klaer, J. Barth, B. Balke, H. J. Elmers, and C. Felser: Scripta Materialia, 63:1216, 2010.

- *Magnetic and structural properties of $Co_2FeAl_{1-x}Si_x$ thin films*
  E. Arbelo-Jorge, M. Jourdan, M. Kallmayer, P. Klaer, and H. J. Elmers: J. Phys. Conf. Ser., 200:072006, 2010.

- *Itinerant half-metallic ferromagnets Co_2TiZ (Z = Si, Ge, Sn): Ab initio calculations and measurement of the electronic structure and transport properties*
  J. Barth, G. H. Fecher, B. Balke, S. Ouardi, T. Graf, C. Felser, A. Shkabko, A. Weidenkaff, P. Klaer, H. J. Elmers, H. Yoshikawa, S. Ueda, and K. Kobayashi: Phys. Rev. B, 81:064404, 2010.

- *Anomalous transport properties of the half-metallic ferromagnets Co_2TiSi, Co_2TiGe and Co_2TiSn*
  J. Barth, G. H. Fecher, B. Balke, T. Graf, A. Shkabko, A. Weidenkaff, P. Klaer, M. Kallmayer, H. J. Elmers, H. Yoshikawa, S. Ueda, K. Kobayashi, and C. Felser: Phil. Trans. R. Soc. A, 369:3588, 2011.

- *Effect of annealing on $Co_2FeAl_{0.5}Si_{0.5}$ thin films: A magneto-optical and X-ray absorption study*
  S. Trudel, W. Georg, J. Hamrle, B. Hillebrands, P. Klaer, M. Kallmayer, H. J. Elmers, H. Sukegawa, W. Wang, and K. Inomata: Phys. Rev. B, 83:104412, 2011.

- *Element-specific magnetic properties of $Co_2(Mn_{1-x}Fe_x)Si$ films probed by X-ray magnetic circular/linear dichroism*
  M. Kallmayer, P. Klaer, H. Schneider, G. Jakob, H. J. Elmers, D. Legut, and P. M. Oppeneer: Phys. Rev. B, 84:054448, 2011.

- *Element-specific ferromagnetic resonance in epitaxial Heusler spin valve systems*
  P. Klaer, F. Hoffmann, G. Woltersdorf, E. Arbelo-Jorge, M. Jourdan, C. H. Back, and H. J. Elmers: J. Phys. D, 44:425004, 2011.

- *Disentangling the Mn moments on different sublattices in the half-metallic ferrimagnet $Mn_{3-x}Co_xGa$*
  P. Klaer, C. A. Jenkins, V. Alijani, J. Winterlik, B. Balke, C. Felser, and H. J. Elmers: Appl. Phys. Lett., 98:212510, 2011.

Conference contributions

- *Half-metallic band structure of Co_2TiZ (Z = Si, Ge, and Sn) detected by XMCD*
  P. Klaer, M. Kallmayer, T. Methfessel, B. Balke, J. Barth, T. Graf, G. H. Fecher, C. Felser, and H. J. Elmers: 424. WE-Heraeus-Seminar, *Magnetism meets Semiconductors*, Bad Honnef, 2009, Poster

- *X-ray absorption spectroscopy of half-metallic Co_2TiZ (Z = Si, Ge and Sn)*
  P. Klaer, M. Kallmayer, B. Balke, J. Barth, T. Graf, G. H. Fecher, C. Felser, and H. J. Elmers: DPG Frühjahrstagung, Dresden 2009, Poster

- *XMCD as probe for unoccupied spin-resolved partial DOS measured on (half-metallic) Heusler compounds*
  P. Klaer, M. Kallmayer, C. G. F. Blum, T. Graf, B. Balke, J. Barth, G. H. Fecher, C. Felser, and H. J. Elmers: 437. WE-Heraeus-Seminar, *Photons and Neutrons as Probes of Matter*, Bad Honnef 2009, Poster/Talk

- *XMCD as a probe for spin-orbit interaction and spin-resolved electronic structure of Heusler compounds*
  P. Klaer, M. Kallmayer, E. Arbelo-Jorge, C. Herbort, G. Jakob, M. Jourdan, C. G. F. Blum, T. Graf, B. Balke, G. H. Fecher, C. Felser, and H. J. Elmers: DPG Frühjahrstagung, Regensburg, 2010, Talk

- *Microscopic origin of magnetic anisotropy in martensitic Ni_2MnGa*
  P. Klaer, T. Eichhorn, G. Jakob, and H. J. Elmers: DPG Frühjahrstagung, Dresden, 2011, Talk

- *Element-specific magnetic moments and spin-resolved DOS of the half-metallic compounds CoFeMnZ (Z = Al, Ga; Si, Ge)*
  P. Klaer, A. Vajiheh, B. Balke, G. H. Fecher, C. Felser, and H. J. Elmers, DPG Frühjahrstagung, Dresden, 2011, Poster

- *Transfer of angular momentum by circularly polarized near fields*
  P. Klaer, F. Schertz, M. Schmelzeisen, R. Mohammadi, H. J. Elmers, G. Schönhense, H. J. Butt, and M. Kreiter: *SPP 1391: Ultrafast nanooptics*, Bad Honnef, 2011, Poster

- *Transfer of angular momentum by circularly polarized near fields*
  P. Klaer, F. Schertz, K. Krewer, G. Schönhense, H. J. Elmers: DPG Frühjahrstagung, Berlin, 2012, Poster

Contents

Chapter 1

Introduction

Functional and smart materials have excited great scientific interest. They are composed for sensing, processing, actuating with designed physical properties. Heusler alloys represent a unique class of materials that are very useful as smart materials. In many cases Heusler alloys show ferromagnetic, superconductive, magneto-optical, semiconductor, heavy-fermion, and topological insulator properties that enable applications in spintronic, shape memory, superconducting, thermoelectric, and spincaloric devices. [vJS04, FFB07, GFP11] The most important feature of Heusler compounds is that they open a way to tailor physical properties via band-structure tuning realized by partial substitution of elements or by adding small amounts of elements keeping the original crystal structure intact. [FKW+05, ÖAGS07, FFB07, CSA+08, WSSI08]

This thesis presents the spectroscopical method X-ray magnetic circular dichroism (XMCD) in X-ray absorption (XAS) to investigate the element-specific electronic properties and the element-specific magnetic orbital and spin moments of ternary and quaternary Heulser compounds. Results for polycrystalline bulk samples and epitaxial thin film samples will be discussed. As it will be shown, measurements on quaternary Heusler alloy series with a selective atom replacement provide the possibility to tailor and to design desired physical properties. The experimental results presented in this thesis in comparison with theoretical predictions lead to an improved understanding of magnetic and electronic properties of Heusler alloys.

Beside XMCD, the spectroscopical energy dispersive X-ray analysis (EDX) method is used to determine the sample quality of the Heusler alloys. The EDX detector in combination with a scanning electron microscope (SEM) allows element-specific surface mappings of the sample constituents and provides information about the phase homogeneity.

Heusler alloys

In 1903 F. Heusler discovered [Heu03] the ferromagnetic Cu_2MnAl alloy consisting of non-ferromagnetic elements as the prototype for Heusler alloys. Since than about one thousand different Heusler compounds have been reported. [GD08] Heusler compounds crystallize by definition in the cubic $L2_1$ structure (space group $Fm\bar{3}m$) as shown in Fig. 1.1. They are mostly ternary compounds with

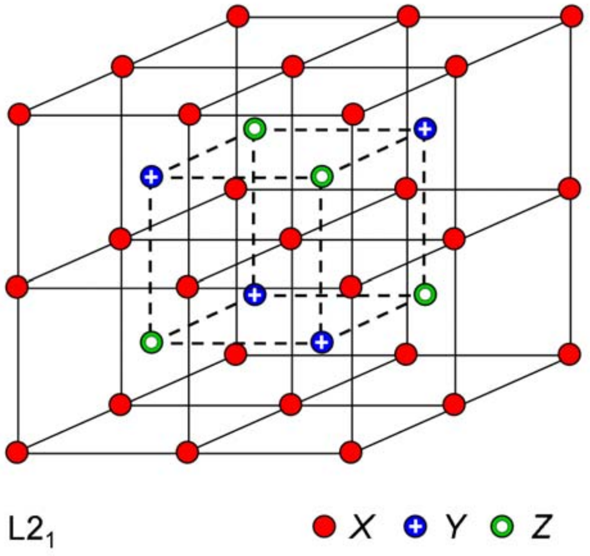

Figure 1.1: Cubic L2$_1$ Heusler crystal structure with a chemical formula X_2YZ. Please note, that all positions are shifted by (1/4 , 1/4 , 1/4) with respect to the standard $Fm\bar{3}m$ cell.

the general chemical formula X_2YZ. X, Y are transition metals, and Z is a main group element placed on the Wyckoff position 8c (1/4, 1/4, 1/4), 4a (0, 0, 0) and 4b (1/2, 1/2, 1/2), respectively.

Some atomic disorder is hardly avoidable because of the small activation energy for site exchange. Disorder has a direct consequence on the intrinsic physical properties. The simplest types of disorder are the B2 and A2 disorder. [BWF$^+$08] In the B2 disorder the Y and Z atoms are mixing and in the A2 disorder all atoms are mixing.

A class closely related to the Heusler compounds is the class of inverse Heusler compounds with a Hg_2CuTi type structure (space group $F\bar{4}3m$) and the half Heusler compounds with the composition XYZ crystallizing in the C1$_b$ structure type (not investigated in this thesis). [BWF$^+$08]

Astonishing are the simple rules predicting common properties of many Heusler alloys. [GFP11] The most famous rule, for example, is the generalized Slater-Pauling rule [Küb84, GMD06] used to estimate the magnetization expressed as the total magnetic moment μ_{tot}:

$$\mu_{\text{tot}} = (N_v - 24)\ \mu_B\ , \tag{1.1}$$

with μ_{tot} given in Bohr magnetons (μ_B) per formula unit. N_v denotes the valence electron number. As an example, Co_2FeAl possesses 29 valence electrons resulting in a magnetic moment of 5 μ_B per formula unit.

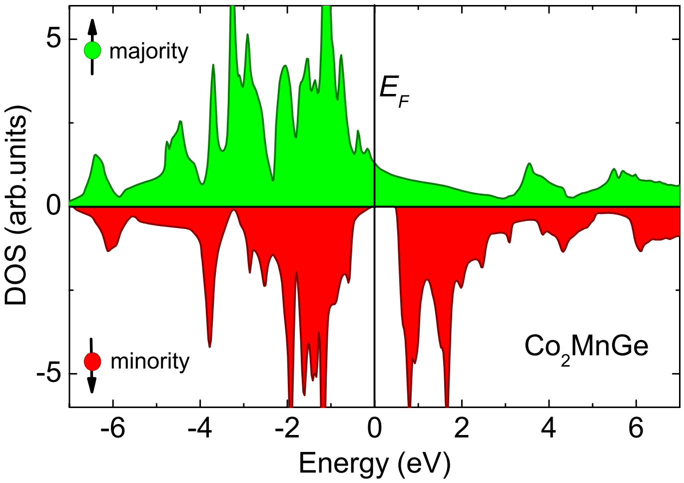

Figure 1.2: *Ab initio* LDA+U calculation by G. H. Fecher. The spin-resolved density of state (DOS) shows the half-metallic ferromagnetic behavior for the Co_2MnGe Heusler compound.

Spintronics

Half-metallic ferromagnetic Heusler materials possess all the requirements for spintronic applications as a result of their exceptional electronic structure. [vJS04, FFB07, Ohn10] The electronic band structure shows properties of a metal for one spin direction and properties of a semiconductor for the complementary spin direction. As an example the density of states (DOS) for Co_2MnGe is shown in Fig 1.2. For many Co-based Heusler alloys as investigated in Chap. 4, 5, and 6 a half-metallic ferromagnetic behavior is predicted with a band gap at the Fermi energy for the minority states promising a large spin polarization usable in transport measurements. [Küb83, GDP02, GMD06, KFF07]

Recent years have seen an impressive increase of the large tunnel magnetoresistance effect (TMR) for devices using Heusler electrodes. [KTHR04, YMI$^+$06, SHO$^+$06, TISI07, IIT$^+$08, WSS$^+$09] Now, they are even used in real application devices for the case of high-quality sputter-deposited epitaxial $Co_2FeAl/MgO/CoFe$ films. [WLK$^+$10]

The TMR ratio of the magnetic tunnel junctions with structure ferromagnet1/insulator/ferromagnet2 can be estimated by the Jullière model [Jul75] using the equation

$$\text{TMR} = \frac{R_{ap} - R_p}{R_p} = \frac{2P_1P_2}{1 - P_1P_2} \cdot 100 \quad (in\ \%) \tag{1.2}$$

with R_p (R_{ap}) being the resistance when the two ferromagnets are magnetized parallel (anitparallel). P_1, and P_2 are the spin polarization values for the two electrodes defined by

$$P = \frac{N_\uparrow - N_\downarrow}{N_\uparrow + N_\downarrow}\ , \tag{1.3}$$

where $N_\uparrow$ ($N_\downarrow$) denotes the majority (minority) density of states at the Fermi energy. From Eq. 1.2 it becomes clear that half-metals with $P = 1$ are ideal materials for TMR devices. When the ferromagnetic layers are magnetically aligned in the same direction, majority spin electrons on one side (ferromagnet1) can tunnel into the same states on the other side (ferromagnet2). In the antiparallel alignment a tunneling is forbidden leading to a large resistance.

Progress in the fabrication of TMR devices provides indirect evidence for half-metallicity in Heusler alloys. However, as was shown in Ref. [WLK+10] the large effective spin polarization can be explained by coherent tunneling and therefore cannot be regarded as a proof for half-metallicity.

For spintronic devices it would also be of great advantage, if the Fermi energy could be shifted with respect to the valence and conduction band edge of the minority electrons in analogy to semiconductor plugins. Such a shift of the Fermi energy E_F position in the minority DOS has been proposed for $Co_2(Fe_xMn_{1-x})Si$ by varying the Fe content x in Ref. [BFKF06] and tested by photoemission spectroscopy without spin resolution [FBO+07, SEW+08].

XAS/XMCD is an alternative method to investigate the element-specific spin-resolved unoccupied partial DOS as it will be shown in Chap. 2. In Chap. 4 the polycrystalline Co-based Co_2TiZ (Z = Si, Ge, Sn, and Sb), $Co_2(Mn_xTi_{1-x})Si$, $Co_2(Mn_xTi_{1-x})Ge$, and $Co_2Mn(Ga_{1-x}Ge_x)$ Heusler alloys will be discussed. The element-specific magnetic moments and the tailoring of the band structure by partly replacing elements on the Y and Z site in the X_2YZ Heusler structure will be demonstrated experimentally in good accordance with *ab initio* calculations. In particular, a defined shift of the position of E_F in the minority DOS will be shown.

In Chap. 5 quaternary Heusler compounds of the type CoFeMnZ (Z = Al, Ga; Si, Ge) with 1:1:1:1 composition are investigated being a new class of materials to extend the variety of Heusler compounds. A prominent example is the quaternary compound CoFeMnSi, with a predicted half-metallic band structure. [DLF+09] The structure is derived from the Heusler structure by occupying the four interpenetrating fcc sublattices of the $L2_1$ structure with a different element. The magnetic moments and the unoccupied partial DOS for Co, Fe, and Mn in CoFeMnZ are experimentally evaluated and compared to *ab initio* calculations. The XAS/XMCD measurements help to identify correct the crystal structure which can not be unambiguously determined by X-ray diffraction. XMCD also provides hints for half-metallicity of this compounds.

In spin transfer torque devices the electron spin current influences the orientation of the magnetization. [RS08] For these applications half-metallic ferrimagnetic properties, as predicted for Mn_2VZ (Z = Al, and Si) in Ref. [GÖSA07] and Co_2TiAl in Ref. [IAKI82] are favorable. Half-metallic ferrimagnets posses large magnetic moments but small magnetization due to the internal spin compensation in combination with a high spin polarization. [TNMS05] In Chap. 6 epitaxial Mn_2VAl and Co_2FeAl thin film samples are discussed. Surface and bulk sensitive XMCD experiments were performed revealing the difference of surface and bulk magnetic and electronic structure properties. Additionally, temperature dependent measurements support a model considering many-body effects [KIC+08] to explain the hitherto puzzling strong temperature dependence of the spin polarization.

Thermoelectrics

Today, Heusler compounds have also received much attention in thermoelectric applications, e.g. power generators or as cooling and heating devices. [GFP11] For metals, heat and charge currents are closely linked to each other by, e.g., the Wiedemann-Franz law. For thermoelectric applications exploiting the Peltier or Seebeck effect, however, a large thermal resistance and a small electrical resistance is needed. Half-Heusler materials are most attractive for thermoelectrics having a large Seebeck coefficient and a large electrical conductivity. [GFP11] Narrow electronic bands known from theoretical calculations lead to a high effective mass resulting in a large thermopower. [UYH+99, GFP11]

The investigated samples and their quality will be introduced in Chap. 3. In some cases of the quaternary Heusler compounds a peculiar phase decomposition will be shown. Especially $Co_2(Mn_{0.5}Dy_{0.5})Sn$ shows a self-organized flower-like pattern. The phase separattion for $Co_2(Mn_xTi_{1-x})Si$, $Co_2(Mn_xTi_{1-x})Sn$, and $Co_2(Mn_{0.5}Dy_{0.5})Sn$ alloys lead to improved thermoelectrical properties. [GKB+10, GBB+10, SSO+12] The additional phonon scattering processes at the phase boundaries result in a reduction of the lattice thermal conductivity and in an increase of the Seebeck coefficient. [GKB+10]

Including the spin, it becomes clear that the long-known thermoelectric phenomena need to be re-considered for half-metallic Heusler materials. Spin-polarized currents by a thermal gradient in (half-metallic) ferromagnets give rise to novel spincaloric effects modifying thermal transport, magneto-resistance properties and possibly even magnetic states. [HKN+10, UTH+08, JYM+10]

Shape memory alloys

Ferromagnetic shape memory alloys (SMA) have attracted a great scientific and technological interest because they can show magnetic field induced strains of 10 % by the rearrangement of twin variants in the martensitic phase. [UHKO97, Ots98, ASU02, Eic11] Many of these alloys are based on the Heusler alloy Ni_2MnGa and are potential smart materials for use in magneto-mechanical devices. SMA devices can be miniaturised and integrated in microelectronics, for example as magnetically driven actuators, sensors, positioning devices and even as valves or pumps in a micro fluidic system. [Whi06, WJZ+07, KKB+08, KKG+08] SMA materials can be driven by heat, applied stress or an applied magnetic field. The latter method has the advantage of a fast control of the external parameter. For magnetically activated motion a large magneto-crystalline anisotropy energy is a necessary condition. [UHK+96, O'H98] This requirement is fulfilled in the martensitic phase of the Ni_2MnGa shape memory alloy. [Ots98]

In the martensitic phase, twin variants occur in which the magnetic easy axis is aligned parallel to the axis of each variant, as shown in Fig. 1.3. An external magnetic field aligned parallel to one of the variants easy axis leads to a growing of this variant at the expense of variants with different orientation resulting in a macroscopic strain. The motion of twin boundaries in the martensitic phase is driven by the magnetic pressure on the twin boundary which is the

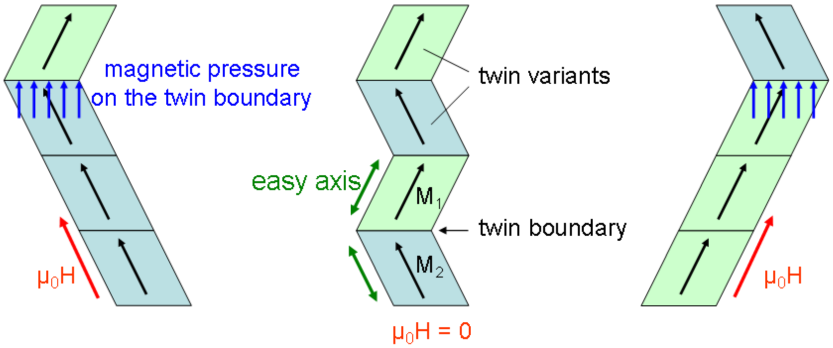

Figure 1.3: Twin boundary motion of the martensitc SMA phase in accordance to Ref. [O'H98]. Without external magnetic field $\mu_0 H$ the magnetization is aligned along the magnetic easy axis of the twin variants (middle). With an applied magnetic field the twin boundary motion is forced by the magnetic pressure at the twin boundary (left and right).

Zeeman energy difference between the twin variants. [O'H98] Without a large magneto-crystalline anisotropy energy the external magnetic field will just align the magnetization of the two twin variants parallel to the magnetic field minimizing the Zeeman energy. If a magnetic anisotropy is present, the anisotropy energy provides the energy to move the twin boundaries and finally the externally available work. In order to activate the device with practically small fields a large magnetization of the material is necessary. In order to provide a large mechanical work, a large anisotropy constant is needed.

In Chap. 7, the origin of the large magnetic crystal anisotropy in Ni_2MnGa is investigated by angular dependent XAS/XMCD measurements. Spectroscopic changes in dependence on the magnetization direction with respect to the crystal axis reveal changes of the occupation of specific Ni 3*d* orbitals that are responsible for the anisotropy. XAS/XMCD measurements show that for Ni_2MnGa the large magnetization stems from the Mn atom and the large magnetic anisotropy from the Ni atom.

The spectroscopic results in combination of theoretical calculations in this thesis build a powerful unit for investigation of intermetallic Heusler materials. The investigated functional Heusler compounds in this thesis allow a tuning and controlled design of their physical properties, which carry an enormous potential for near future applications, e.g., spintronics, thermoelectrics, and smart shape memory alloy devices.

Chapter 2

Experimental Methods

2.1 Magnetic circular dichroism in X-ray absorption

Magnetic circular dichroism (XMCD) in X-ray absorption (XAS) describes the interaction of circularly polarized light with matter. For the first time Erskine and Stern [ES75] theoretically predicted magneto-optical effects in the X-ray region in 1975. More than 10 years later Schütz et al. [SWW$^+$87] demonstrated the circular dichroism in X-ray absorption at the Fe K edge. Today, XAS/XMCD measurements are primarily used to determine element-specific magnetic spin and orbital moments in metallic and intermetallic materials using sum rules (see below). [CIL$^+$95]

Using the full spectroscopic information of the X-ray absorption spectra one can also deduce the partial unoccupied density of states as described in Refs. [KKS$^+$09, KKE$^+$09] and below. One obtains additional information on the binding energy of electronic states and hints on the localization of states. For example, strongly localized states like in oxides lead to strong interaction between the core hole and the conduction band in the final state and to an additional splitting of the spectra, often denoted as multiplet effects.

The XAS/XMCD experiments were performed at the UE56/1 - SGM undulator beamline at the German synchrotron light source BESSY II (see Fig. 2.1). The investigated polycrystalline samples were cleaved *in situ* in UHV ($p = 1 \times 10^{-9}$ Torr) directly before the measurement. The total electron yield (TEY) served as a measure for the X-ray absorption signal. For the thin film samples usually capped by a thin Al layer both TEY intensity and transmission (TM) signal were measured.

- **Total Electron Yield (TEY) measurement:**
  Core electrons are excited by resonant X-ray absorption producing an empty core hole. The empty state can be occupied again by electrons of higher energy states via an Auger electron process. The Auger electrons lead to an increase of excited electrons via an avalanche process by scattering, e.g., a 1000 eV Auger electron produces about $\sim 100 \times 10$ eV electrons. The current of the low energy electrons leaving the sample surface can be measured by a sensitive amperemeter. The measured total electron yield current I_{TEY} is proportional to the X-ray absorption intensity I_{XAS}. The

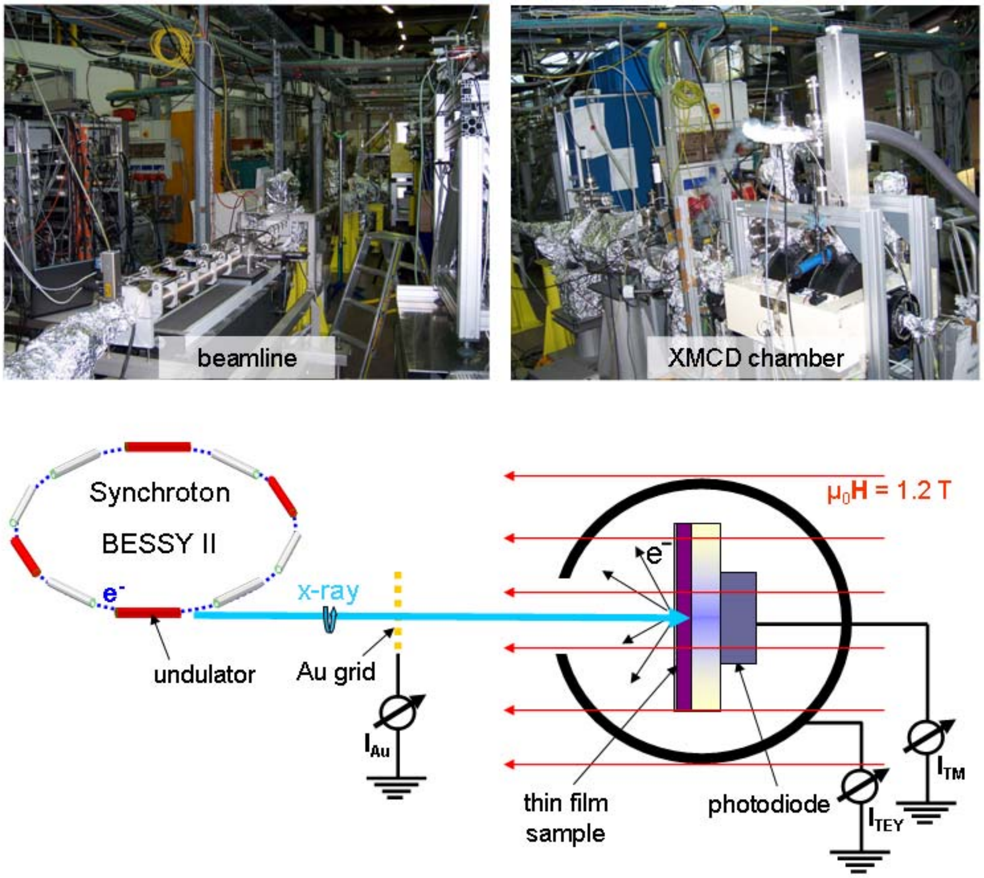

Figure 2.1: UE56/1-SGM undulator beamline at the synchroton light source BESSY II (Helmholtz Zentrum Berlin) and the XMCD chamber. The lower part shows the schematic sketch of the XAS/XMCD experiment.

information depth of the TEY signal is 2.5 nm (surface sensitive!) in the case of Heusler alloys, limited by the mean free path of the secondary low energy electrons (cf. Fig. 2.9 (a)). To collect all electrons the sample is shielded by a metallic tube.

- **Transmission (TM) measurement:**
  In thin films samples only a part of the X-ray intensity is absorbed in the thin film itself and the remaining part is absorbed in the transparent film substrate. The transmitted photons induce light by a luminescence effect in the film substrate which can be detected with a photodiode. The photodiode current is a measure for the transmitted X-ray intensity carrying information integrated across the whole film thickness (bulk sensitive!). Using Lambert-Beer´s law the XAS intensity I_{TM} measured in transmission results in the relation $I_{\mathrm{XAS}} = \kappa \propto -1/t \cdot \ln(I_{\mathrm{TM}}/I_{\mathrm{ref}})$. κ is the absorption coefficient, t the film thickness and I_{ref} the reference spectrum measured by the bare substrate crystal which increases nearly linearly with the photon energy. For the transmission measurements a film thickness less than 100 nm is appropriate. For larger thickness the absorption is too large to get a proper signal. For films thiner than 4 nm the absorption coefficient becomes too small for a good signal-to-noise ratio.

An Au grid monitored the incident photon flux (TEY intensity). An external magnetic field of 1.22 Tesla was applied along the direction of the incident X-ray beam, i.e. approximately perpendicular to the sample surface, and switched after each data point to determine the XMCD signal while the polarization was kept constant. For the angular dependent measurements the sample was rotated, additionally. The energy resolution of the X-ray monochromator was set to 0.4 eV at 800 eV photon energy. An increase in the resolution to 0.1 eV at 800 eV for selected samples revealed only marginal changes in the observed spectra. This confirmed that the spectral shape is dominated by the intrinsic life-time broadening of the X-ray absorption. The XAS/XMCD measurements were performed at room temperature and at low temperature by cooling with liquid nitrogen.

In an external magnetic field $\mu_0 H$ and a defined photon polarization the magnetic quantum axis is aligned along the magnetization of the sample. Therefore, for magnetization direction parallel or antiparallel to the photon polarization vector P with constant polarization (e.g. right circular X-ray polarization) one measures two different absorption spectra I^+ and I^- depending on the X-ray energy, respectively. One can either switch the magnetization and keep P constant or vice versa. Fig. 2.2 (b) shows an example for XAS and XMCD spectra at the Co L_3 ($2p_{3/2} \rightarrow 3d$) and L_2 ($2p_{1/2} \rightarrow 3d$) edge for $\mathrm{Co_2FeAl}$. The averaged XAS spectra I_{XAS} is derived from the measured spectra according to

$$I_{\mathrm{XAS}} = (I^+ + I^-)/2 \ , \tag{2.1}$$

and the XMCD spectra I_{XMCD} results from the difference

$$I_{\mathrm{XMCD}} = I^+ - I^- \ . \tag{2.2}$$

A more detailed description of the experimental setup, the data acquisition and evaluation is given in Ref. [Kla, Kal11].

2.1.1 Dipole approximation

Neglecting any multiplet effects, the simplest model (in the dipole approximation) of the X-ray absorption can be described as a resonant excitation of core level electrons (e.g. $2p_{3/2}$), and $2p_{1/2}$ states) into the unoccupied electron states (e.g. $3d$, and $3s$ states) above the Fermi energy E_F as sketched in Fig. 2.2 (a). [Stö99, dG05, dGK08]

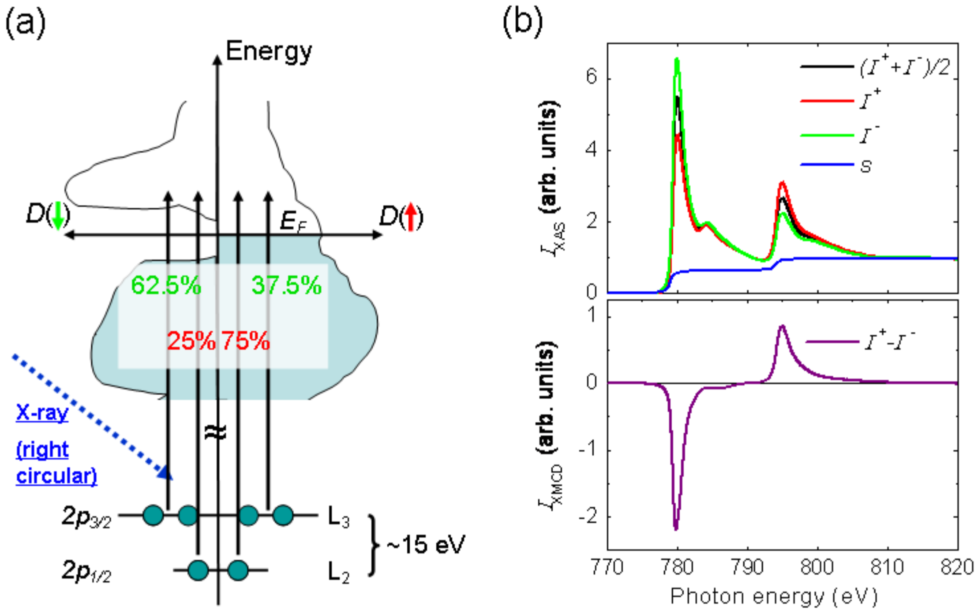

Figure 2.2: (a) Sketch of the one electron X-ray absorption model in the dipole approximation for right circularly polarized photon light. Transition probabilities are given as a percentage resulting in a spin polarization $P_{L_3} = 0.25$ at the L_3 edge and $P_{L_2} = -0.5$ at the L_2 edge (b) Typical measured XAS data and the corresponding XMCD spectra at the Co $L_{3,2}$ edge.

The X-ray absorption of circularly polarized light may then be mapped on a two-step process considering the dipole matrix elements. In the first step, the photo-electron is excited from a spin-orbit split $2p_{3/2}$ or $2p_{1/2}$ level ($L_{3,2}$ edge) and has taken up the angular momentum of the photon in part to its spin due to spin-orbit coupling. [Stö99] Therefore, the excited photo-electrons might be considered spin-polarized depending on the polarization direction of the incident light. Since the L_3 and L_2 edge have opposite spin-orbit coupling the spin polarization is opposite at both edges.

In a second step the unoccupied valence band states serve as a detector for the spin and orbital polarization. As the orbital magnetic moments in Heusler alloys are typically less then 10 % of the spin moment, the orbital polarization of the photoelectrons can be neglected for the following discussion. For $2p$ to $3d$ transitions, the spin polarization P is 25 % at the L_3 edge and -50 % at the L_2 edge. Transitions from $2p$ to $4s$ states are largely suppressed due to the small transition matrix element.

The transition probability W_{fi} is given by Fermi´s golden rule in the dipole approximation by the equation

$$W_{fi} \propto \sum_q \underbrace{| < f|\hat{e}_q \cdot \vec{r}|i > |^2}_{=\mathrm{M}^2} \delta[(E_f - E_i) - \hbar\omega] \ . \tag{2.3}$$

M is the transition matrix element with $\hat{e}_q \cdot \vec{r}$ denoting the dipole transition operator, i the initial, and f the final state wave function. The delta function $\delta[(E_f - E_i) - \hbar\omega]$ allows a resonant transition if the final state energy E_f equals the energy of the initial state E_i plus the photon energy $\hbar\omega$. In the one electron excitation picture one can calculate the transition matrix elements M by the well known Clebsch-Gordan coefficients. This leads to the polarization dependent photon absorption intensity

$$I_{\mathrm{XAS}} \propto \mathrm{M}^2 \cdot D^{\uparrow\downarrow}(1 - f_F) \ . \tag{2.4}$$

Therefore, the shape of the XAS spectra carries information of the unoccupied density of states $D^{\uparrow\downarrow}$ above E_F indicated by the factor with the Fermi function $(1 - f_F)$. Effects from anisotropic charge and spin densities may be neglected for the discussion of polycrystalline samples. Since the radial matrix elements show in general only a small energy dependence, the absorption spectra may be interpreted as a direct measure of the spin-resolved PDOS $D^{\uparrow(\downarrow)}$ above the Fermi energy. $D^{\uparrow}$ is the density of states of the majority states and $D^{\downarrow}$ the density of states of the minority states. This simple interpretation of course requires that the angular matrix elements can be averaged at every energy value, i.e. $3d$ states of different magnetic quantum number equally contribute to the spectral density independent on energy. As has been shown for $\mathrm{Co_2(Fe_xMn_{1-x})Si}$ and $\mathrm{Co_2Fe(Al_{0.3}Si_{0.7})}$ this assumption holds to some extent in the case of the Co L edge spectra. [KKS$^+$09]

2.1.2 Sum rules

Element-specific magnetic moments can be calculated by the sum rules developed by Thole *et al.* [TCSvdL92] and Carra *et al.* [CTAW93]. The first sum rule calculates the effective magnetic spin moment

$$\mu_{\mathrm{eff,spin}} = \mu_{\mathrm{spin}} + \mu_{\mathrm{dip}} = \frac{1}{\gamma C}(-A + 2B)\ \mu_B \quad \text{(per atom)}, \tag{2.5}$$

with μ_{dip} being the result of the intra-atomic dipole operator [Stö95] and μ_{spin} the spin moment being the expectation value of the spin operator [Stö95]. For cubic systems, one may assume $\mu_{\mathrm{dip}} \approx 0$.

The second sum rule describes the magnetic orbital moment

$$\mu_{\mathrm{orb}} = \frac{2}{3\gamma C}(-A - B)\ \mu_B \quad \text{(per atom)}. \tag{2.6}$$

The integrals

$$A = \int_{\mathrm{L}_3} I_{\mathrm{XMCD}} dE \ , \qquad (2.7)$$

$$B = \int_{\mathrm{L}_2} I_{XMCD} dE \qquad (2.8)$$

are integrals over the XMCD spectra at the L_3 and L_2 absorption edge, respectively. C is an integral over the total XAS spectra after subtraction of the step function s as described by the charge sum rule

$$C = \frac{1}{N_h} \int_{\mathrm{L}_3+\mathrm{L}_2} [I_{\mathrm{XAS}} - s] dE \ . \qquad (2.9)$$

s can be approximated by a two step function (see Fig. 2.2 (b)) to account for the absorption into delocalized itinerant s states, and N_h is the number of unoccupied $3d$ states. [EFV$^+$03] The factor $\gamma = P\cos(\Theta)$ (≈ 1 for the XMCD experiment in this thesis) accounts for the X-ray polarization P ($P \approx 1$ for the used undulator beamline), and the angle Θ between the X-ray polarization vector and the sample magnetization ($\cos(\Theta) \approx 1$ for the used geometry).

It is difficult to determine the d hole number N_h for an unknown compound from the XAS spectra and therefore N_h is usually taken from the theory. [EFV$^+$03]

For the sum rules (Eq. 2.5 and 2.6), transitions between free atomic states and a full splitting of the $2p_{3/2}$ and $2p_{1/2}$ are assumed. [Kuc02, TCSvdL92, CTAW93] A correction factor (jj-mixing, see Ref. [Goe05]) is necessary for light 3d elements (V, Ti, Mn, etc.) to consider the $2p_j$ states mixing.

2.1.3 Spin-resolved unoccupied density of states

Within the constraints of Chap. 2.1.1, the spin-resolved unoccupied PDOS $D^{\uparrow(\downarrow)}(1-f_F)$ results from the XAS spectra I^+ and I^- according to

$$D^{\uparrow(\downarrow)}(1-f_F) \propto I_{\mathrm{XAS}} - s + (-)\frac{1}{P_j}\frac{I_{\mathrm{XMCD}}}{2}, \qquad (2.10)$$

where f_F denotes the Fermi function, I_{XAS} the isotropic XAS spectra (Eq. 2.1), I_{XMCD} the XMCD spectra (Eq. 2.2), s the step function and P_j the spin polarization of the excited photo-electrons, i.e. $P_{\mathrm{L}_3} = 0.25$ and $P_{\mathrm{L}_2} = -0.5$. However, the Co states in Heusler alloys take an intermediate position between localized and delocalized states. Therefore, one has to consider core hole interaction at least to the lowest order. That means that the core hole in the final-state attracts the excited electron, thus, lowering the energy needed for excitation when compared to the corresponding ground-state values. In principal, this energy rescaling occurs for all X-ray absorption spectra. It is usually neglected, as it shifts the energy of the absorption energy by a constant value for all states.

For Heusler alloys, the electronic states close to the Fermi energy are dominated by two different types of electronic states that can be classified as localized $3d - e_g$ and itinerant $3d - t_{2g}$ states. In the case of $\mathrm{Co_2FeSi}$ the itinerant band

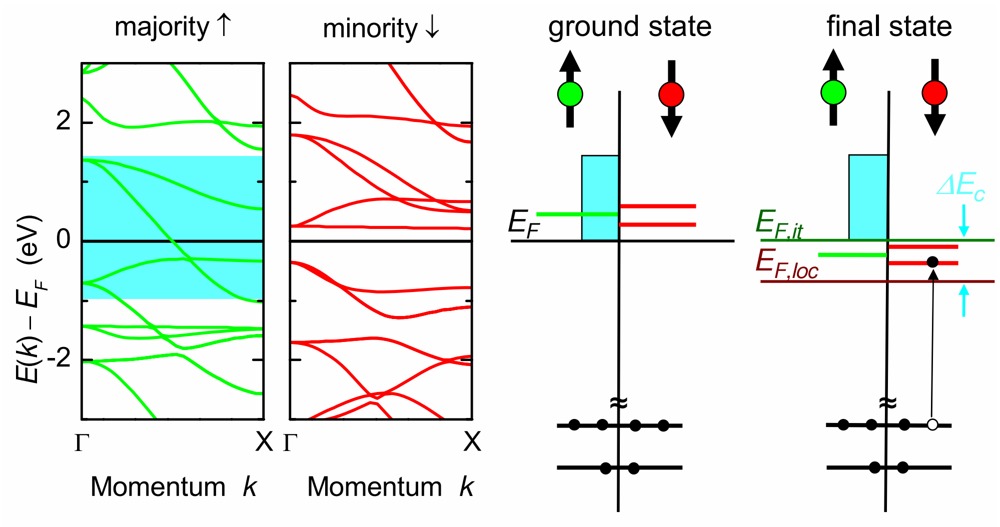

Figure 2.3: (Left) Spin-resolved band structure for Co_2TiGe calculated by G. H. Fecher (AK Felser). (Right) Schematic description of the absorption process emphasizing the different reference energies for the localized and the delocalized $3d$ final-state configurations separated by ΔE_c.

dominates the unoccupied majority states near E_F [FFB07], while the minority states close to E_F are dominated by localized states. This is the case for most of the Co-based Heusler alloys. The core hole in the final-state attracts the electron in the localized $3d$ states to a larger extent, thus lowering the photon energy needed for the transition.

For an itinerant state the energy decrease is smaller since the electrons from neighboring atoms screen the core hole to some extent. [WCvA$^+$90, Bia82] For a free electron state this final-state effect would completely vanish and the excitations energy equals the value following from the one-electron model. The different core hole screening thus produces an energy shift ΔE_c between itinerant and localized states (see also Fig. 2.3). [WCvA$^+$90, Bia82] A similar effect has been observed in the V K edge absorption spectra for VO_x (Ref. [Bia82]).

The exact value of ΔE_c is very critical for the determination of half-metallic properties from the XMCD data. ΔE_c is related to the bandwidth or, in other words, to the degree of localization of the contributing states. To first order it does not depend on the magnetic moment as given by the difference of unoccupied majority and minority states. For many Co-based Heusler compounds, calculations reveal a rather similar band structure close to E_F independent of the occupancy of the Y and Z sites except for a relative shift of each contributing band. Thus one expects to first order a constant value of ΔE_c. In the case of Co_2TiSi ($N_v - 24 = 2$), the majority electron states are composed of both itinerant and localized states at E_F. In this case one expects a splitting of the onset of unoccupied majority states at E_F. The splitting allows for a direct experimental determination of $\Delta E_c = 0.5$ eV as shown below. In the case of Co_2FeSi ($N_v - 24 = 6$), a close comparison with *ab initio* calculation using a LDA+DMFT ansatz [CFF$^+$09] led to the same value. Moreover, the same

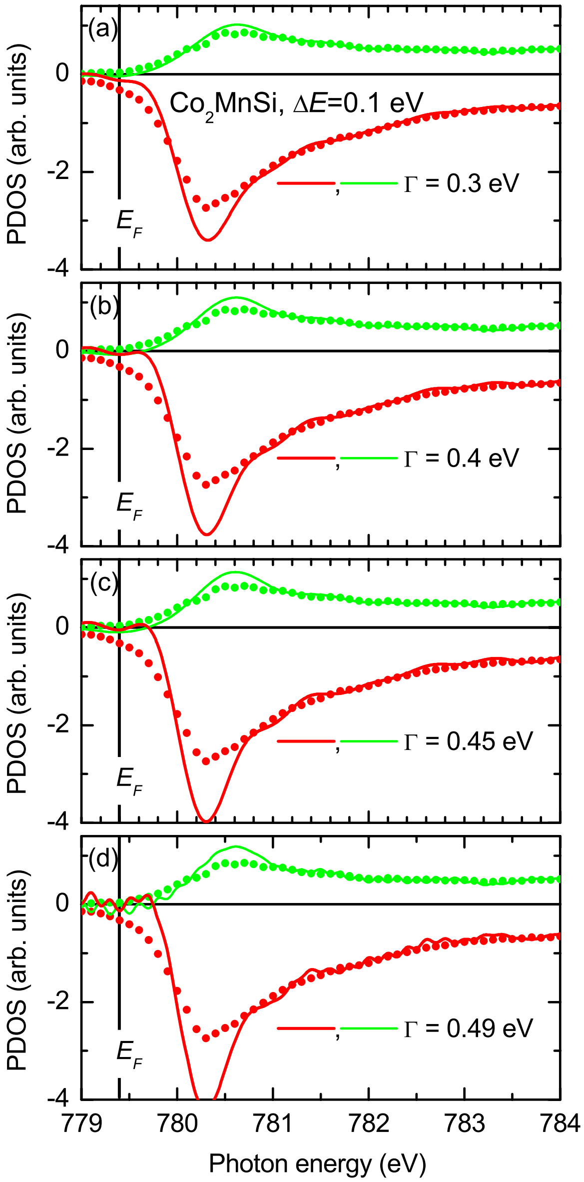

Figure 2.4: Spin-resolved PDOS calculated from the XAS/XMCD data measured at the Co L_3 edge of a Co_2MnSi film with similar spectra as the bulk data. Majority PDOS (green circles) and minority PDOS (red bullets) are shown on a positive scale and negative scale, respectively. Data after deconvolution with a Lorentzian function (full lines) of width Γ as indicated in the Figure.

calculation predicted a shift of E_F with respect to the conduction band edge of minority electrons for the series $Co_2(Fe_xMn_{1-x})Si$ ($N_v - 24 = 5 - 6$), which could be confirmed using a constant value of $\Delta E_c = 0.5$ eV. [KKS$^+$09] In the following, this constant value is assumed for the determination of the position of E_F. Recently, a direct comparison of XAS/XMCD spectra with calculations confirmed the existence of this electron correlation effect for Co_2TiSn in Ref. [MSW$^+$11]. Even the effective value of ΔE_c shows a surprising coincidence.

An analysis of Fe, Mn, Cr, and Ti spectra with respect to an evaluation of the PDOS is increasingly difficult because of the increasing localization and increasing contribution of multiplet effects as discussed in Ref. [dGFTS90]. For example, the Mn $L_{3,2}$ spectra in Co_2MnSi are convincingly explained by multiplet calculations based on atomic states (see Ref. [TKvdL$^+$08]). A combination of band structure calculations and multiplet calculations will possibly enable a recovering of the Fe, Mn, Cr, or Ti PDOS from experimental data but they are not available at present. However, an encouraging *ab initio* configuration-interaction method has recently been presented for the case of molecular orbitals. [IdGST09]

In order to account for the life-time broadening of the XAS/XMCD spectra, XAS data for Co_2MnSi with high energy resolution ($\Delta E = 0.1$ eV) was deconvoluted with a Lorentzian function as shown in Fig. 2.4. The Co PDOS was determined according to Eq. 2.10 and deconvoluted with a Lorentzian function of various widths Γ. The results compared in Fig. 2.4 reveal an increasing steepness of the initial onset of the minority DOS with increasing value of Γ. However, values larger than $\Gamma = 0.4$ eV lead to an increasing contribution of oscillations, in particular, for $E < E_F$ indicating an overestimation of the lifetime broadening.

The observation of a zero line for $E < E_F$ for $\Gamma = 0.4$ eV is a consequence of a near coincidence of the Lorentzian function and the experimental data. Note that for $\Gamma = 0.4$ eV, the Co minority PDOS is close to zero in a finite energy interval around E_F. Thus, the experimental data support the theoretical prediction of Co_2MnSi being a half-metal even if ΔE_C slightly differs from the assumed value. Attempts of using a deconvolution function of a convoluted Lorentzian and Gaussian function in order to consider the finite-energy resolution led to an increased contribution of oscillations and were therefore abandoned.

In this thesis, a Lorentzian function Γ with a constant value of $\Gamma = 0.4$ eV in Chap. 4, and 6, and $\Gamma = 0.35$ eV in Chap. 5 are applied for deconvolution of the experimental data. The same result can be calculated from the L_2 edge as discussed in Ref. [KKS$^+$09]. But $D^{\uparrow(\downarrow)}$ derived from the L_2 edge shows an even larger broadening because of the Coster-Kronig decay. [dGFTS90].

According to Eq. 2.10, the spin-resolved unoccupied PDOS function $D^{\uparrow(\downarrow)}$ for Co_2TiSi has been calculated from data at the Co L_3 edge in Fig. 2.5. For consideration of the thermal magnetization decrease at 300 K the XMCD signal was multiplied by a factor $M(0)/M(T) = 1.66$. The majority PDOS shows a characteristic double step increase at E_F, which can be directly related to the onset of the localized majority states at E_F and the onset of the itinerant majority state shifted by $\Delta E_C = 0.5$ eV to higher energy (as discussed before). The experimental data fit well to the PDOS calculated in Refs. [LLBS05]

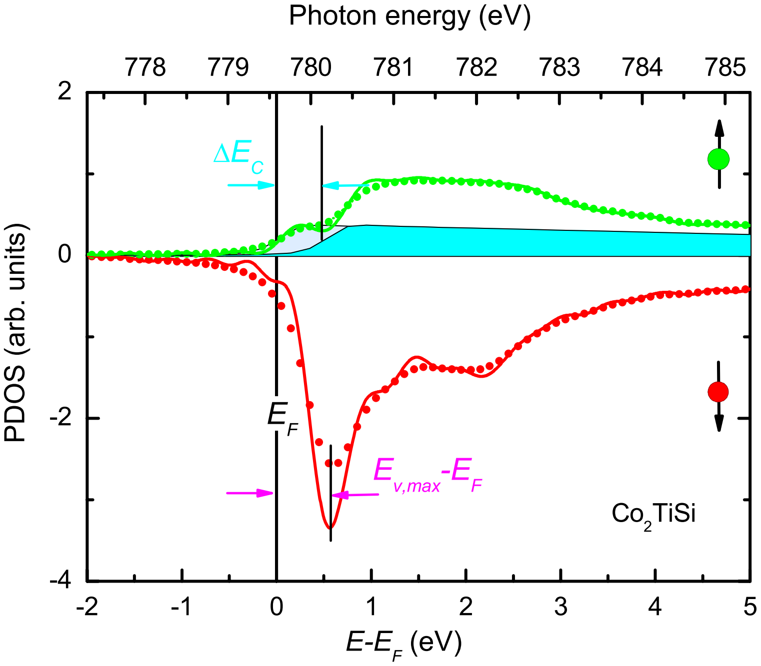

Figure 2.5: Spin-resolved PDOS calculated from the XAS/XMCD data measured at the Co L_3 edge. Majority PDOS (green circles) and minority PDOS (red circles) are shown on a positive and negative scale, respectively. Full lines with shadings indicate the function used for approximation of the itinerant band as measured (blue) and shifted by ΔE_C (gray). $E_{v,max} - E_F$ is defined as the energy difference between the minority PDOS maximum $E_{v,max}$ and the Fermi energy E_F.

and [KFF07] (see also Fig. 4.8 (a)). The minority PDOS shows a sharp onset above E_F with an inclination point at $E_F + 0.3\ eV$, as expected for a half-metal. The broadening of the spectra caused by the finite lifetime of the excited state and by the limited energy resolution, however, hinders a direct determination of the spin polarization at E_F from this data. For the discussions in the following chapters it is useful to introduce the separation of the prominent maximum in the unoccupied minority PDOS $E_{v,max}$ and the Fermi energy E_F as $E_{v,max} - E_F$.

2.1.4 Electron correlation

In the exact description of X-ray absorption, the atom is excited from an initial-state configuration to a final-state configuration, e.g., $2p^63d^7$ to $2p^53d^8$. When the final state consist of more than one unoccupied state, correlation effects between the final states lead to multiplet effects. [dGFTS90, dG05]

Previous results on X-ray absorption spectroscopy have shown that the existence of local moments gives rise to pronounced multiplet structures resulting from the interaction of the core hole with the excited electron, thus, representing a final-state effect. [GDG+02, EFJ+05, TKvdL+08, KKE+09] The consideration of final-state effects exceeds state-of-the-art band-structure calculation schemes. Nevertheless, multiplet features might be accurately described by an atomic model in the case of localized electronic states as they are discussed for Heusler alloys. The following discussion is focused on Co states with $3d$ character as these states are closest to the Fermi energy. A multiplet calculation is shown in Fig. 2.7 based on the program described in Refs. [dGFTS90, Cow81, mis]. The charge-transfer multiplet calculation considers electric dipole allowed transitions between a mixed Co $2p^63d^7$ and $2p^63d^8$ ground state and the corresponding final states $2p^53d^8$ and $2p^53d^9$. The crystal field was set to zero. The calculated results were convoluted by a Lorentzian of $\Gamma = 0.1(0.3)$ eV for the L_3 (L_2) edge to account for intrinsic lifetime broadening and a Gaussian of $\sigma = 0.2$ eV for the instrumental broadening according to previously published calculations. [dGFTS90] Note that the realistic lifetime broadening correeponds to $\Gamma = 0.4$ eV (0.8 eV) at the L_3 (L_2) edge.

The charge-transfer energy parameter was varied from +9 eV to −5 eV corresponding to an almost linear variation in the ground state from $2p^63d^7$ to $2p^63d^8$. The multiplet features show up as multiple peaks that are more pronounced at the L_3 edge. For $\Delta E = -1$ eV, one obtains a mixed ground state of equal weight of the $2p^63d^7$ and $2p^63d^8$ state, according to the number of unoccupied $3d$ holes of N_h(Co)= 2.5 assumed for the sum-rule analysis. Note, that no resemblance with experimental Co XAS/XMCD spectra appears for any charge-transfer values. The extra peak at 1 eV above the L_3 XMCD maximum appearing for $\Delta E > -2$ eV and also visible in experiment is accompanied by a similar peak in the L_3 XAS spectra, which is not observed experimentally. A reduction in the Slater integrals to 80 % of the Hartree-Fock calculated values has been shown to be close to the optimized value to simulate the multiplet spectra of atoms. [dGFTS90] For itinerant electron states of atoms in a metallic surrounding, one might expect an even larger reduction. Fig. 2.7 shows the change in the spectra from the atomic multiplet features to the single peak at each L edge with decreasing core hole interaction. Thus, one may keep the one-electron model in cases where itinerant states sufficiently suppress this multiplet splitting of transition energies as, e.g., in intermetallic alloys and compounds.

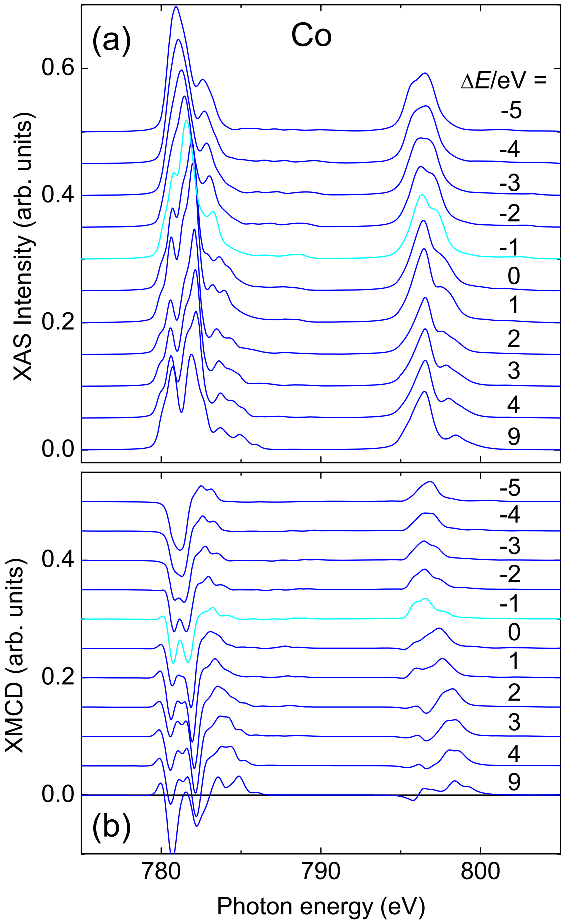

Figure 2.6: (a) Series of XAS charge transfer multiplet calculations for the Co $2p^6 3d^7$ plus $2p^6 3d^8$ ground state for steps of 1 eV for the charge transfer energy. The top spectrum corresponds to $N_h = 2.19$ and the top bottom spectrum to $N_h = 2.94$. The spectrum corresponding to the value of $N_h = 2.5$ as calculated by band structure calculations is highlighted. (b) XMCD spectra calculated for the same parameters.

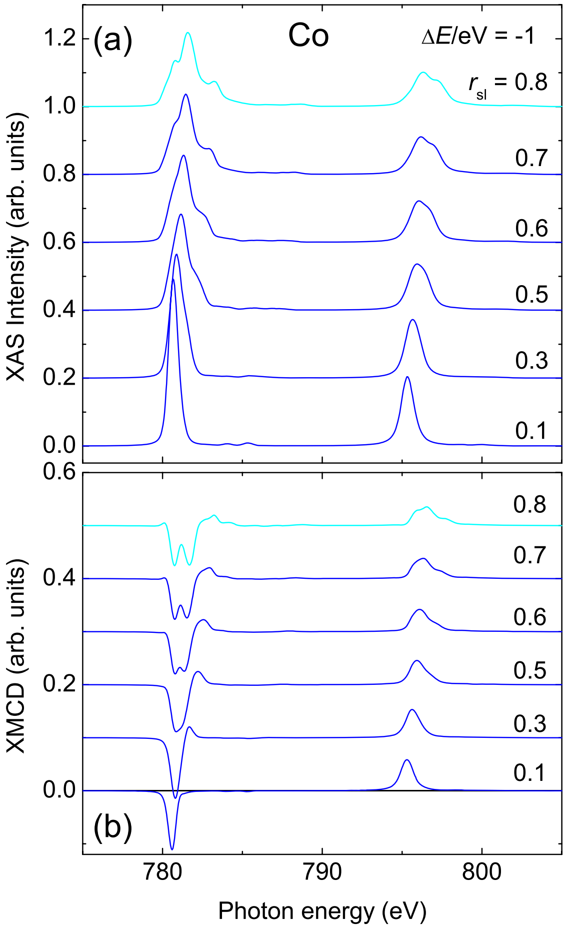

Figure 2.7: (a) Series of XAS charge-transfer multiplet calculations with varying reduction factor r_{sl} of the Slater integrals for the Co $2p^6 3d^7$ plus $2p^6 3d^8$ ground state at a charge-transfer energy of -1 eV ($N_h = 2.5$). (b) Corresponding XMCD spectra.

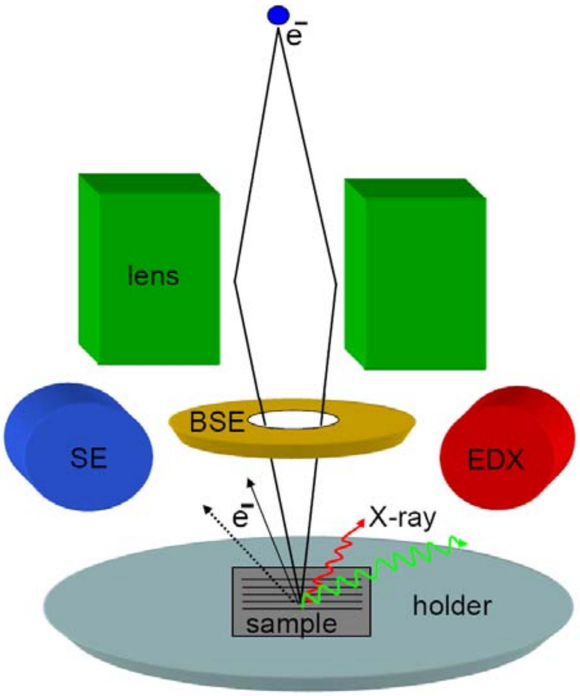

Figure 2.8: (a) Schematic sketch of the SEM/EDX detection system.

2.2 Energy dispersive X-ray analysis

Energy dispersive X-ray analysis (EDX) is a common method to analyze the stoichiometry of bulk samples. A high-energy electron beam can be used to excite electron states, e.g., as provided by a scanning electron microscope (SEM). An EDX detector in combination of a SEM allows not only quantitative element analysis of the compound composition, but also a spectroscopic element mapping of the sample surface.

A SEM/EDX detection system is shown schematically in Fig. 2.8. Electrons are accelerated through a lens system for line-by-line scanning of the sample surface. The electrons are partially scattered back or absorbed producing secondary electrons and X-ray fluorescence. Therefore, the detection can be performed by a secondary electron detector (SE), a backscattering detector (BSE), and an EDX detector (EDX) providing information about the surface topology and composition.

The SEM Jeol JSM-6400 equipped with an EDX detection system WINEDS was used to check the homogeneity and stoichiometry of the samples. The EDX and the SE detection modus was used simultaneously. An acceleration voltage of 20 KV and an inspection angle of 35° was set up. The quantitative data was corrected by the ZAF method which relies on atomic number (Z), absorption (A) and fluorescence (F) effects. The pressure in the chamber was about 10^{-6} mbar.

X-ray fluorescence is produced by electrons of high kinetic energy, which are scattered and slowed down in the bulk as shown in Fig. 2.9 (a). By the scattering process core holes are produced. This excited atom state is similar to

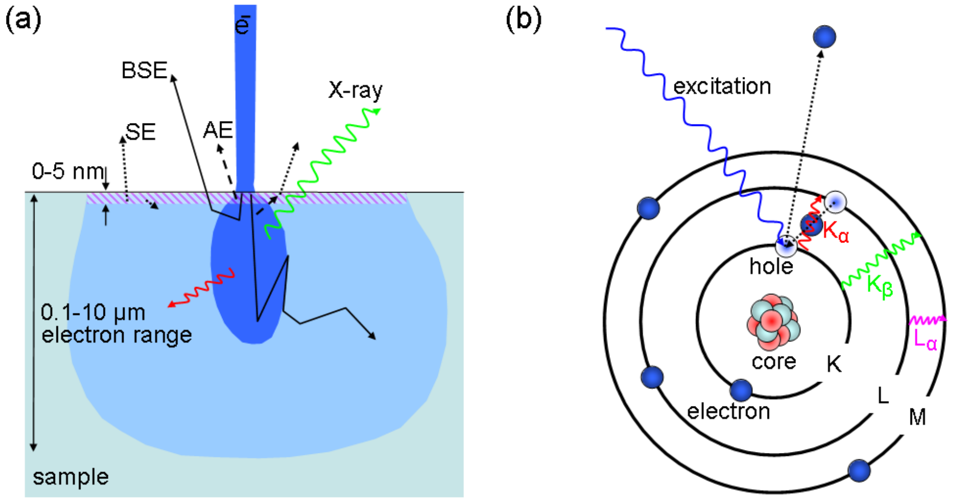

Figure 2.9: (a) Process and information depth of secondary (SE), backscattered (BSE), Auger electrons (AE) and X-ray fluorescence (X-ray) in the diffusion cloud for normal electron beam incidence. (b) X-ray fluorescence process produced by an excitation current (electron beam).

the final state in X-ray absorption as discussed before. Subsequently, the core hole is filled by electrons from the outer shell. In addition to the Auger process producing again a high energy electron, the de-excitation alternatively leads to an emission of a high energy photon. The photon energy is characteristic for each element. The photon emission process becomes more efficient for heavy elements in comparison to the non-radiative Auger process.

For instance, an electron from the L shell fills the vacant state of the K shell emitting a photon with a characteristic energy K_α as sketched in Fig. 2.9 (b). From the element characteristic energies (K_α, K_β, L_α, etc.) and from the resulting EDX spectra it is possible to determine the element and its concentration in the sample.

The photon energy of the X-ray fluorescence is usually detected by a Si(Li) detector. The photon produces a number of electron-hole pairs in the detector, which is proportional to its energy. The energy resolution of this energy dispersive detector is several eV. Therefore, it is not possible to resolve spectroscopic details as in the case of XAS. The information depth is rather large due to the large mean free path of the incident high kinetic energy electrons (several tens nanometer) and the even larger mean free path of the X-ray photons. The lateral resolution is limited to ~ 100 nm because of the scattering distribution of incident electrons.

Because of the large path of the incident electron beam (0.1-10 μm depending on electron energy and target density, see Fig. 2.9 (a)), thick bulk samples are suitable. In thin films the incident electron beam will be partly absorbed in the film sample and the remaining beam in the film substrate. In this case a standard quantitative determination is not possible and special prepared calibration standards to quantify the right composition of the constituents are necessary. Details about EDX and SEM can be found in Refs. [Rei85] and [Sch94].

Chapter 3

Sample preparation and structural properties

3.1 General remarks

This chapter summarizes details of the sample preparation and structural investigations by X-ray diffraction that have been performed by partner groups. Characterization by scanning electron microscopy (SEM) combined with energy-dispersive X-ray spectroscopy (EDX) were measured as part of this thesis.

The crystal structure and even crystal orientation in the XAS/XMCD experiment has direct consequences on the physical properties and the measured experimental results. Samples with a well defined local order is a precondition for comparison of experimental results with theory. Furthermore, through an appropriate variation of the stoichiometry and the local atomic ordering one has a direct control of the electronic band structure and its resulting properties. For example, a small change of the Ni_2MnGa 2:1:1 stoichiometry leads to a strong variation of the phase transition temperature, where the transition from the austenitic to the martensitic phase takes place. [Eic11] Even with optimized preparation methods, it is always not possible to avoid local disorder, decomposition or phase separation. A high degree of local disorder is usually not welcome for spintronic applications, because it can destroy the half-metallicity of the electronic structure. [MNS04, PCF04, GH07] Decomposition or phase separation is not always undesirable. Phase separated Heusler alloys, which have been also found in this work, are of highest interest for thermoelectric, spincaloric and even for spintronic applications. [RKTH07, GKB$^+$10, GBB$^+$10] Compared to a single-phase sample, phonon scattering processes at phase boundaries lead to a reduction of the lattice thermal conductivity.

The investigated polycrystalline bulk samples were prepared by the group of C. Felser. The thin films investigated in this thesis were produced by the groups M. Jourdan, G. Jakob, and K. Inomata, who have a high experience in controlled thin film deposition. The characterization of the samples by X-ray diffraction (XRD) and magnetometry [via Superconducting Quantum Interference Device (SQUID) or Vibrating Sample Magnetometer (VSM)] was done in these groups, too. To check the homogeneity and stoichiometry of the bulk samples a SEM

	Co	Ti	Z
Z = Si	49	23	28
Z = Ge	50	23	27
Z = Sn	53	25	22
Z = Sb	49	26	25

Table 3.1: Relative concentrations given as atomic percentages of the samples for Co_2TiZ determined by an EDX analysis. The error is approximately 2-atomic %.

equipped with an energy dispersive EDX was used as described in Chap. 2.2. In the following, a short description of the sample preparation and characterization is given for the particular samples examined within this thesis.

3.2 Polycrystalline bulk samples

Polycrystalline bulk samples were prepared by arc melting of stoichiometric quantities of the constituents in an argon atmosphere (10^{-4} mbar). Avoiding of oxygen contamination was established by evaporation Ti inside the vacuum chamber before melting the compound as well as additional purification of the process gas. To get a homogeneous material the melting procedure was repeated three times. After melting, the polycrystalline ingots were annealed in an evacuated quartz tube for about 2 weeks. For powder investigations, a part of the sample was crushed by hand using a mortar. The crystal structures of the samples were determined by X-ray diffraction (XRD) using Mo K_α radiation (Bruker D8 Advance). The magnetic properties were investigated by a superconducting quantum interference device (SQUID, Quantum Design MPMS-XL-5) using nearly punctual sample pieces of approximately 20 to 30 mg. Rods with dimensions $1 \times 1 \times 10$ mm^3 were cut from the ingots for spectroscopic investigations of the bulk samples. For the measurements with the SEM/EDX detector system, one should note, that the accuracy of the determination of the relative atomic concentration is on the order of ±2-atomic %.

3.2.1 Co_2TiZ (Z = Si, Ge; Sn, Sb)

X-ray diffraction revealed a diffraction pattern that is compatible with a high degree of $L2_1$ order. The preparation and the structural investigations were performed by J. Barth (AK Felser) and more details can be found in Refs. [GCW^+09, BFB^+10, BFB^+11]. The EDX analysis of the fractured surfaces revealed a homogeneous composition for all samples with small deviations from the stoichiometric composition. The relative atomic compositions for the elements Co, Ti, and Z are listed in Tab. 3.1.

3.2.2 $Co_2(Mn_xTi_{1-x})Z$ (Z = Si, Ge)

The XRD analysis for $Co_2(Mn_xTi_{1-x})Si$ revealed a single $L2_1$ Heusler phase with a linearly varying lattice constant for $x = 0$ to 5.74 Å for $x = 1$ to 5.65 Å.

$Co_2(Mn_xTi_{1-x})Ge$ shows the Heusler L2_1 structure with a small B2 type disorder contribution. The XRD analysis and the sample preparation was done by C. G. F. Blum (AK Felser). The EDX analysis for the $Co_2(Mn_xTi_{1-x})Si$ series resulted in some deviations from the intended composition as listed in Tab. 3.2. In addition, the samples showed traces of a decomposition into a Ti-rich and a Ti-poor Heusler compound with the Co and Si concentration being constant across the fractured surface (see also Chap. 3.3). From the EDX analysis of the $Co_2(Mn_xTi_{1-x})Ge$ sample surfaces the relative atomic compositions according to Tab. 3.3 are obtained. Within error limits the average composition reproduces the desired composition for the $Co_2(Mn_xTi_{1-x})Ge$ series. In contrast to $Co_2(Mn_xTi_{1-x})Si$ these samples have a homogeneous composition.

	Co	Mn	Ti	Si
$x = 0.0$	49.0	0.0	23.0	28.0
$x = 0.4$	51.6	10.0	14.3	24.1
$x = 0.6$	48.9	14.9	8.7	27.5
$x = 0.8$	43.9	18.5	9.5	28.1
$x = 1.0$	47.9	25.3	0.0	26.8

Table 3.2: Relative concentrations given as atomic percentages of the samples for $Co_2(Mn_xTi_{1-x})Si$ determined by an EDX analysis. The error is approximately 2-atomic %.

	Co	Mn	Ti	Ge
$x = 0.0$	49.5	0.0	23.2	27.3
$x = 0.2$	49.8	4.8	20.7	25.1
$x = 0.4$	49.2	10.2	14.9	25.7
$x = 0.5$	49.9	12.5	12.4	25.2
$x = 0.6$	49.4	15.0	10.1	25.5
$x = 1.0$	49.2	25.3	0.0	25.5

Table 3.3: Relative concentrations given as atomic percentages of the samples for $Co_2(Mn_xTi_{1-x})Ge$ determined by an EDX analysis. The error is approximately 2-atomic %.

	Co	Mn	Ga	Ge
$x = 0.0$	47.7	24.7	27.6	0.0
$x = 0.2$	48.6	24.3	21.8	5.3
$x = 0.4$	48.5	23.9	16.9	10.7
$x = 0.6$	48.0	24.8	10.9	16.3
$x = 0.8$	45.7	26.1	5.7	22.5
$x = 1.0$	47.9	25.3	0.0	26.8

Table 3.4: Relative concentrations given as atomic percentages of the samples for $Co_2Mn(Ga_{1-x}Ge_x)$ determined by an EDX analysis. The error is approximately 2-atomic %.

	Co	Fe	Mn	Z
Z = Al	24.4	25.3	25.0	25.3
Z = Ga	24.3	26.4	24.6	24.7
Z = Si	24.5	25.6	24.7	25.2
Z = Ge	24.4	24.6	24.7	26.3

Table 3.5: Relative concentrations given as atomic percentages of the samples for CoFeMnZ (Z = Al, Ga; Si, Ge) determined by an EDX analysis. The error is approximately 2-atomic %.

3.2.3 $\mathbf{Co_2Mn(Ga_{1-x}Ge_x)}$

X-ray diffraction revealed a $L2_1$ compatible pattern for this series of samples. The almost equal scattering cross section of the constituting elements hinders an unambiguous structural determination from XRD. The sample preparation and XRD measurements were done by C. G. F. Blum (AK Felser). NMR measurements at the Mn resonance revealed a $L2_1$ structure with a small degree of disorder. [JHKF] The EDX analysis of this series revealed a homogeneous composition for all samples except for the sample with $x = 0.2$, where a small variation in the Ge/Ga ratio across the sample was observed. The relative atomic compositions are given in Tab. 3.4.

3.2.4 CoFeMnZ (Z = Al, Ga; Si, Ge)

The sample preparation and the crystal structure determination by XRD of CoFeMnZ (Z = Al, Ga; Si, Ge) is done by V. Alijani (AK Felser). More details about the structural properties can be found in Ref. [AOF$^+$11]. CoFeMnSi shows a clear (110) and (200) reflection indicating a dominating type I structure which is proposed in Ref. [DLF$^+$09] (see also Fig.5.1). For CoFeMnAl only the (200) reflection is observed, which is compatible with the dominating type I structure combined with a B2-type disorder. It is known that Al-containing Heusler compounds are very susceptible to disorder effects. [BWF$^+$08] The (200) fcc-superstructure reflections are absent or very small for CoFeMnGa and CoFeMnGe due to nearly equal scattering amplitudes of the constituting elements, which prevents a detailed structure analysis. Eventually, a distinction between the three proposed crystal structures is impossible because of the equal scattering crossections of the $3d$ constituents.

3.3 Phase separated alloys

In rare cases Heusler alloys show a phase separation into phases with different compositions. The alloys discussed here open a new possibility to improve their thermoelectric and spincaloric properties. In phase separated Heusler alloys the increased scattering of phonons at the phase boundaries reduces thermal conductivity and thus improves thermoelectric and spincaloric properties compared to a single-phase compound. [GKB$^+$10, GBB$^+$10, SSO$^+$12] For the characterization of the phase separation, element specific EDX linescans and mappings have

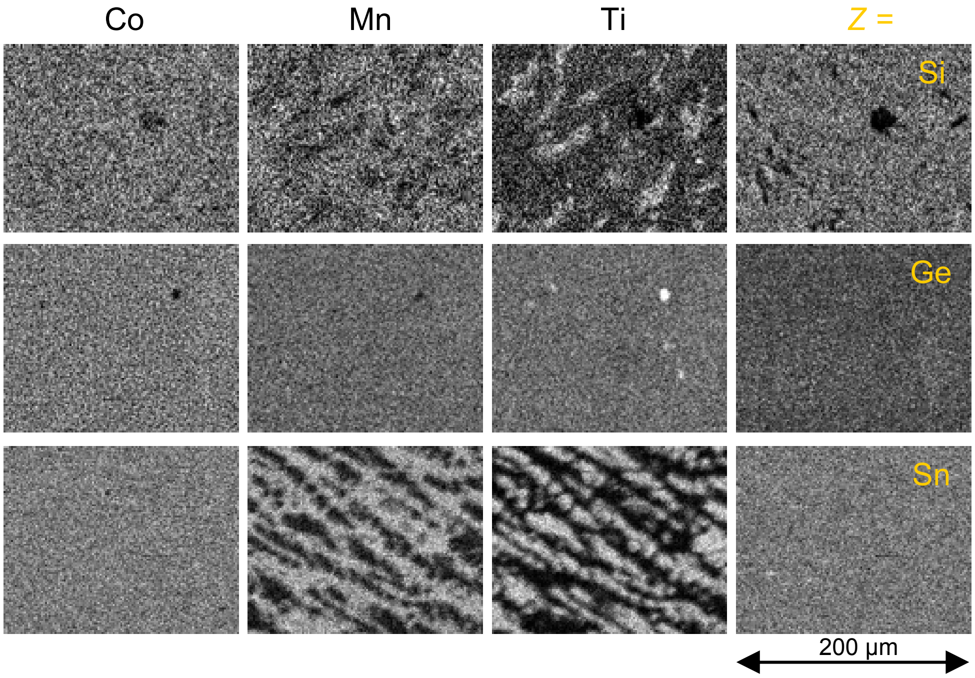

Figure 3.1: Element specific EDX mappings for the Heusler alloys $Co_2(Mn_{0.6}Ti_{0.4})Si$ (first row), $Co_2(Mn_{0.6}Ti_{0.4})Ge$ (second row), and $Co_2(Mn_{0.6}Ti_{0.4})Sn$ (third row). The columns show the elements Co, Mn, Ti and Z = Si, Ge, Sn, respectively. The brightness qualitatively represents the element concentration.

been acquired with a SEM/EDX analysis system.

Fig. 3.1 shows the spatial distribution of the constituents in $Co_2(Mn_xTi_{1-x})Z$ (Z = Si, Ge, and Sn) with $x = 0.6$. In contrast to $Co_2(Mn_xTi_{1-x})Ge$ which has a homogeneous composition, the element specific EDX mappings of $Co_2(Mn_xTi_{1-x})Si$ and $Co_2(Mn_xTi_{1-x})Sn$ reveal a decomposition into a Co_2MnZ-enriched and Co_2TiZ-enriched (with Z = Si, and Sn, respectively) phase.

The different behavior of the three $Co_2(Mn_xTi_{1-x})Z$ series with Z = Si, Ge, and Sn might be explained by the different size of the atoms in the Z position. While Si is smaller and Sn larger compared to Co, Mn, and Ti, Ge has nearly the same size. From the hard sphere model one easily imagines that the internal stress for a mixed compound of unequally sized atoms can be reduced by decomposition. This model is supported by the observation of a smaller lattice constant variation with x for Z = Ge compared to Z = Si, and Sn shown in Fig. 3.2 (values taken from Ref. [GCW$^+$09]).

A reason for the particular shape of decomposed phases are the higher melting points for the Co_2TiZ (Z = Si, Sn) phase compared to the Co_2MnZ (Z = Si, Sn) phase. This leads to an initial crystallization of the Co_2TiZ-enriched phase during cooling, revealing the rounded Co_2TiZ-rich areas in a matrix consisting of the Co_2MnZ-enriched Heusler phase.

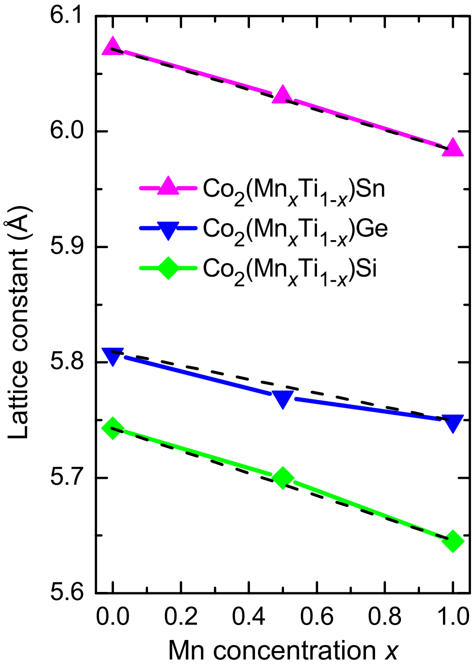

Figure 3.2: Lattice constant variation depending on the Mn concentration for the Heusler series as indicated in the figure. Values taken from Ref. [GCW+09].

In Ref. [GBB+10] the impact of the phase separation on the transport properties is studied in detail. In particular, a reduction of up to 50 % in the thermal lattice conductivity was found, which opens a new way to tune Heulser compounds to overcome the problem of their comparatively high thermal conductivity. As a second example the half-Heulser Co(Mn_xTi_{1-x})Sb with reduced thermal conductivity forms a phase separation into CoTiSb-enriched and CoMnSb-enriched phase as discussed in Ref. [GKB+10].

Another example of a phase separated alloy is $Co_2(Mn_{0.5}Dy_{0.5})Sn$. It is a rare earth compound with an interesting structural decomposition. The sample was prepared by M. Schwall (AK Felser). For more details about the crystal structure measured by XRD, magnetic, and transport properties see Ref. [SSO+12].

Fig. 3.3 (a) shows the distribution of the elements Co, Mn, Dy, and Sn in the phase separated $Co_2(Mn_{0.5}Dy_{0.5})Sn$ compound as measured with the SEM/EDX. One recognizes a pattern with a sixfold symmetry. While the Co concentration is equally distributed, the Dy forms a flower-like six-fold pattern. The Dy-rich regions have a small concentration of Mn and vice versa. Sn also shows a more or less homogeneous distribution except small regions at the grain boundaries. A linear combination of the element-specific EDX mappings shown in Fig. 3.3 (b) reveals three distinct phases. Region I (light blue) shows a sixfold flower pattern embedded in region II (violet). Region III (green) fills the interstitial space within region II.

The EDX line-scan shown in Fig. 3.3 (c) quantifies the stoichiometry of the three regions. Region I with composition $Co_{1.95}Mn_{0.26}Dy_{0.84}Sn_{0.95}$ has the

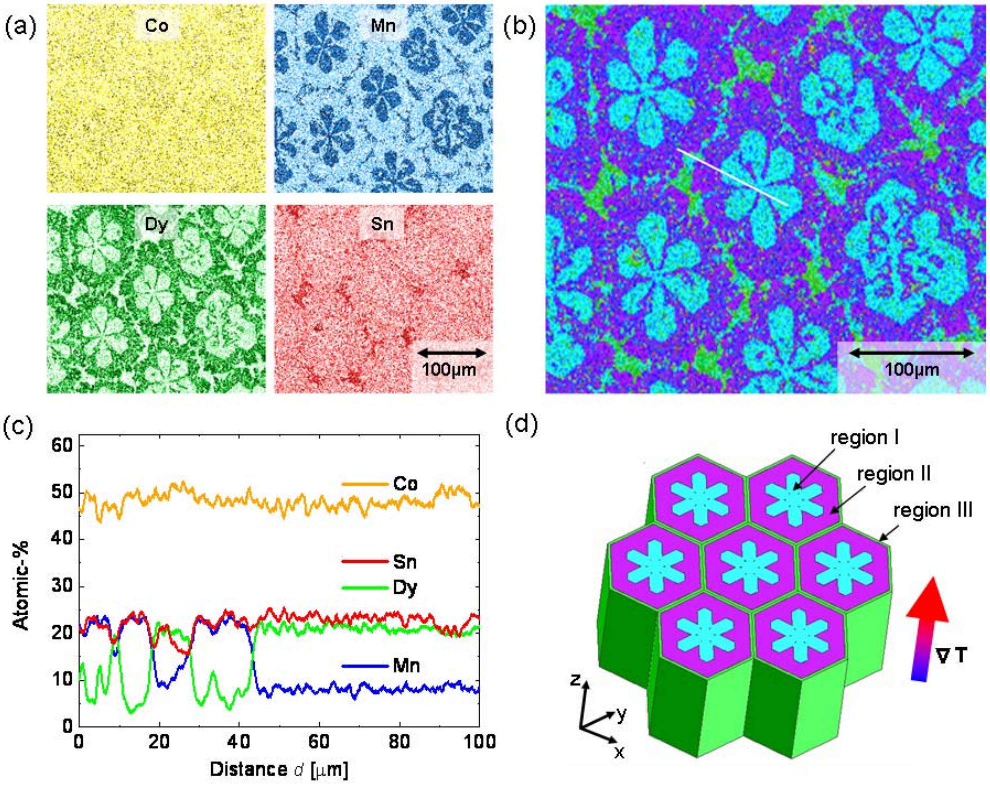

Figure 3.3: (a) Element-specific EDX mappings of the four constituents of the phase separated $Co_2(Mn_{0.5}Dy_{0.5})Sn$ alloy with brightness indicating the relative concentration. (b) Linear combination of the EDX mapping shown in a) revealing three distinct regions with different composition denoted as region I (light blue), region II (violet), and region III (green). (c) Line-scan along the white line in (b). (d) Sketch of the 3-dimensional phase separated $Co_2(Mn_{0.5}Dy_{0.5})Sn$ alloy. Temperature gradient ∇T shows along the z direction.

lowest Mn concentration and forms the flower-like six-fold pattern surrounded by region II with the composition $Co_{1.95}Mn_{0.96}Dy_{0.14}Sn_{0.95}$. Both compositions are formally close to the Heusler alloy $Co_2Mn_{1-x}Dy_xSn$. Region III consists of an intermediate composition $Co_2Mn_{0.45}Dy_{0.83}Sn_{0.72}$. The structure in the lower left corner of Fig. 3.3 (b) reveals an inner pattern, roughly repeating the sixfold flower-like pattern on a smaller scale. All three phases reveal inhomogeneities that could hardly be resolved by EDX. Taking into account the XRD analysis, that has identified cubic $L2_1$ ordered Co_2MnSn and hexagonal $Co_8Dy_3Sn_4$ as pure constituent phases, the observed non-stoichiometric composition for region I and II may be interpreted in the following way: Region I is dominated by $Co_8Dy_3Sn_4$ with additional inclusions of Co_2MnSn amounting to 20 % volume fraction, and region II is dominated by Co_2MnSn with an amount of 10 %.

The SEM and EDX measurements on a surface cut parallel to the temperature gradient reveals parallel stripes at up 1 mm length that can be clearly identified with regions I, region II, and region III. In contrast, EDX images on surfaces perpendicular to the temperature gradient show the flower-like structure (Fig. 3.3). A sketch of the resulting 3-dimensional (3D) structure is shown in Fig. 3.3 (d).

The EDX mappings imply the following growth model explaining the 3D structure: The 3D cellular microstructure is formed by a dendritic crystal growth similar to observations in binary alloys, e.g. Pb-Sn. [TSS94] The different melting points of Co_2MnSn and $Co_8Dy_3Sn_4$ are most likely the origin for the observed cellular microstructure. $Co_8Dy_3Sn_4$ with the highest melting point solidifies as the observed region I in the remaining liquid phase. The sixfold pattern formation in region I originates from the strong epitaxial strain imposed by the hexagonal $Co_8Dy_3Sn_4$ phase with the cubic Co_2MnSn phase formed during the solidifying process. This micro structure is temperature-stable over a wide temperature range, in contrast to $Co_2(Mn_xTi_{1-x})Sn$ and $Co(Mn_xTi_{1-x})Sb$ showing an irregular structure and a disappearance of the phase separation after high temperature annealing.

The lattice thermal conductivity of phase separated $Co_2(Mn_{0.5}Dy_{0.5})Sn$ is lower than the mean value of the single $Co_8Dy_3Sn_4$ and Co_2MnSn phases. [SSO+12] The magnetic properties exist individually in the two $Co_8Dy_3Sn_4$ and Co_2MnSn main phases and the electronic properties are dominated by the $Co_8Dy_3Sn_4$ phase. [SSO+12] Therefore, the observed phase separation represents an example where transport properties are improved compared to a single phase alloy suitable for thermoelectric applications.

3.4 Thin film samples

Thin film samples were prepared by the groups of M. Jordan, G. Jakob, and K. Inomata using magnetron sputtering on transparent substrates (single crystalline substrates MgO, and Al_2O_3). The thickness of the film samples smaller than 100 nm enables the measurement of a photon flux through the film via X-ray luminescence in the substrate. The films were additionally capped by an Al layer to avoid oxidation. Magnetron sputtering deposition is a vapor deposition method via ion bombardment (usually Ar^+ ions) of a target surface. [EB97, HRS04] Ions hitting the target eject atoms and small clusters of the target material which form the growing film on the substrate. To improve structural properties of the sample heating of the substrate during sputtering or sequential post-annealing of the film has been applied.

3.4.1 Mn_2VAl

Epitaxial Mn_2VAl on MgO(100) was grown with a thickness of 60 nm via rf sputtering. Thin films were post-annealed at 550 °C and capped by 4 nm Al layer. The characterization of the Mn_2VAl film by X-ray diffraction revealed a predominant $L2_1$ crystal structure. The sample preparation and crystal structure characterization was done by E. Arbelo-Jorge (AG Jourdan). A detailed description of the used rf sputtering technique and crystal structure measurements can be found in Ref. [AJ11].

3.4.2 Co_2FeAl

Epitaxial Co_2FeAl thin film samples were a courtesy of K. Inomata (Magnetic Materials Center, National Institute for Materials Science (NIMS), 1-2-1 Sengen, Tsukuba 305-0047, Japan). The films are part of an annealing series optimized for TMR devices. 30 nm Co_2FeAl was deposited onto a MgO(100) substrate. After post-annealing at 480 °C the film was capped with a Al/MgO (3 nm/3 nm) layer. The Al/MgO/CoFe layer construction is a typical tunneling magnetoresistor design replacing the Al layer by CoFe. In such tunnel junctions CoFe/MgO/Co_2FeAl using the MgO layer as a tunneling barrier record values of the magnetoresistance of 330% at room temperature were found. [WSS+09] Structural invetigations of the Heusler layer reveal that the Co_2FeAl films always show a B2 atomic order instead of a fully ordered $L2_1$ structure. [OMS+05, WSS+09]

3.4.3 Ni_2MnGa

Ni_2MnGa films were grown by T. Eichhorn (group G. Jakob) with a typical thickness of 100 nm capped by 4 nm of Al by dc magnetron sputtering onto MgO(001) substrates at a substrate temperature of 650 °C [JE07]. A more detailed description of the sputter deposition method, thin film structure investigations, and magnetic properties can be found in Ref. [Eic11].

Temperature dependent XRD confirmed that the Ni_2MnGa thin films show a martensitic phase transition at $T_m = 250$ K. [JE07, JEKE07] Fig. 3.4 (a)

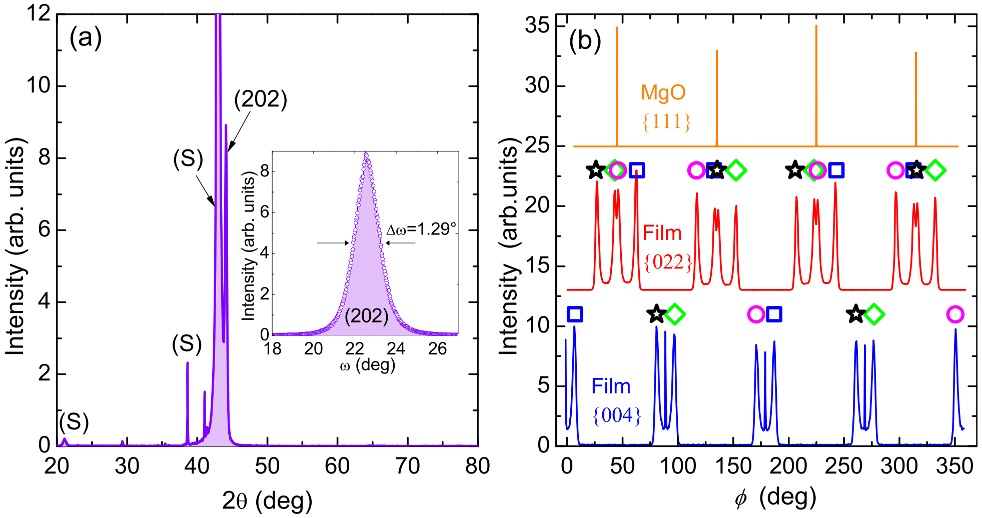

Figure 3.4: (a) Two circle x-ray diffraction in Bragg Brentano geometry of the $Ni_2MnGa(101)/MgO(001)$ film. (b) Room temperature ϕ-scans of the {022} and {004} Ni_2MnGa film and MgO {111} reflections revealing four variants of the cubic phase with respect to the substrate indicated by different symbols. Measurements performed by T. Eichhorn (group G. Jakob).

shows a two circle X-ray diffraction in Bragg Brentano geometry revealing an epitaxial growth of $Ni_2MnGa(101)$ films on MgO(001) as sketched in Fig. 3.5. This naming convention sets the [0k0] direction parallel to the substrate surface, that differs from the orientation in the previously reported (001) orientation on MgO(001) in Ref. [JEKE07]. The high substrate temperature during deposition and small changes in the substrate surface lead to a formation of magnesium hydroxide prior to deposition being responsible for this orientation observed in several samples. For substrates which were stored in vacuum or inert atmosphere prior to deposition a (001) oriented growth was exclusively found. Films with (101) orientation were chosen for the present study because this orientation form a martensitic transformation with twin planes parallel to the surface, thus largely avoiding elastic strain energy in the martensitic phase below $T_m = 250$ K, and a well defined uniaxial magnetic anisotropy as it will be described in Chap. 7.

The lattice constants in the cubic phase are $a_c = b_c = c_c = 0.581$ nm. Fig. 3.5 (a), and (c) show the cubic Ni_2MnGa structure (for temperature T > T_m). For the martensitic phase (T < T_m) the lattice constants are $a_m = 0.607$ nm and $c_m = 0.551$ nm resulting in the martensitic ratio $c/a = 0.91$. Assuming volume conservation one can calculate a value for the lattice constant of $b_m \approx a_c^3/(a_m c_m) \approx a_c$. The values and directions in the martensitic phase have been measured at 120 K. Thus, the martensite phase is in fact orthorhombic leading to twin planes parallel to the surface as sketched in Fig. 3.5 (d).

In-plane twin planes alignment of the Ni_2MnGa film was probed by ϕ-scans shown in Fig. 3.4 (b) of the {022} and {004} reflections that enclose angles of 30° and 45° with the substrate surface, respectively. The ϕ-scans reveal a multivariant growth with respect to the in-plane orientation for the (101) oriented films. In the {004} ϕ-scan actually four variants contribute (marked by different symbols to their respective variants in Fig. 3.4 (b)). The sharp peaks between two {004} reflections are obviously tails of the very strong {022} substrate reflections. This is evident by comparison to a ϕ-scan of 45° rotated in plane {111} substrate reflections. In a single crystal a ϕ-scan of the {004} peaks would give only two reflections corresponding to the (004) and (400) reflection with a (101) plane aligned perpendicular to the ϕ-axis, which will differ by 180° in ϕ.

The ϕ-scan of the {022} Ni_2MnGa reflections confirms the existence of the four variants. The (022) peak appears 54.74° in respect to the (004) peak of the same variant. Counting in the $(0\bar{2}2)$ peak in the opposite rotation direction and the corresponding (220) and $(2\bar{2}0)$ reflections leads in total to 16 peaks in the ϕ-scan of the {022} reflections for the four variants (marked in Fig. 3.4 (b))).

From the X-ray diffraction measurement a tilt of approximately ±8° of the Ni_2MnGa[010] direction and MgO[100] crystal axis of the MgO substrate is found. This tilt can be motivated by inspection of the (101) plane of Ni_2MnGa as viewed in Fig. 3.5 (b). The (101) plane of Ni_2MnGa has a rectangular symmetry, which forms a dense line of atoms along the diagonal of the rectangle enclosing two surface unit cells. The angle between the MgO [100] direction and this diagonal can be calculated by $\arctan(2/\sqrt{2}) = 54.74°$. For the MgO(001) substrate surface the oxygen, and MgO atoms form two fcc sublattices in the plane with dense lines of atoms tilted by 45° in respect to the in-plane MgO [100], and [010] axes. Assuming that the substrate-film interactions lead to a parallel orientation of dense lines, one expects four variants with the Ni_2MnGa[010] film direction showing ±9.74° off from the MgO[100], and MgO[010] direction in close agreement with the experimental observation. The forming of two twin variants parallel to the surface in the martensitc phase leads to eight variants in the Ni_2MnGa film.

Although the structure of the martensitic phase appears complicated (revealing eight variants), the process of averaging upon measuring macroscopic physical properties results in a clear effective uniaxial symmetry. Averaging the two twin variants with their individual c axis oriented at an angle smaller than 45° with respect to the film normal (see Fig. 3.5 (d)) results in a two-fold symmetry within the {010} planes and an effective (short) c'-axis along the surface normal n. This is explicitly calculated in Chap. 7 for the case of magnetic anisotropy. In a similar way the four variants rotated azimuthally at ±8° with respect to the in-plane MgO[100] and [010] axes lead to an effective four-fold symmetry comprising a considerably reduced anisotropy. The remaining uniaxial anisotropy applies to the magnetic anisotropy, to the magnetic orbital moment and to the symmetry of the electronic structure as measured by X-ray absorption. Angular dependent XAS/XMCD will be discussed in detail in Chap. 7.

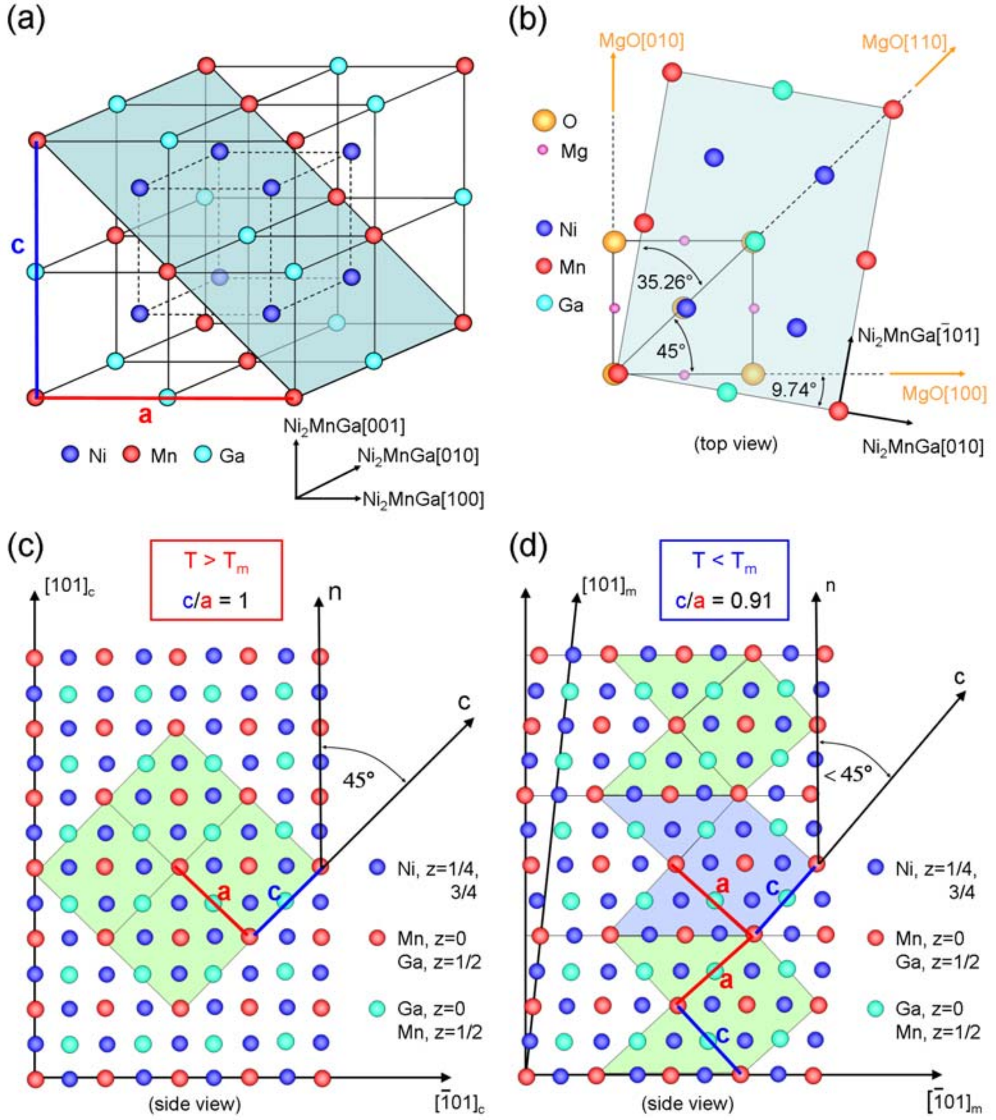

Figure 3.5: (a) Cubic Ni_2MnGa crystal structure (for temperature $T > T_m$). The blue are illustrates the (101) film plane. (b) Top view of the relative orientation of one of the four (or rather eight for $T < T_m$) variants with respect to the substrate. (c) Structural model of the cubic phase ($T > T_m$) neglecting modulation viewed along the Ni_2MnGa[010] axis. (d) Correspondingly, structural model of the martensitic phase ($T < T_m$) with position of the (101) twin planes parallel to the film surface as indicated by the horizontal lines between the blue and green areas.

Chapter 4

Tailoring the electronic band-structure

4.1 Motivation

Recent experimental progress in the fabrication of tunneling magnetoresistance (TMR) devices provides indirect evidence for half-metallic ferromagnetism in Heusler alloys because of the large TMR values [KTHR04, SHO$^+$06, TISI07, TSO$^+$08, TIMS09, TII$^+$09] observed for magnetic tunneling junctions using Co-based Heusler electrodes.

The strong temperature dependence of the TMR effect was attributed to the location of the Fermi energy close to one of the minority band edges. [CSA$^+$08] In order to shift the Fermi energy into the center of the band gap of a Heusler alloy with respect to the minority band gap, a band-structure tailoring through substitution of the transition metal on the Y site or the main group element on the Z site in quaternary compounds has been proposed. [FKW$^+$05, ÖAGS07, FFB07, CSA$^+$08, WSSI08] Shan *et al.* [SSW$^+$09] presented a tunneling spectroscopy study that supports this idea of band-structure tailoring for $Co_2Fe(Al_{0.3}Si_{0.7})$. Sakuraba *et al.* [STK$^+$10] confirmed this idea by an investigation of a $Co_2Fe(Al_{1-x}Si_x)$ series. A shift of the band gap for $Co_2(Fe_xMn_{1-x})Si$ has also been tested by photoemission spectroscopy but without spin resolution. [FBO$^+$07, SEW$^+$08]

A direct study of the band gap is of particular importance to confirm the theoretical concept of a gradual band-structure tailoring. With X-ray magnetic circular dichroism (XMCD) in X-ray absorption spectroscopy (XAS) it is possible to study the element-specific electronic structure, both at surfaces and at buried interfaces. [Stö99, KKS$^+$09] The element-specific and spin-resolved partial density of states (PDOS) can thus be derived directly from the experimental spectra. [KKS$^+$09] In the following a detailed PDOS study of polycrystalline Co_2TiZ (Z = Si, Ge, Sn; Sb), $Co_2(Mn_xTi_{1-x})Si$, $Co_2(Mn_xTi_{1-x})Ge$, and $Co_2Mn(Ga_{1-x}Ge_x)$ alloys will be demonstrated. All compounds with $x = 0$ or $x = 1$ (except Co_2TiSb) have been predicted to be half-metallic ferromagnets. [LLBS05, ÖAGS07] Co_2TiZ (Z = Si, Ge, Sn; Sb) are interesting Heusler alloys because they are less sensitive to local atomic disorder in contrast to many other Heusler alloys. [KKW+07] Substitution of Ti by Mn in Co_2TiSi and Co_2TiGe implies the prospect of combining the robust half-metallic properties of Co_2MnSi and Co_2MnGe with the disorder-resistant properties. The exchange of the fourth main group element by the fifth group element results in normal-metallic ferromagnetic properties. [LLBS05] The idea of substituting the main group element in order to shift the Fermi energy relative to the band gap as proposed for $Co_2Fe(Al_{1-x}Si_x)$ (Ref. [FBO+07] and Ref. [BFF07]) is studied by the $Co_2Mn(Ga_{1-x}Ge_x)$ series. Also, changes of the element-specific spin and orbital moments of the Co and Y elements with composition are determined and compared with theoretical and experimental predictions.

4.2 Element-specific magnetic properties

4.2.1 Co_2TiZ (Z = Si, Ge, Sn; Sb)

Curie temperatures T_C have been determined by SQUID for all three compounds resulting in 380 K for Co_2TiSi, and 355 K for Co_2TiZ (Z = Ge, Sn). For Co_2TiSb the magnetization shows a small magnetization decrease in the temperature range below 400 K representing the maximum available temperature, indicating a much larger value for T_C. The low-temperature (5 K) magnetization values are 1.96 μ_B/f.u., 1.94 μ_B/f.u., 1.97 μ_B/f.u., and 1.67 μ_B/f.u. for Z = Si, Ge, Sn, and Sb, respectively. This is in good agreement with the theoretical value of 2 μ_B/f.u. predicted by the Slater-Pauling rule for Z = Si, Ge and Sn, while for Co_2TiSb a value of 3 μ_B/f.u. is expected. The SQUID measurements were performed by J. Barth (AK Felser) and more details can be found in Ref. [BFB+11].

Fig. 4.1 and 4.2 show XAS/XMCD spectra at the Co and Ti $L_{3,2}$ absorption edges measured at room temperature. After subtracting a constant background from the raw data, the XAS spectra were normalized at the post edge value. The spectra for Z = Si, Ge, and Sn show similar features. The Co XAS signal reveals a characteristic double peak feature at the L_3 edge and a shoulder at the L_2 edge. An additional peak is visible at the L_3 maximum of the XMCD signal. For the case of Z = Sb, the double peak feature is completely absent. The satellite peak at approximately 4 eV above the Co XAS maximum, regularly observed for the Co_2YZ Heusler compounds, [EFV+03] appears only as a weak shoulder for Heusler compounds with Y = Ti. The Ti XAS signal shows a larger maximum at the L_2 edge compared to the L_3 edge, thus reversing the branching ratio expected from an atomic model. This is in agreement with previously measured XAS spectra of metallic Ti. [SWB04] The shape of the Ti XAS signal is similar to that of the pure element spectrum. In contrast, Ti oxide is known to reveal additional multiplet peaks. Their absence confirms the presence of a clean surface. Only after several hours at $p = 1 \cdot 10^{-9}$ mbar the onset of oxide derived XAS peaks was observed. The Ti XMCD signal reveals a complex behavior of alternating positive and negative values for Z = Si, Ge, and Sn. This feature is similar to a reference XMCD spectrum measured for an ultrathin Ti film that was polarized between two ferromagnetic films. [SWB04] From a comparison with this reference spectrum, one can conclude that the Ti

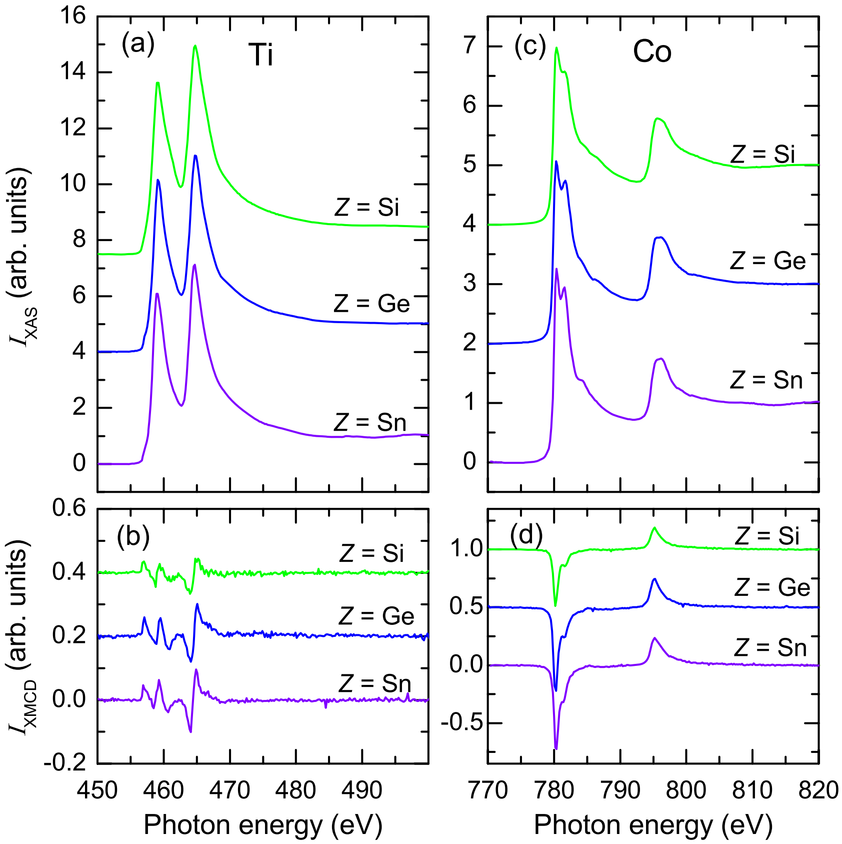

Figure 4.1: (a), and (c) X-ray absorption spectra I_{XAS} for $\mathrm{Co_2Ti}Z$ (Z = Si, Ge, and Sn) measured at the Ti, and Co $\mathrm{L}_{3,2}$ edge averaged from total electron yield intensities I^+ and I^- for magnetization direction parallel and antiparallel to the X-ray polarization. (b), and (d) corresponding XMCD spectra $I_{\mathrm{XMCD}} = I^+ - I^-$ on the same scale.

magnetic moment is antiparallel to the Co moment. Therefore, $\mathrm{Co_2Ti}Z$ (Z = Si, Ge, and Sn) are ferrimagnetic compounds. For Z = Sb, the Ti XMCD signal vanishes within error limits (see Fig. 4.2).

The Co XAS spectrum of $\mathrm{Co_2TiSn}$ measured by Yamasaki *et al.* (Ref. [YIA$^+$02]) differs from the spectra observed here. It revealed three peaks with a separation of 0.5 eV at the L_3 edge instead of two peaks. This feature was then interpreted as a multiplet effect. However, as shown in Sec. 2.1.4, the multiplet calculation neither reproduces the experimentally observed XAS and XMCD spectra of Ref. [YIA$^+$02] nor the spectra observed here. XAS/XMCD spectra calculated by Bekenov *et al.* (Ref. [BASY05]), using an *ab initio* local-density approximation (LDA) approach, revealed a sharp maximum at the L_3 edge followed by a distinct shoulder at the trailing edge 1 eV above the maximum. This is in fair agreement with the spectra observed in this work. According to the band-structure calculations, the double peak at the L_3 edge observed for Z = Si, Ge, and Sn originates from a twin peak of the minority PDOS 0.5 eV above E_F with the peak at higher energy attributed to a localized Co-Ti hy-

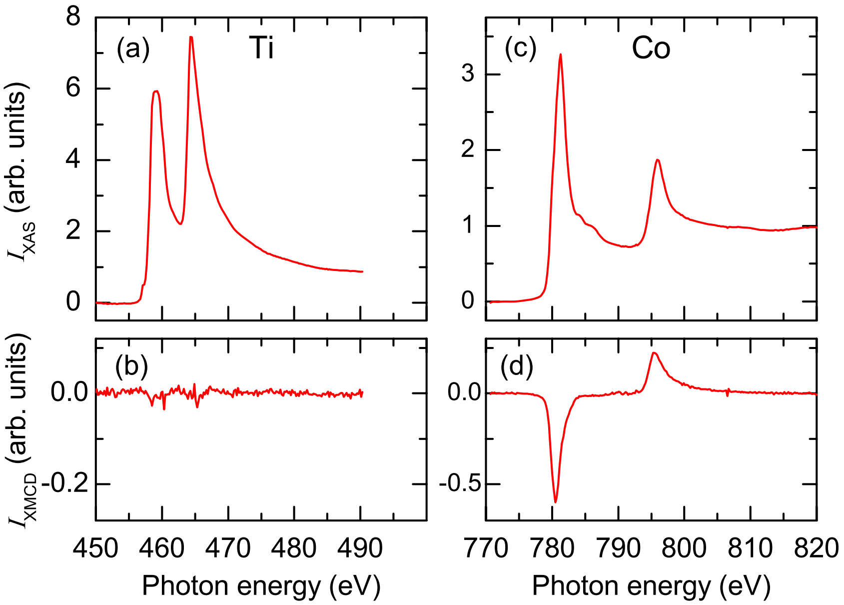

Figure 4.2: (a), and (c) X-ray absorption spectra I_{XAS} for $\mathrm{Co_2TiSb}$ measured at the Ti, and Co $\mathrm{L}_{3,2}$ edge averaged from total electron yield intensities I^+ and I^- for magnetization direction parallel and antiparallel to the X-ray polarization. (b), and (d) corresponding XMCD spectra $I_{\mathrm{XMCD}} = I^+ - I^-$ on the same scale.

bridization state. $\mathrm{Co_2TiSb}$ has a different band structure. Due to the increased number of valence electrons, the minority band gap is shifted below E_F and a PDOS minority maximum coincides with E_F. [LLBS05] Thus, the pronounced differences between Z = Si, Ge, Sn, and Z = Sb can be traced back to the pronounced difference of the PDOS.

Spin and orbital moments, that were calculated using the sum rules, are summarized in Tab. 4.1. $N_h(\mathrm{Co}) = 2.5$, and $N_h(\mathrm{Ti}) = 8$ was assumed for the number of $3d$ holes. The dipole term was neglected for the calculation of the spin moment. This contribution cancels for the polycrystalline samples investigated here. [CIL$^+$95] The selfabsorption correction [NSI99] is also dispensed, because this correction is smaller than the statistical error for the compounds investigated here. For $\mathrm{Co_2TiGe}$ and $\mathrm{Co_2TiSn}$, the sum-rule analysis led to very large values and opposite sign of the orbital moments. In these two cases, the magnetic moment of Ti was determined by a comparison of XMCD peak heights with data from Z = Si. The sum of the atomic moments μ_{XMCD} agrees well with the magnetization determined by SQUID magnetometry except for the case of Z = Si. In this case, XMCD leads to a slightly smaller value, which might be explained by a nonsaturated magnetization due to the limitation of the external field ($\mu_0\mathrm{H} = 1.2$ T) for the XMCD measurement. For all $\mathrm{Co_2Ti}Z$ compounds, the magnetization is clearly dominated by the Co spin moment and a relatively large contribution of the Co orbital moment.

	μ	Co	Ti	$\mu_{\text{Co}}/\mu_{\text{Ti}}$
Z = Si	μ_{spin}	0.36 ± 0.02	-0.02 ± 0.02	-36
	μ_{orb}	0.02 ± 0.02	0.00 ± 0.02	
	μ_{XMCD}	0.75 ± 0.12		
	μ_{SQUID}	1.21 ± 0.10		
Z = Ge	μ_{spin}	0.49 ± 0.02	-0.03 ± 0.02	-33
	μ_{orb}	0.07 ± 0.02	0.00 ± 0.02	
	μ_{XMCD}	1.09 ± 0.12		
	μ_{SQUID}	1.22 ± 0.10		
Z = Sn	μ_{spin}	0.56 ± 0.02	-0.03 ± 0.02	-37
	μ_{orb}	0.05 ± 0.02	0.00 ± 0.02	
	μ_{XMCD}	1.19 ± 0.12		
	μ_{SQUID}	1.28 ± 0.10		
Z = Sb	μ_{spin}	0.67 ± 0.02	0.00 ± 0.02	
	μ_{orb}	0.05 ± 0.02	0.00 ± 0.02	
	μ_{XMCD}	1.44 ± 0.12		
	μ_{SQUID}	1.62 ± 0.10		

Table 4.1: Element-specific magnetic spin moment μ_{spin} (μ_B per atom) and orbital moment μ_{orb} (μ_B per atom) for $\text{Co}_2\text{Ti}Z$ at $T = 300$ K as calculated from the sum rules. The total moment μ_{XMCD} (μ_B per formula unit) results from weighted sum of the atomic moments. For the number of unoccupied $3d$ states the values $N_h(\text{Co}) = 2.5$, and $N_h(\text{Ti}) = 8$ were assumed. Total magnetic moment μ_{SQUID} (μ_B per formula unit) measured by SQUID magnetometry at $T = 300$ K is given for comparison. SQUID measurement performed by J. Barth (AK Felser).

4.2.2 $Co_2(Mn_xTi_{1-x})Si$

In order to measure properties close to the ground state, for most of the compounds T_C increases from 380 K for Co_2TiSi to 985 K for Co_2MnSi, the XAS measurements were performed at 150 K, i.e., at a temperature where the thermal decrease in the magnetization is comparatively small for all compounds. Only the $x = 0$ sample was measured at 300 K as already discussed in Sec. 4.2.1. For consideration of the thermal magnetization decrease, the room-temperature XMCD signal of this sample was multiplied by a factor of 1.66 in order to compare with results of the other compounds. The factor reflects the magnetization ratio $M(T)/M(T = 0\ \text{K})$ measured by SQUID. Fig. 4.3 shows XAS/XMCD spectra at the Co and Mn $L_{3,2}$ absorption edges. As for Co_2TiZ, after subtracting a constant background from the raw data, the XAS spectra were normalized at the post-edge value. The characteristic double peak features of the Co XAS and XMCD signal gradually vanish with decreasing Ti concentration. For Co_2MnSi, a very pronounced peak at 4 eV above the XAS maximum is observed in agreement with previously published spectra. [TKvdL$^+$08, SKS$^+$04] The fine structure of the L_3 XMCD maximum discussed in Ref. [TKvdL$^+$08] is also confirmed.

The Mn XMCD signal for $x = 1$ reveals a weak doublet structure at the Mn L_2 edge. A similar splitting of the Mn L_2 XAS peak is observed for Mn oxide, however, with a larger width of the splitting and also accompanied by additional peaks at the L_3 edge. [KEB$^+$06] Moreover, for Mn oxide, the double peak would not show up in the XMCD spectra since the Mn oxide has no magnetic moment. Other proposed explanations for the Mn multiplet features referring to interface effects [GBN$^+$05] are not applicable in our case since we investigate an uncoated surface. Instead, the Mn L_2 double peak can be explained by a multiplet effect [KKE$^+$09] invoked by the localized character of the Mn states. [MIK$^+$03]

For the $Co_2(Mn_xTi_{1-x})Si$ series, the number of valence electrons N_v increases from 26 to 29. Hence, the magnetization is expected to increase linearly from 2 μ_B/f.u. to 5 μ_B/f.u. per formula unit with increasing Mn concentration. This expectation is roughly confirmed by the experiment (see Tab. 4.2). The Co moment is approximately 1 μ_B/atom. The Mn moment is also fairly constant independent on x. Therefore, the magnetization increase with increasing x is mainly caused by the replacement of Ti with nearly zero moment by Mn with a large moment ($\approx 3.3\ \mu_B$/atom). The total magnetization for the mixed compounds is slightly larger than predicted by the Slater-Pauling rule. This was also observed in the case of a $Co_2Mn_{1-x}Fe_xAl$ series. [JFB$^+$09] The Co orbital to spin moment ratio $\mu_{\text{orb}}/\mu_{\text{spin}}$ is larger for the mixed compounds than for $x = 0$ and $x = 1$. The increased orbital moment is tentatively attribute to the internal stress and local deviation of individual unit cells from their averaged cubic symmetry. The random replacement of Ti by the smaller Mn atom therefore acts as a point defect. This model is in agreement with the single phase observed in XRD (Chap. 3) because diffraction is exclusively sensitive to the translational symmetry on a much larger scale. However, a local decomposition into a few number of complete Co_2MnSi and Co_2TiSi unit cells cannot be fully

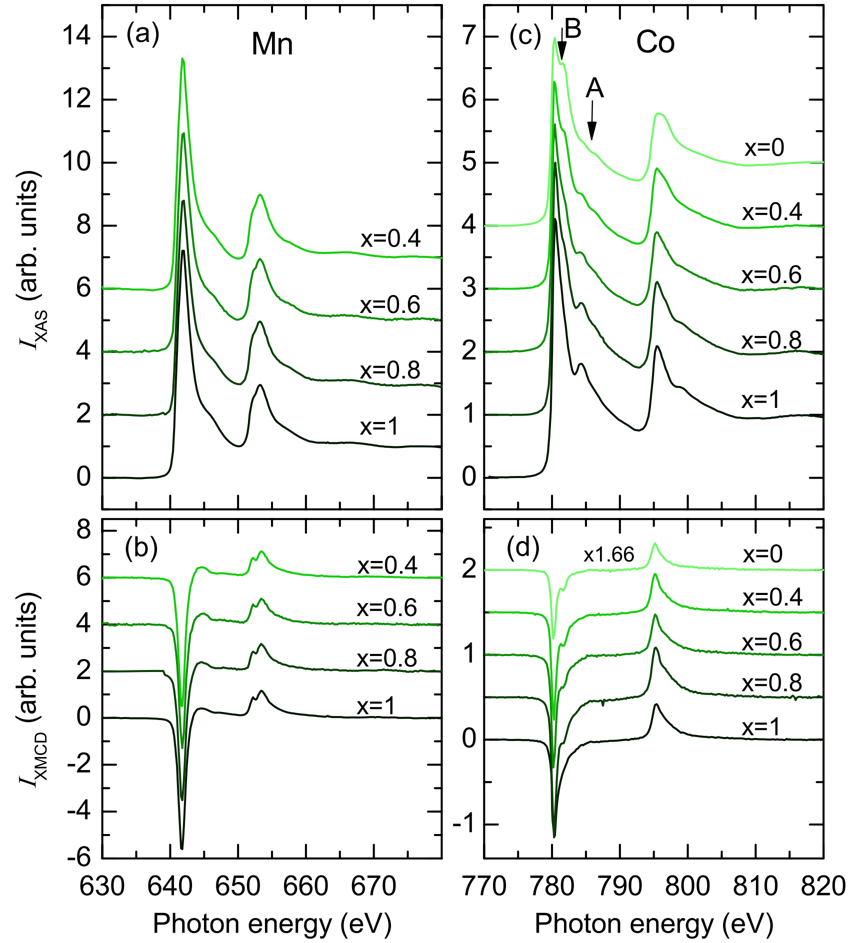

Figure 4.3: (a), and (c) X-ray absorption spectra I_{XAS} for $\mathrm{Co_2(Mn}_x\mathrm{Ti}_{1-x}\mathrm{)Si}$ measured at the Mn, and Co $\mathrm{L}_{3,2}$ edge averaged from total electron yield intensities I^+ and I^- for magnetization direction parallel and antiparallel to the X-ray polarization. (b), and (d) corresponding XMCD spectra $I_{\mathrm{XMCD}} = I^+ - I^-$ on the same scale (note the scaling factor for $x = 0$).

	μ	Co	Mn	Ti
$x = 0.0$	μ_{spin}	0.60 ± 0.02		-0.03 ± 0.02
	μ_{orb}	0.02 ± 0.02		-0.00 ± 0.02
	μ_{XMCD}	1.25 ± 0.12		
$x = 0.4$	μ_{spin}	0.88 ± 0.02	3.37 ± 0.10	0
	μ_{orb}	0.07 ± 0.02	0.11 ± 0.05	0
	μ_{XMCD}	3.29 ± 0.20		
$x = 0.6$	μ_{spin}	0.90 ± 0.02	3.08 ± 0.10	0
	μ_{orb}	0.05 ± 0.02	0.12 ± 0.05	0
	μ_{XMCD}	3.82 ± 0.20		
$x = 0.8$	μ_{spin}	0.97 ± 0.02	3.39 ± 0.10	0
	μ_{orb}	0.09 ± 0.02	0.21 ± 0.05	0
	μ_{XMCD}	5.00 ± 0.20		
$x = 1$	μ_{spin}	0.72 ± 0.02	3.34 ± 0.10	
	μ_{orb}	0.05 ± 0.01	0.11 ± 0.05	
	μ_{XMCD}	4.99 ± 0.20		

Table 4.2: Element-specific magnetic spin moment μ_{spin} (μ_B per atom) and orbital moment μ_{orb} (μ_B per atom) for $\text{Co}_2(\text{Mn}_x\text{Ti}_{1-x})\text{Si}$ at $T = 150$ K as calculated from the sum rules. The total moment μ_{XMCD} (μ_B per formula unit) results from weighted sum of the atomic moments. For the number of unoccupied $3d$ state the values $N_h(\text{Co}) = 2.5$, $N_h(\text{Mn}) = 4.5$ and for Mn a jj-mixing correction factor $c_{jj} = 1.5$ were assumed. Values for $x = 0$ are included for comparison from Sec. 4.2.1 and multiplied by a factor of 1.66 for consideration the thermal magnetization decrease. Ti moments could not be determined for x > 0 because of the limited signal-to-noise ratio and are assumed to be zero for calculation of μ_{XMCD}.

excluded. In this case, the internal stress would also destroy the local cubic symmetry and increase the orbital moment.

4.2.3 $\text{Co}_2(\text{Mn}_x\text{Ti}_{1-x})\text{Ge}$

XAS/XMCD results are shown in Fig. 4.4 for the $\text{Co}_2(\text{Mn}_x\text{Ti}_{1-x})\text{Ge}$ series measured at the Ti, Mn, and Co $\text{L}_{3,2}$ edges. All measurements (except $x = 0$, which is included from Sec. 4.2.1 and multiplied by a factor of 1.66 for consideration the thermal magnetization decrease) were performed at 110 K. The Co XAS spectra in Fig. 4.4 (e) reveal the largest change with composition. Similar changes occur at the L_3 edge and L_2 edge. Replacing Ti by Mn causes a vanishing of the second maximum (~ 1 eV above L_3 maximum) and an arising satellite peak B (~ 3 eV above L_3 maximum). Peak A represents a dominant Co-Ti d-band hybridization state. The satellite peak B corresponds to a Co-Mn sd-band hybridization state and was described as characteristic for highly ordered Heusler compounds. [TKvdL$^+$06] In the quaternary Heusler alloy Mn has also some effects on the Ti states and the corresponding XMCD spectra. A systematic change in the peak height and an additional feature at 470 eV occurs in the Ti XMCD spectra (marked in Fig. 4.4 (b)).

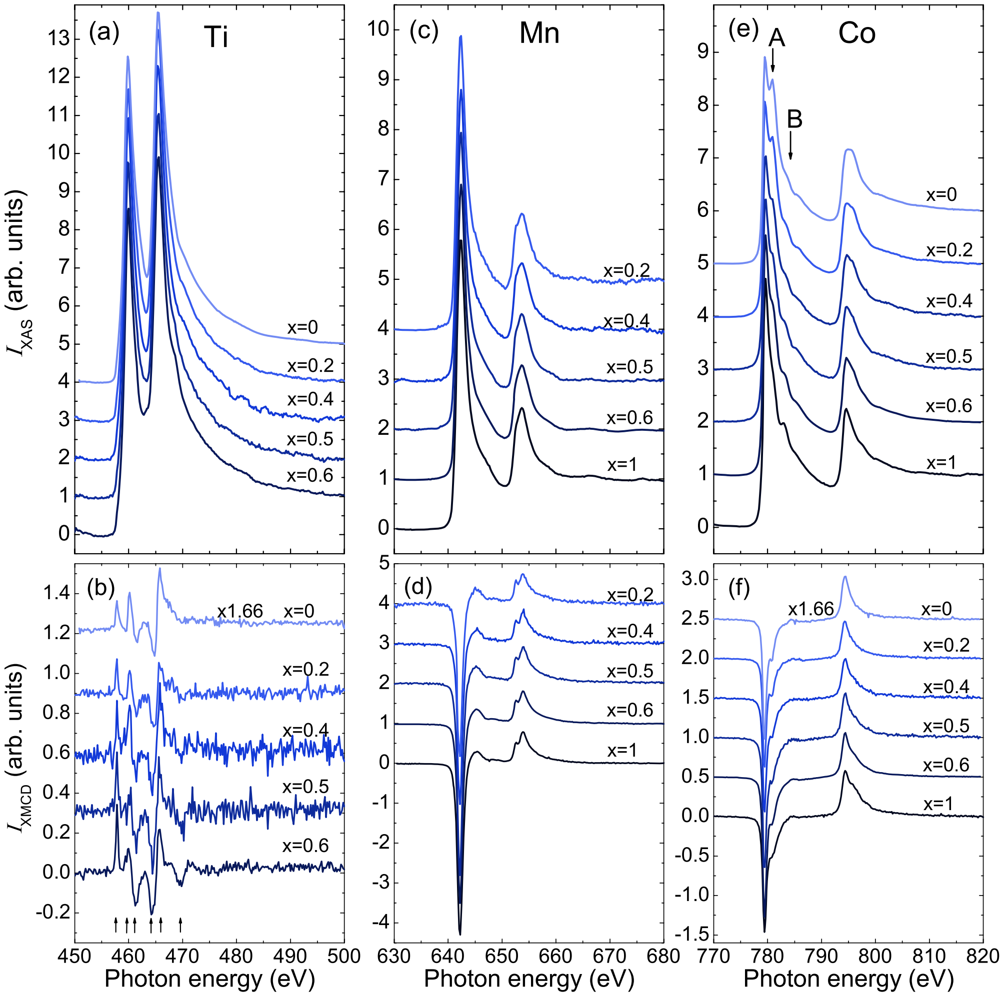

Figure 4.4: (a), (c), and (e) X-ray absorption spectra I_{XAS} for $Co_2(Mn_xTi_{1-x})Ge$ measured at the Ti, Mn, and Co $L_{3,2}$ edges averaged from total electron yield intensities I^+ and I^- for magnetization direction parallel and antiparallel to the X-ray polarization. (b), (d), and (f) corresponding XMCD spectra $I_{\mathrm{XMCD}} = I^+ - I^-$ on the same scale.

	μ	Co	Mn	Ti
$x = 0.0$	μ_{spin}	0.69 ± 0.02		-0.03 ± 0.05
	μ_{spin}(LDA)	1.05		-0.05
	μ_{orb}	0.06 ± 0.01		
$x = 0.2$	μ_{spin}	0.62 ± 0.02	3.18 ± 0.10	-0.04 ± 0.05
	μ_{orb}	0.05 ± 0.01	0.03 ± 0.05	
$x = 0.4$	μ_{spin}	0.68 ± 0.02	3.21 ± 0.10	-0.04 ± 0.05
	μ_{orb}	0.05 ± 0.01	0.04 ± 0.05	
$x = 0.5$	μ_{spin}	0.79 ± 0.02	3.84 ± 0.10	-0.05 ± 0.05
	μ_{spin}(LDA)	1.01	3.19	-0.1
	μ_{orb}	0.08 ± 0.01	0.11 ± 0.05	
$x = 0.6$	μ_{spin}	0.81 ± 0.02	3.64 ± 0.10	-0.06 ± 0.05
	μ_{orb}	0.08 ± 0.01	0.04 ± 0.05	
$x = 1.0$	μ_{spin}	0.93 ± 0.02	3.25 ± 0.10	
	μ_{spin}(LDA)	1.02	3.05	
	μ_{orb}	0.00 ± 0.01	0.24 ± 0.05	

Table 4.3: Element-specific magnetic spin moment μ_{spin} (μ_B per atom) and orbital moment μ_{orb} (μ_B per atom) per atom for Co$_2$(Mn$_x$Ti$_{1-x}$)Ge at $T = 110$ K as calculated from the sum rules. The total moment μ_{XMCD} (μ_B per formula unit) results from weighted sum of the atomic moments. For the number of unoccupied $3d$ states the values $N_h(\text{Co}) = 2.5$, $N_h(\text{Mn}) = 4.5$ and $N_h(\text{Ti}) = 8$ and for Mn a jj-mixing correction factor $c_{jj} = 1.5$ were assumed. Values for $x = 0$ are included for comparison from Sec. 4.2.1 and multiplied by a factor of 1.66 for consideration the thermal magnetization decrease. Theoretical magnetic spin moment μ_{spin}(LDA) from the LDA+U calculation is given for comparison. Theoretical calculations done by G. H. Fecher (AK Felser).

From element-specific XMCD spectra the derived magnetic spin moment μ_{spin} and magnetic orbital moment μ_{orb} are listed in Tab. 4.3. Similar experimental moments were reported [MKI$^+$04] for Co$_2$MnGe ($x = 1$) with slightly larger Co and smaller Mn orbital moments. Theoretical results for Co$_2$MnGe (Tab. 4.3) coincide with previously reported data. [SRK$^+$06] The theoretical calculataions were performed by G. H. Fecher (AK Felser, see also Chap. 4.3.3). Co$_2$(Mn$_x$Ti$_{1-x}$)Ge is a ferrimagnet due to the antiparallel magnetic moments of Ti and Co/Mn. The increase in the Mn content leads to a strong increase in the negative Ti magnetic moment. The Co spin moment slightly increases with x and the Mn spin moment remains almost constant.

Fig. 4.5 shows the XMCD corresponding total magnetic moments and the measured SQUID values at 110 K. The SQUID measurements were done by B. Balke (AK Felser). The experimental results are not far away from the Slater-Pauling curve and the *ab initio* local-density approximation plus U (LDA+U) calculations (only spin magnetic moments). Remarkable is the Slater-Pauling curve crossing of the total magnetic moment at $x = 0.5$ derived from XMCD. Crystalline disorder has a direct effect on the magnetic moment. B2 disorder in the samples is hardly avoidable and leads to an increased magnetic moment

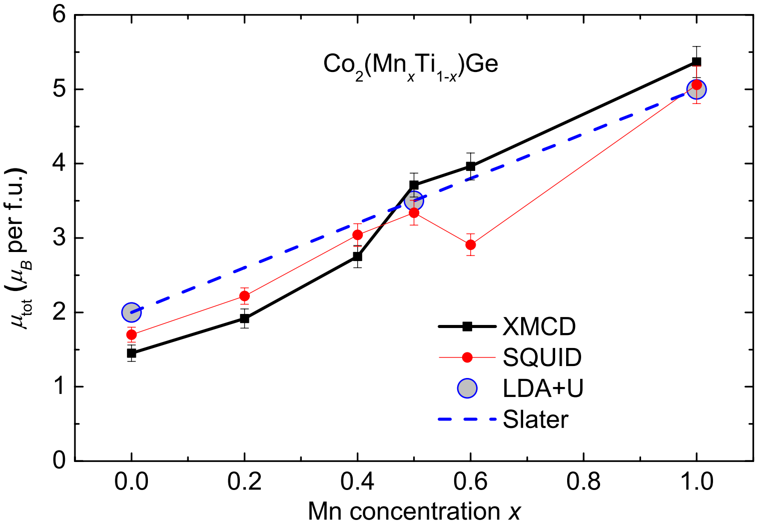

Figure 4.5: Total magnetic moments μ_{tot} (μ_B per formula unit) for Co$_2$(Mn$_x$Ti$_{1-x}$)Ge investigated at 110 K with SQUID (measured by B. Balke (AK Felser)) and XMCD as a function of the Mn concentration. The dashed line indicates the Slater-Pauling rule. LDA+U values (calculated by G. H. Fecher (AK Felser)) from weighted sum of the atomic spin moments are given for comparison.

for $x > 0.5$ (in the ferromagnetic dominated case) and a decreased magnetic moment for $x < 0.5$ (ferrimagnetic dominated case).

4.2.4 Co$_2$Mn(Ga$_{1-x}$Ge$_x$)

Because the Curie temperature T_C at approximately 900 K for the whole series is very high, the XAS/XMCD measurements were performed at room temperature. The magnetization measured by SQUID magnetometry revealed a reduction of 5 % at room temperature from its low-temperature value at 5 K. The magnetization increases linearly from 4 μ_B/f.u. to 5 μ_B/f.u. with increasing Ge concentration in close agreement with the Slater-Pauling rule.

Fig. 4.6 shows XAS/XMCD spectra at the Co and Mn L$_{3,2}$ absorption edges measured at room temperature. Similar to the case of Co$_2$(Mn$_x$Ti$_{1-x}$)Z (Z = Si, Ge), the Mn XMCD signal (Fig. 4.6 (b)) reveals a doublet feature at the Mn L$_2$ edge in agreement with an earlier observation [MIK$^+$03] for Co$_2$MnGe. The double peak feature becomes less prominent with decreasing Ge concentration, indicating a decrease in the localization similar to the case of Co$_2$MnAl and Co$_2$MnSi discussed in Ref. [TKvdL$^+$08].

The Co XAS spectra of Co$_2$MnGe reveal the Heusler peak A at 3 eV above the L$_3$ maximum in accordance with the spectra reported in Ref. [MIK$^+$03]. This extra peak shifts continuously to 4 eV above the maximum with decreasing Ge concentration. One would not expect this continuous shift, if the local structure was decomposed in Ge and Ga rich areas. Therefore, the Co XAS spectra of

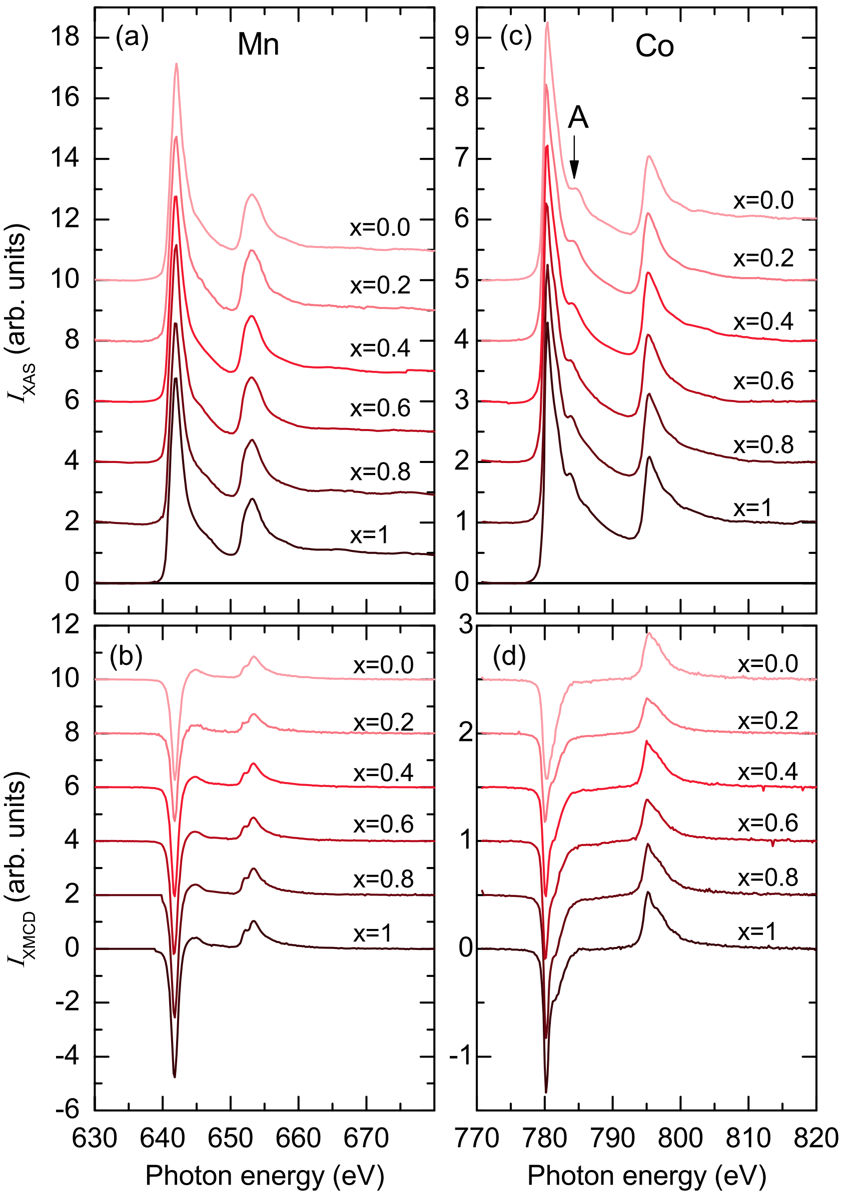

Figure 4.6: (a), and (c) X-ray absorption spectra I_{XAS} of $\mathrm{Co_2Mn(Ga_{1-x}Ge_x)}$ at the Mn, and Co $L_{3,2}$ edge averaged from total electron yield intensities I^+ and I^- for magnetization direction parallel and antiparallel to the X-ray polarization. (b), and (d) corresponding XMCD spectra $I_{\mathrm{XMCD}} = I^+ - I^-$ on the same scale.

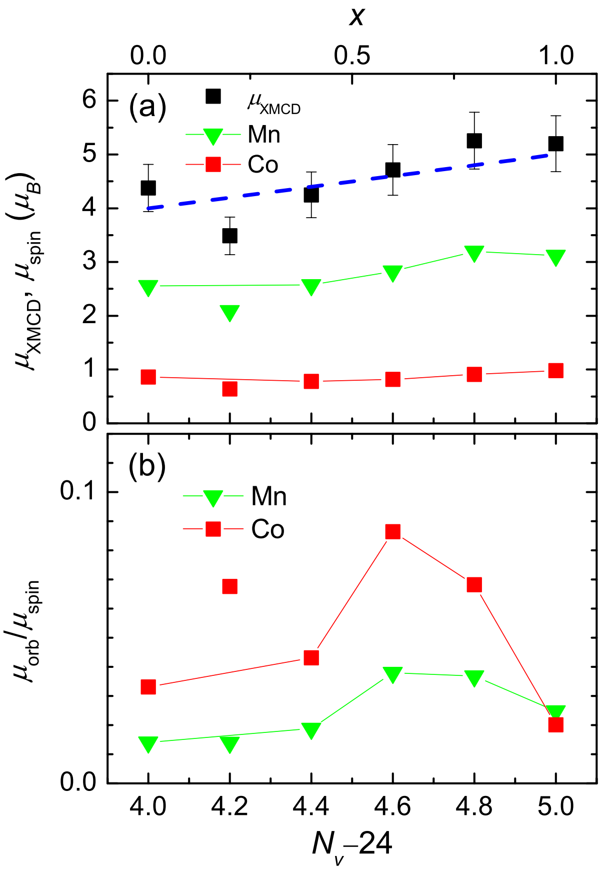

Figure 4.7: (a) Total magnetic moment μ_{XMCD} (μ_B per formula unit) and element-specific magnetic spin moment μ_{spin} (μ_B per atom) for $\mathrm{Co_2Mn(Ga_{1-x}Ge_x)}$ measured at 300 K with XMCD as a function of the Ge concentration. μ_{XMCD} results from weighted sum of the atomic moments. For the number of unoccupied $3d$ states the values $N_h(\mathrm{Co}) = 2.5$, $N_h(\mathrm{Mn}) = 4.5$ and for Mn a jj-mixing correction factor $c_{jj} = 1.5$ were assumed. The dashed line indicates the Slater-Pauling rule. (b) Ratio of the orbital magnetic moment over the spin magnetic moment.

this series unambiguously prove the formation of a Heusler structure with the Z sites randomly occupied by Ge and Ga.

The XMCD maximum at the Co L_3 edge shows a shoulder at around 1.5 eV above the maximum. A similar feature was observed in Ref. [MIK$^+$03] and also in the case of the isoelectronic compound $\mathrm{Co_2MnSi}$ (see Sec. 4.2.2 and Ref. [KEB$^+$06]). The shoulder has been ascribed to the separated minority states with e_g and t_{2g} symmetries. [MIK$^+$03]

The Co and Mn magnetic spin moments calculated by the sum-rule analysis increase with increasing Ge concentration as shown in Fig. 4.7 (a). The weighted sum of Co and Mn spin and orbital moments obeys the Slater-Pauling rule. The sample with $x = 0.2$ shows an exceptional low value, which might be traced back to the poorer homogeneity observed by the EDX analysis for this particular sample.

The orbital to spin moment ratio (Fig. 4.7 (b)) shows a pronounced maximum between $x = 0.6$ and $x = 0.8$. As for the case of $Co_2(Mn_xTi_{1-x})Si$, the orbital moment increase can be attributed to the internal stress and local deviation of individual unit cells from their averaged cubic symmetry. Because, a local decomposition can be excluded for the $Co_2Mn(Ga_{1-x}Ge_x)$ series, the Ga atoms act as point defects in the Co_2MnGe structure. The particularly low values of the orbital moments in the case of $x = 0$ (0.03 μ_B/atom) and $x = 1$ (0.02 μ_B/atom) are in very good agreement with theoretical predictions [0.02 μ_B/atom for $x = 1$ (Ref. [PCF02]) and $0.01 - 0.02$ μ_B/atom for $x = 0$ (Ref. [SRK$^+$06])].

4.3 Spin-resolved unoccupied density of states

4.3.1 Co_2TiZ (Z = Si, Ge, Sn; Sb)

Fig. 4.8 shows the Co PDOS for the sample series Co_2TiZ (Z = Si, Ge, Sn, and Sb) recovered from the L_3 edge data including a scaling factor $M(0)/M(T)$ for the case of Z = Si, Ge and Sn. The Co PDOS for Z =Si, Ge, and Sn look similar to each other which can be expected because the compounds are isoelectronic to each other. [LLBS05] For all samples, the majority PDOS shows a characteristic double step increase at E_F although the steps are less pronounced for the cases of Z = Ge, Sn, and Sb compared to Z = Si. The double step indicates the simultaneous presence of itinerant and localized majority states at E_F.

In the following, it is assumed that the contribution of the itinerant band is constant for all Co-based Heusler compounds. This assumption is supported by the fact that calculations reveal a similar width of the itinerant band (approximately 4 eV) for all these compounds. The contribution from the itinerant band is approximated by a steplike function with slowly decreasing intensity for increasing energy. The same function for all samples has been used and the function was shifted along the energy axis in order to fit the onset of the itinerant contribution to the majority bands. Then from the 50 % point of the step function the correlation energy $\Delta E_C = 0.5$ eV was subtracted in order to determine E_F corresponding to the localized majority and minority contributions to the PDOS.

The minority PDOS shows a pronounced maximum at $E_{v,max} - E_F = 0.5$ eV. The maximum is related to the unoccupied Co e_g state. [LLBS05] The binding energy of this state is in accordance with most calculations. [LLBS05,KFF07] In contrast, Ref. [HHHJ06] predicts much larger values ($E_{v,max} - E_F = 1 - 2$ eV) for Co_2TiSn depending on the calculation scheme. From comparison with theory, the second maximum of the minority PDOS at $E - E_F = 2$ eV is identified as a localized Co-Ti hybridization state of t_{2g} character. It is this pronounced t_{2g} hybridization peak that causes the double peak feature in the Co XAS spectra (Fig. 4.1 (c)).

Upon approaching E_F the minority PDOS rapidly decreases but does not vanish at E_F. Therefore, Co_2TiZ with Z = Si, Ge, and Sn are at the boundary of being half-metallic with E_F positioned at the minority conduction band edge.

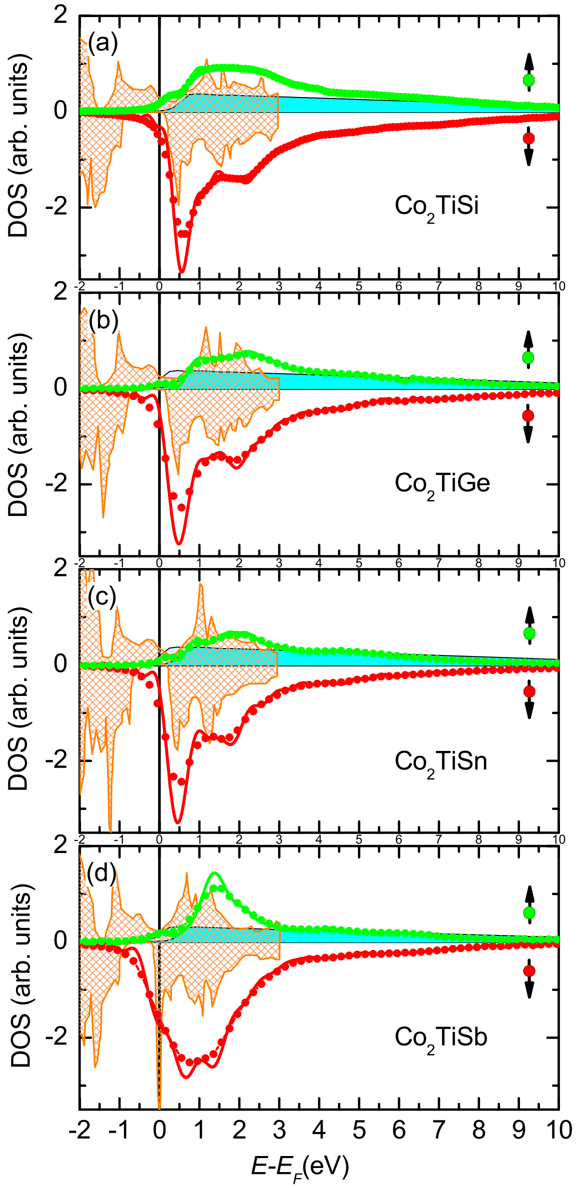

Figure 4.8: Spin-resolved Co PDOS calculated from the XAS/XMCD data measured at the Co L_3 edge for Co_2TiZ samples as indicated in the Figure. Full lines indicate deconvoluted data. Full lines with shadings indicate the function used for approximation of the itinerant band as measured (blue) and shifted by ΔE_C (gray). Theoretical total DOS data from Ref. [LLBS05] is shown by an orange patterned area.

For Co_2TiSb the minority PDOS does not decrease close to E_F but instead reveals a shoulder directly at E_F. This reflects the metallic behavior of this particular compound in agreement with a calculation by Lee et al. [LLBS05].

4.3.2 $\mathbf{Co_2(Mn_xTi_{1-x})Si}$

For the $Co_2(Mn_xTi_{1-x})Si$ series shown in Fig. 4.9, the minority feature caused by the Co-Ti t_{2g} state gradually decreases with decreasing Ti concentration. For Co_2MnSi the corresponding Co-Mn t_{2g} state produces a much weaker feature at a slightly larger energy in accordance with calculations. [GMD06] A gradual shift of the minority maximum with the change of composition is not observed. Instead, $E_{v,max}$ remains at 0.5 eV above E_F with increasing Mn concentration for $x \leq 0.8$ and increases to 0.9 eV for $x = 1$. As discussed in Chap. 3, the $Co_2(Mn_xTi_{1-x})Si$ series shows a decomposition into a Mn-rich (nearly poor Co_2MnSi) and a Ti-rich (nearly poor Co_2TiSi) phase. This means that the PDOS for $0 < x < 1$ has to be seen as a linear combination of $Co_2(Mn_xTi_{1-x})Si$ with $x = 0$ and $x = 1$.

4.3.3 $\mathbf{Co_2(Mn_xTi_{1-x})Ge}$

Self-consistent electronic structure calculations were carried out using the full potential linearized augmented plane wave method as implemented in WIEN2K. [BSM$^+$01] Further details for the *ab initio* LDA+U calculations done by G. H. Fecher (AK Felser) can be found in Ref. [KFF07]. As previously discussed [GDP02] the theoretical results for $Co_2(Mn_xTi_{1-x})Ge$ ($x = 0$, 0.5, and 1) in Fig. 4.10 show that the boundaries of the minority band gap at E_F are dominated by the Co states. A minority band gap occurs for the complete $Co_2(Mn_xTi_{1-x})Ge$ series indicating half-metallic behavior. The Fermi energy is shifted from a position close to the conduction band edge for Co_2TiGe to a position near the valence band edge for Co_2MnGe. Hence, an experimental test of the calculated band gap can be restricted to the Co related PDOS.

The experimental spin-resolved unoccupied Co PDOS is shown in Fig. 4.11 derived from the Co L_3 edge absorption data. Note, that the Co minority PDOS is close to zero in a finite energy interval around E_F. The observation of a vanishing PDOS for $E < E_F$ is a consequence of a near coincidence of the Lorentzian function and the experimental data. Thus, the experimental data support the theoretical prediction of half-metal behavior particular for Co_2MnGe. In comparison with the LDA+U calculations a nice coincidence can be find (see Fig. 4.11 (a), (c), and (f)). Only Co_2MnGe shows a deviation in the majority states which has not been understood yet. Co-Ti d hybridization states are well reproduced in the minority states (1.8 eV above E_F). Even though, from the experimental results one can assume that the Co-Ti hybridization state should be more pronounced in the calculations. In contrast to $Co_2(Mn_xTi_{1-x})Si$ a linear shift of $E_{v,max}$ with respect to E_F can be seen.

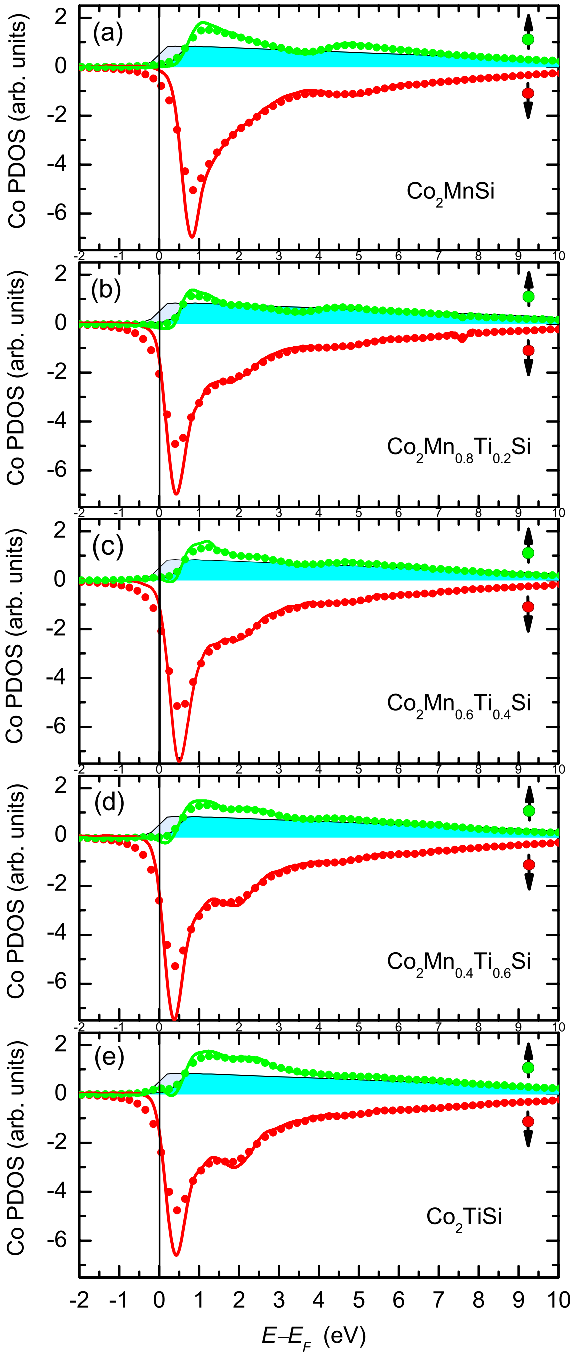

Figure 4.9: Spin-resolved Co PDOS calculated from the XAS/XMCD data measured at the Co L_3 edge for $Co_2(Mn_xTi_{1-x})Si$ samples as indicated in the Figure. Full lines show the deconvoluted data. Full filled areas indicate the function used for approximation of the itinerant band as measured (blue) and shifted by ΔE_c (light blue).

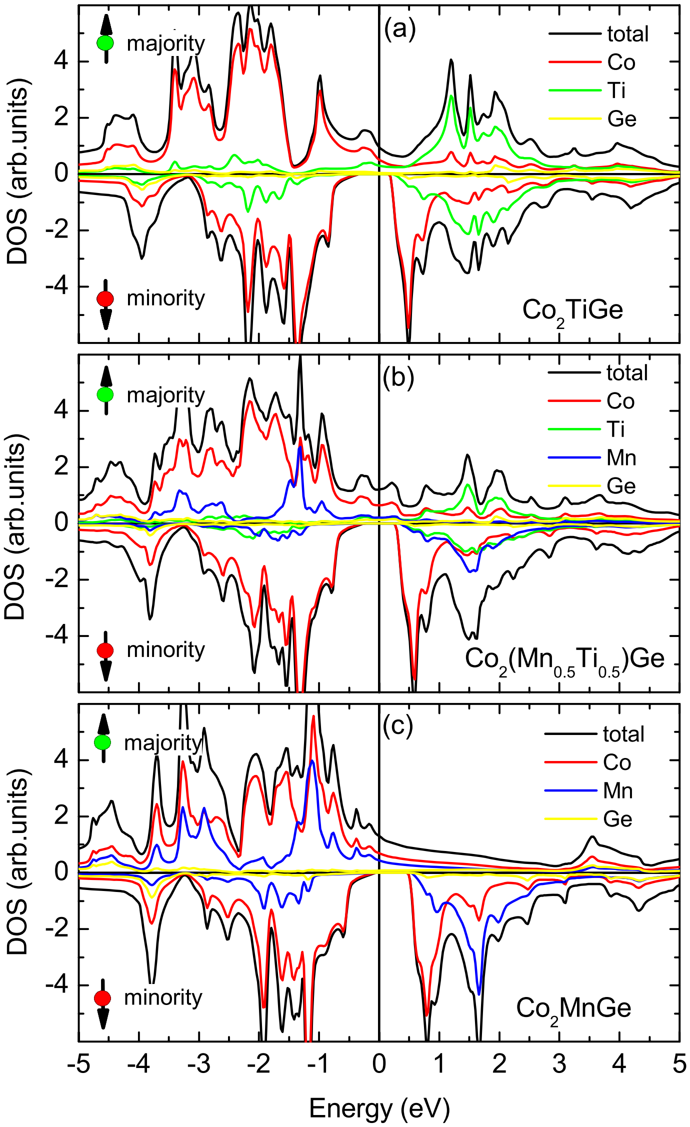

Figure 4.10: Element-specific and spin-resolved DOS for $Co_2(Mn_xTi_{1-x})Ge$ ($x = 0$, 0.5, and 1) as indicated in the Figure using *ab initio* LDA+U calculations. Calculated by G. H. Fecher (AK Felser).

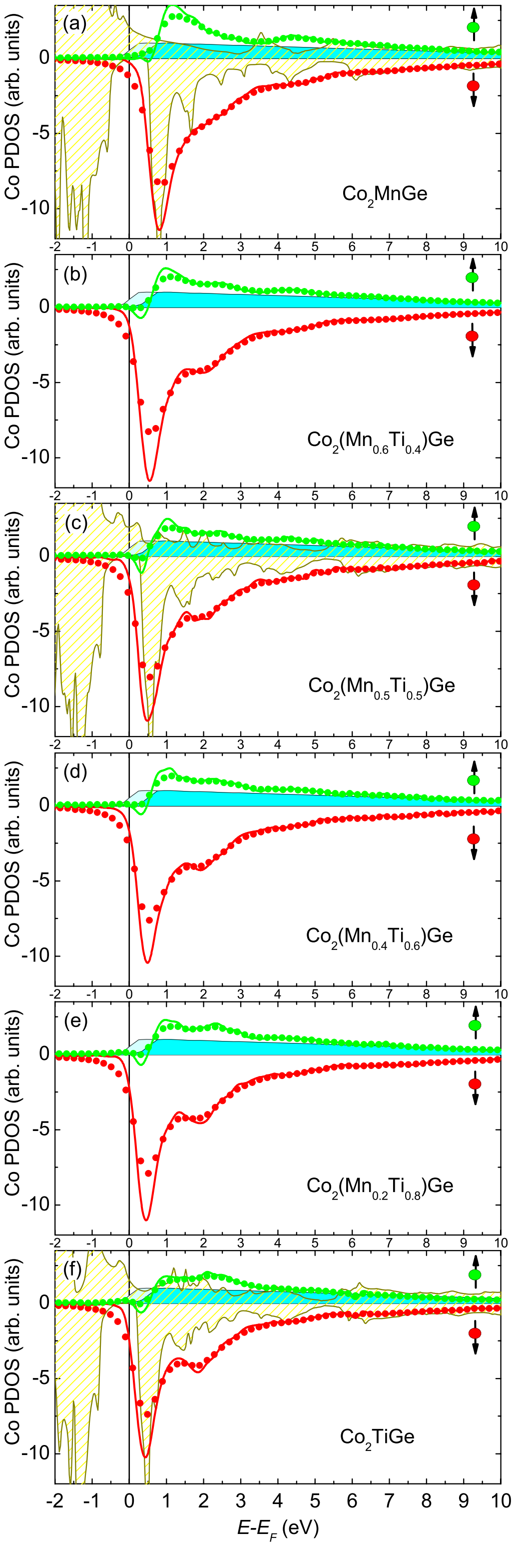

Figure 4.11: Spin-resolved Co PDOS calculated from the XAS/XMCD data (dots) measured at the Co L$_3$ edge for Co$_2$(Mn$_x$Ti$_{1-x}$)Ge samples as indicated in the figure. Full lines show the deconvoluted data. Full filled areas indicate the function used for approximation of the itinerant band as measured (blue) and shifted by ΔE_c (light blue). Data from theoretical *ab initio* calculations are shown by a yellow patterned area in (a), (c) and (f). Theory calculated by G. H. Fecher (AK Felser).

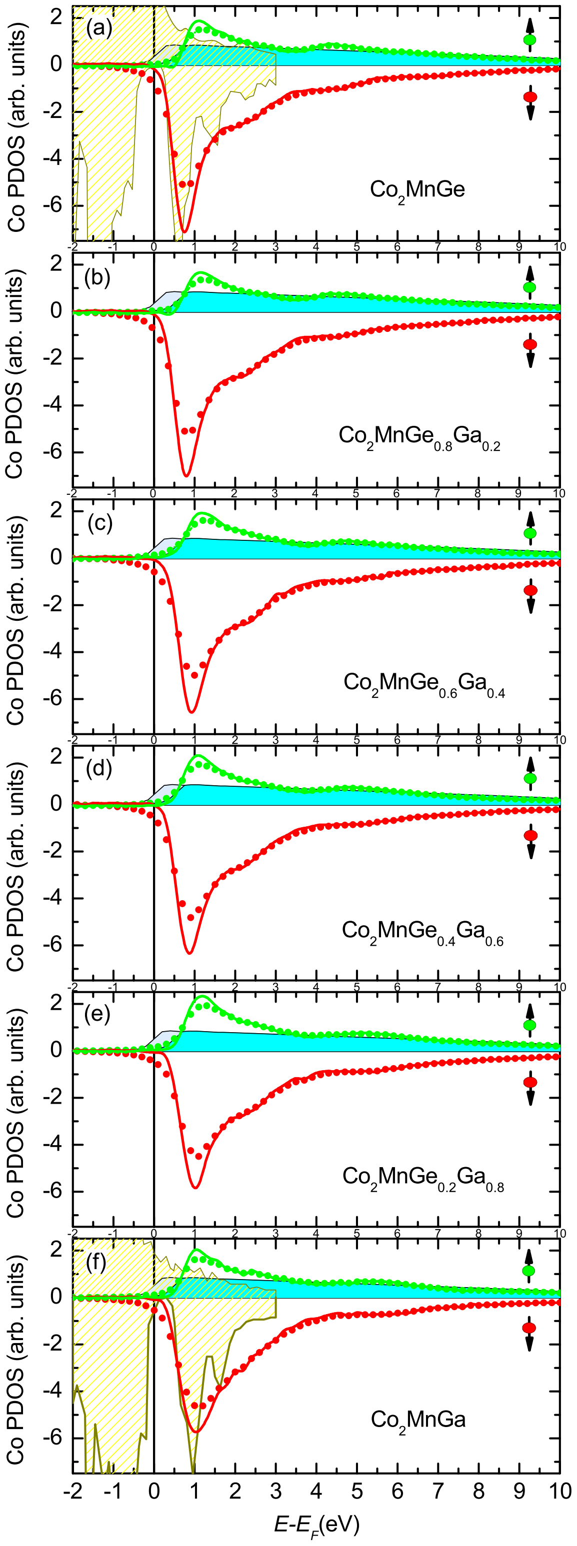

Figure 4.12: Spin-resolved Co PDOS calculated from the XAS/XMCD data (dots) measured at the Co L_3 edge for $Co_2Mn(Ga_{1-x}Ge_x)$ samples as indicated in the figure. Full lines show the deconvoluted data. Full filled areas indicate the function used for approximation of the itinerant band as measured (blue) and shifted by ΔE_c (light blue). Theoretical *ab initio* calculations from Ref. [GDP02] are shown by a yellow patterned area.

4.3.4 $Co_2Mn(Ga_{1-x}Ge_x)$

Fig. 4.12 shows the experimentally determined PDOS for $Co_2Mn(Ga_{1-x}Ge_x)$ (x = 0, 0.2, 0.4, 0.6, 0.8, and 1). Additionally included are the theoretical results (electronic structure calculations using the full-potential nonorthogonal local-orbital minimum-basis band structure scheme (FPLO) [KE98]) from Ref. [ÖSAG06] for Co_2MnGe and Co_2MnGa. The Co PDOS of Co_2MnGe (Fig. 4.12 (a)) appears similar to the corresponding spectra for Co_2MnSi as expected from theory. [ÖSAG06, GMD06] Close inspection reveals a little more pronounced Co-Mn t_{2g} related spectral weight at $E - E_F = 2.3$ eV in accordance with Refs. [ÖSAG06, GMD06].

The most prominent difference, however, is the reduced energy of the minority maximum at $E_{v,max} - E_F = 0.7$ eV compared to $E_{v,max} - E_F = 0.9$ eV for Co_2MnSi. Calculations using the same approximations for Co_2MnSi and Co_2MnGe predicted the same energy of 0.7 eV for both compounds. [GMD06] For Co_2MnGa the minority maximum is located at a larger energy $E_{v,max} - E_F = 1.0$ eV in excellent agreement with Ref. [GMD06]. The Co-Mn t_{2g} feature is weaker and the Co-Ga hybridization state appears at 5.5 eV instead of 4.5 eV for Co_2MnGe.

For the $Co_2Mn(Ga_{1-x}Ge_x)$ series, a gradual shift of the minority maximum is observed from 0.7 eV to 1.0 eV with increasing Ga concentration. The rapid decrease of the minority maximum close to E_F is compatible with the predicted half-metallic properties for the whole series. The gradual shift demonstrates the proposed concept of varying the position of E_F relative to the minority band gap.

4.4 Conclusion

Element-specific magnetic properties and electronic structures of Co_2TiZ (Z = Si, Ge, Sn, and Sb), and the substitutional series $Co_2(Mn_xTi_{1-x})Si$, $Co_2(Mn_xTi_{1-x})Ge$, and $Co_2Mn(Ga_{1-x}Ge_x)$ were investigated by XAS and XMCD. Applying the sum rule analysis the element-specific magnetic moments were determined for Co, Mn, and Ti. The Ti moment is in all samples rather small (< 0.03 μ_B/atom) and oriented antiparallel to the mean magnetization direction, indicating that Ti containing Heusler compounds are ferrimagnets. The Mn moments are comparatively large (> 3 μ_B/atom) consisting mainly of a spin moment as the orbital to spin ratio is less than 0.03. The Co moment shows values of $0.8 - 1.0$ μ_B/atom, extrapolated to 0 K in the case of Co_2TiZ. Co_2TiSb is an exception with a vanishing Ti moment and a smaller Co moment. For the parent compounds with $x = 0$ and $x = 1$ the total magnetization and the element-specific moments are in agreement with previously reported theoretical and experimental results.

The substitutional series of quaternary Heusler compounds proposed for a tuning of the band structure are expected to show a linearly increasing magnetization with increasing number of valence electrons, i.e. proportional to $N_v - 24$ and thus obeying the generalized Slater-Pauling rule. For the $Co_2(Mn_xTi_{1-x})Si$ series (except $x = 0$) slightly larger magnetization values compared to the Slater-

Pauling rule are observed. Similar observations were reported in the case of the substitutional series $Co_2Mn_{1-x}Fe_xAl$ (Ref. [JFB+09]) and attributed to partial disorder. In contrast, $Co_2(Mn_xTi_{1-x})Ge$ shows a crossing of the Slater-Pauling line at $x = 0$. For the $Co_2Mn(Ga_{1-x}Ge_x)$ series, magnetization values were measured in agreement with the Slater-Pauling rule.

The complementary series are investigated with transition metal substitution on the Y site ($Co_2(Mn_xTi_{1-x})Si$, and $Co_2(Mn_xTi_{1-x})Ge$) and main group element substitution on the Z site ($Co_2Mn(Ga_{1-x}Ge_x)$). The distribution of the magnetization on the X and Y sublattices varies with N_v in a similar way for the two complementary series. For $Co_2(Mn_xTi_{1-x})Si$ and $Co_2(Mn_xTi_{1-x})Ge$ the element-specific moments remain almost constant and the increase of the magnetization with increasing x is directly related to the increasing Mn content. Thus the Y sublattice covers the total magnetization increase. For $Co_2Mn(Ga_{1-x}Ge_x)$ an almost constant Co moment and an increasing Mn moment on the Y sublattice is found. The almost constant Co moment reflects the fact that the distribution of the Co d electrons in the majority and minority states does not change with N_v. [KFF07]

In order to maximize the number of unpaired electrons, the minority d states should be filled by 8 electrons to have a gap and the rest of the electrons fill the majority states. [Küb84] As the Co minority d states are occupied by roughly 3.5 electrons at each atom only 1 minority d electron stems from the Y atom. This explains the increasing moment on the Y site going from Ti to Mn. The increase of the Mn moment for $Co_2Mn(Ga_{1-x}Ge_x)$ cannot be explained by this general behavior of d electrons. In this case, the hybridization of electrons at the Z site causes a redistribution of majority and minority electrons when the Ga is replaced by Ge. Because Ge has a higher electro-negativity compared to Ga the bonding interaction between Co and Ge is stronger than for Co and Ga. This causes an electron transfer to de-localized states in the interstitial. In particular the t_{2g} minority states at the Y site are emptied. At the same time the majority t_{2g} states are filled resulting in a larger moment.

Although the orbital moment contributes less than 10 % to the total moment, its variation with composition is an important indication for local deviations from cubic symmetry. Large orbital moments may also be a hint to an increased magnetic crystal anisotropy and to an increased Gilbert damping. [KKN+09, LMC+09] An orbital magnetic moments is found to be low for the parent Heusler compounds and increased in the case of mixed compounds, i.e. $0 < x < 1$. For $Co_2(Mn_xTi_{1-x})Si$ the maximum orbital moment appears at $x = 0.8$ and for $Co_2Mn(Ga_{1-x}Ge_x)$ at $x = 0.6$. This observation is attributed to a local distortion from the cubic symmetry caused by a random occupation of the Y and Z site, respectively.

Considering final-state electron correlation, the spin-resolved PDOS at the Co atom can be extracted from the XMCD data. As the minority Co states are closest to the Fermi edge, the partial density of Co states is decisive for the half-metallic properties of the Co based Heusler compounds. The experimental results confirm theoretical predictions for the PDOS in the case of Co_2TiSi, Co_2TiGe and Co_2TiSn. The Fermi energy E_F is located at the minority conduction band edge. This means that these compounds are at the borderline of

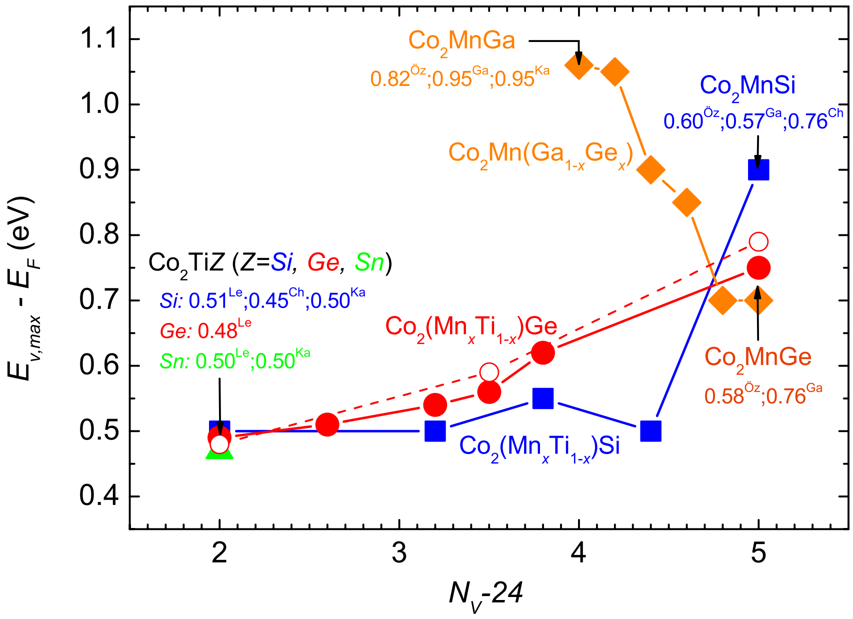

Figure 4.13: Separation of the minority PDOS maximum and the Fermi energy $E_{v,max} - E_F$ for the indicated Heusler alloys. N_v indicates the number of valence electrons per formula unit. Full symbols show the experimental results. Theoretical results are given with open symbols and as direct values from Ref. [GDP02] (Ga), [LLBS05] (Le), [ÖSAG06] (Öz), [CPR06] (Ch), and [KFF07] (Ka) as indicated.

being half-metallic. In contrast, Co_2TiSb shows a large minority PDOS at the Fermi energy like a normal metal.

The idea of tailoring the electronic structure in substitutional quaternary Heusler compounds originates from the rigid band model. Accordingly, an increasing number of valence electrons fill previously unoccupied states, thus lifting the Fermi energy with respect to the rigid band structure. Consequently, one expects that $E_{v,max} - E_F$ as defined in Fig. 2.5 decreases with increasing N_v. This is indeed observed for $Co_2Mn(Ga_{1-x}Ge_x)$ and also for $Co_2Mn_{1-x}Fe_xSi$ [KKS+09].

Replacing Ge by Ga increases the difference between the prominent maximum $E_{v,max}$ in the minority PDOS and E_F. Fig. 4.13 summarizes the results for the separation of the minority PDOS maximum and the Fermi energy $E_{v,max} - E_F$. For the series $Co_2Mn(Ga_{1-x}Ge_x)$ a gradual shift of the minority PDOS maximum is observed from 0.7 eV for $x = 1$ to 1.0 eV for $x = 0$ and also a gradual increase of the onset of the minority PDOS with decreasing x. Thus, the Co minority PDOS corroborates half-metallic ferromagnetism for the whole series. In contrast, $E_{v,max} - E_F$ increases with increasing N_v for $Co_2(Mn_xTi_{1-x})Si$, and $Co_2(Mn_xTi_{1-x})Ge$ indicating a reversed electron transfer out of the Co d majority states. Replacing Ti by Mn reduces the difference $E_{v,max} - E_F$ between the prominent maximum $E_{v,max}$ in the minority PDOS

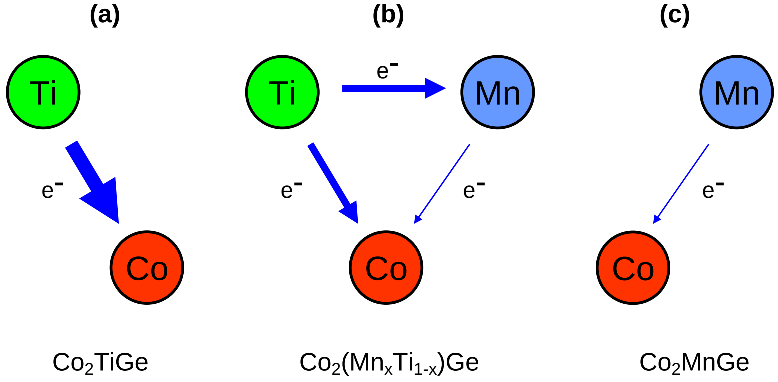

Figure 4.14: Charge transfer sketch for the (a) Co_2TiGe, (b) $Co_2(Mn_xTi_{1-x})Ge$ and Co_2MnGe compound. The arrows represent the direction and the amount of the electron transfer between the atoms.

and E_F. For $Co_2(Mn_xTi_{1-x})Ge$ a nearly linear increase of $E_{v,max} - E_F$ is observed with increasing x. However, obviously the rigid band model is too simple, as it does not explain the experimental result.

The result for $Co_2(Mn_xTi_{1-x})Ge$ can instead be explained by the charge transfer sketched in Fig. 4.14. Ti has a very small electronegativity compared to Co. This causes charge transfer from Ti to Co in Co-Ti d hybridization states (t_{2g} states) as displayed in (a) for Co_2TiGe. If Ti atoms are replaced by Mn (b) the electrons are redistributed. Mn has an electronegativity between Ti and Co. The electron transfer from Mn to Co is less pronounced. Moreover, electrons are shifted from Ti to Mn instead to the Co sites. The Mn-Ti charge transfer causes an additional loss of occupied majority Ti states at E_F and an increasing of the negative magnetic Ti moment (see also Tab. 4.3). The redistribution increases with increasing number of replaced Ti atoms. Thus the increasing electronegativity Ti-Mn-Co leads to an emptying of majority Co d states near E_F. Accordingly, E_F shifts to the left side of the minority band gap. Without Ti (c) we have only a small Mn-Co charge transfer. A similar electron transfer scheme was already considered for binary bulk alloys by Friedel [Fri62].

The experimental results for $E_{v,max} - E_F$ are in a good agreement with the *ab initio* calculations (see also Fig. 4.11). The linear increase in $E_{v,max} - E_F$ with increasing valence electron number N_v is quantitatively reproduced. This indicates that the predicted half-metallicity for this series exist in the $Co_2(Mn_xTi_{1-x})Ge$ series. $Co_2(Mn_xTi_{1-x})Si$ shows only one step from $x = 0.8$ to $x = 1$. This can be explained by the phase inhomogeneity discussed before. Co_2TiSi impurities in the quaternary $Co_2(Mn_xTi_{1-x})Si$ compound dominate the energetic position of $E_{v,max} - E_F$. Note, that due to the small density of Co states at the Fermi edge, a small charge transfer that is negligible for the magnetic moment causes a sizable shift. A second deviation from the rigid band model is revealed by the comparison of Co_2MnSi and Co_2MnGe. Although N_v is not changed different values for $E_{v,max} - E_F$ can be observed.

Theoretical *ab initio* calculations explaining qualitatively the trends in the case of $Co_2(Mn_xTi_{1-x})Z$ (Z = Si, and Ge) and $Co_2Mn(Ga_{1-x}Ge_x)$ show quantitative deviations from our results and with each other depending on the model assumptions. In addition, an exchange of the main group element with an element from the same group should have a negligible influence on the band structure according to theory. The deviation from that rule observed here may be a hint to previously neglected electron correlation effects.

4.5 Summary

Magnetic and electronic properties were experimentally determined for Co_2TiZ (Z = Si, Ge, Sn, and Sb), $Co_2(Mn_xTi_{1-x})Z$ (Z = Si, and Ge), and $Co_2Mn(Ga_{1-x}Ge_x)$ Heusler alloy series. All compounds are predicted to be ferromagnetic (ferrimagnetic) half-metallic except Co_2TiSb. Element-specific magnetic moments and the spin-resolved unoccupied density of states were investigated using XMCD. The small Ti magnetic spin moment oriented antiparallel to the spin moments of Co and Mn confirm the theoretical *ab initio* LDA+U calculations.

From XAS/XMCD spectra the spin-resolved unoccupied Co density of states is derived. The experimental spin-resolved spectra are in close agreement with *ab initio* calculations. $Co_2Mn(Ga_{1-x}Ge_x)$ shows a linear decreasing of the separation of the minority PDOS and Fermi energy $E_{v,max} - E_F$ with increasing valence number N_v explained by the rigid band model. An increasing value of $E_{v,max} - E_F$ with increasing N_v is found for $Co_2(Mn_xTi_{1-x})Ge$ ($Co_2(Mn_xTi_{1-x})Si$) which can not be explained by the rigid band model as in the case for $Co_2Mn(Ga_{1-x}Ge_x)$. This unexpected behavior can only be accounted for by a charge transfer from Ti to Co and Mn due to the small electronegativity of Ti in combination with the half-metallicity. The gradual shift demonstrates the proposed concept of varying the position of E_F relative to the minority band gap.

The results confirm the predicted possibility of tailoring the minority band gap using substitutional quaternary Heusler compounds. From the suggested charge transfer model one may conclude that $Co_2(Fe_xTi_{1-x})Z$ and $Co_2(Cr_xTi_{1-x})Z$ (Z = Si, Ge) series will behave in a similar way. Calculations for the parent compounds Co_2FeZ (Z = Si, Ge) [BWF$^+$08] and Co_2CrSi [CPR06] as well as the experimental result for Co_2FeSi [KKS$^+$09] support this idea. A detailed analysis reveals in some cases deviations from general assumptions related to a rigid band model and also from standard *ab initio* calculations using local density approximation, which are attributed to electron correlation effects. Nevertheless, the $Co_2(Mn_xTi_{1-x})Ge$, and $Co_2Mn(Ga_{1-x}Ge_x)$ quaternary Heusler alloys allow a tailoring of the Fermi energy position within the minority DOS band gap.

Chapter 5

Quaternary CoFeMnZ (Z = Al, Ga; Si, Ge) alloys with 1:1:1:1 composition

5.1 Motivation

Quaternary compounds of the type $XX'YZ$ are a new class of materials with high potential in spintronic applications. The structure is derived from the Heusler structure by occupying each of the four interpenetrating fcc sublattices of the L2_1 structure with a different element. A prominent example is the quaternary compound CoFeMnSi with a predicted half-metallic band structure. [DLF$^+$09] However, three different structure types with different degrees of spin polarization may form that cannot be distinguished by standard X-ray diffraction because of similar scattering factors of the constituting elements. Also magnetometry does not help because of the similar predicted magnetization values. [DLF$^+$09] In X-ray absorption spectroscopy element-specific magnetic moments are determined. As the element-specific moments considerably differ for different structure models, it becomes possible to identify the LiMgPdSn-Typ I (space group $F\overline{4}3m$) as the correct structure type in the case of CoFeMnSi (see Fig. 5.1). For this particular structure half-metallicity is predicted. [DLF$^+$09] In this chapter experimental and theoretical results are compared for the four compounds CoFeMnZ (Z = Al, Ga; Si, Ge). From the XAS/XMCD data the element-specific partial density of states function (PDOS) for Co, Fe, and Mn will be presented using the previously in Chap. 2.1 described data evaluation. The quaternary CoFeMnZ alloys with $1:1:1:1$ composition extend the common Heusler compounds giving an enormous potential to design physical properties.

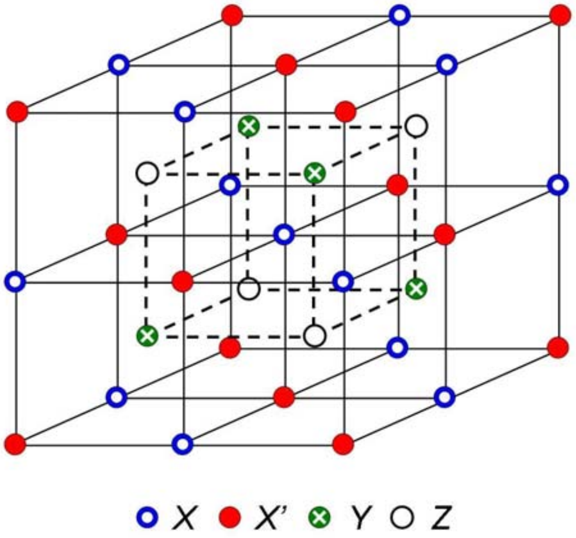

Figure 5.1: Cubic LiMgPdSn-Typ structure of the related X_2YZ L2_1-Heusler structure. Type I: Co, Fe, Mn, and Si atoms occupy the X, X', Y, and Z sublattice. Type II: Co, Mn, Fe, and Si occupy the X, X', Y, and Z sublattice. Type III: Fe, Mn, Co, and Si occupy the X, X', Y, and Z sublattice.

5.2 Computational details

The basic electronic structure calculation and the optimization of the lattice parameter were carried out using the scalar-relativistic full potential linearized augmented plane wave method (FLAPW) as provided by WIEN2K [BSM$^+$01]. The exchange-correlation functional was taken within the generalized gradient approximation (GGA) in the parametrization of Perdew-Burke-Ernzerhof (PBE) [PBE96]. 816 k-points in the irreducible wedge of the Brillouin zone of the primitive $F\overline{4}3m$ cell were used for integration. The number of plane waves was restricted by $R_{MT} \cdot k_{max} = 9$. Both, total energy (10^{-5} Ry) and charge ($10^{-2}\ e^-$) were used simultaneously as criteria for convergence.

For the disordered structures, further electronic structure calculations have been carried out using the full relativistic spin-polarized Korringa-Kohn-Rostocker method (SPRKKR) provided by Ebert *et al.* [Ebe05,Ebe99,EMP01]. This program provides the coherent potential approximation (CPA) for calculating the properties of alloy systems with random distribution of the atoms. The SPRKKR calculations have been performed using the PBE generalized gradient approximation. [PBE96] The CPA tolerance was set to 10^{-4} and the energy convergence criterion to 10^{-5}. f-states were included in the basis of all atoms. 832 irreducible k-points based on a $22 \times 22 \times 22$ mesh have been used for integration. The density of states is calculated for the double number of k-points from the Greens function by adding a small imaginary part of 0.005 Ry to the energy. For smaller values, the band gaps may become better visible, however, at the same time the DOS becomes much more noisy. The calculations have

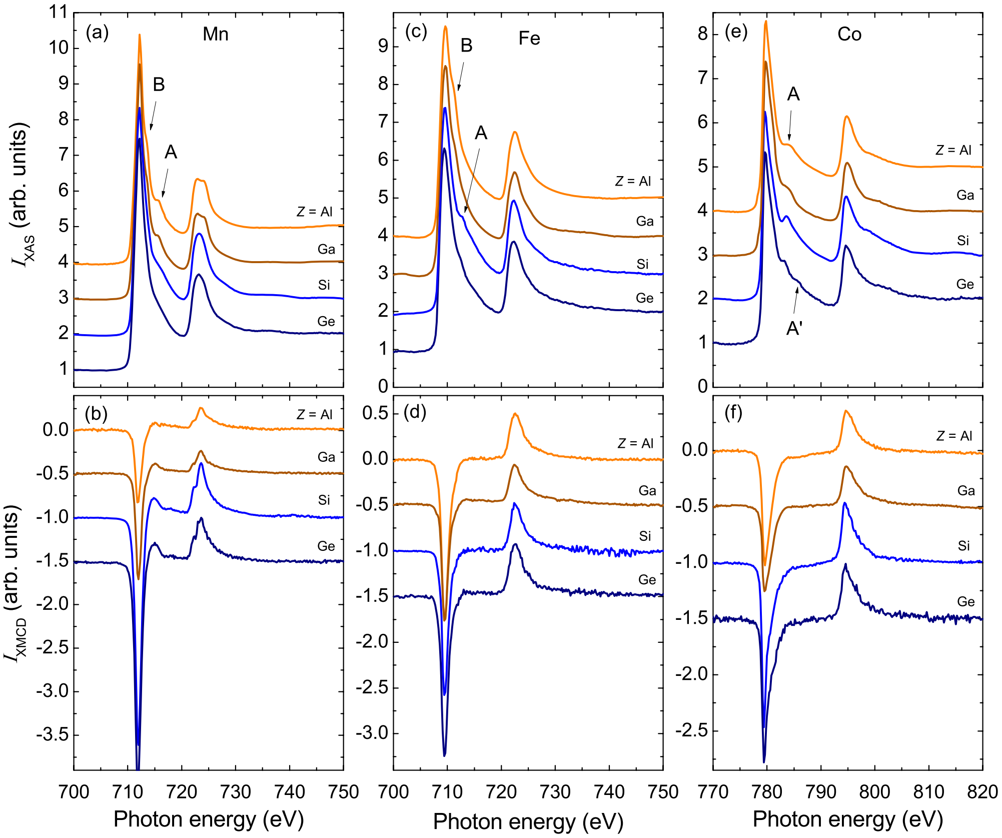

Figure 5.2: (a), (c), (e) X-ray absorption spectra I_{XAS} for CoFeMnZ (Z = Al, Ga; Si, Ge) measured at the Mn, Fe, and Co $L_{3,2}$ edge averaged from total electron yield intensities I^+ and I^- for magnetization direction parallel and antiparallel to the X-ray polarization. (b), (d), (f) corresponding XMCD spectra $I_{\text{XMCD}} = I^+ - I^-$ on the same scale.

been done by G. H. Fecher (AK Felser), hence, more description and electronic band structure calculations can be found in Ref. [AOF+11].

5.3 Element-specific magnetic properties

The XAS/XMCD measurements were performed at room temperature resulting close to the ground state because the Curie temperature is comparatively large ($\sim$ 900 K). The results for the Mn, Fe and Co measured at the $L_{3,2}$ edge are summarized in Fig. 5.2. The XAS spectra were normalized at the post-edge value after subtracting a constant background from the raw data. The shape of the spectra appear pairwise similar for CoFeMnZ (Z = Al, Ga) and for CoFeMnZ (Z = Si, Ge). This is not surprising because the crystal structures are similar and the compounds with Al (Ga) and Si (Ge) are isoelectronic. Similar changes occur at the L_3 edge and L_2 edge.

The Co XAS spectra in Fig. 5.2 (e) show a satellite peak A ($\sim$ 4 eV above

L_3 maximum) for all samples, which is indicative for a *sd* band hybridization state similar to the related Co-based highly ordered Heusler compounds with a $L2_1$ crystal structure. [TKvdL$^+$06, EFV$^+$03] For Z = Ge an additional satellite peak A' appears which was observed for the Co_2MnGe Heusler alloy, too (cf. Chap. 4.2.4). A related satellite peak A is also visible for the Fe spectra for Z = Si, Ge (Fig. 5.2 (c)). The Fe peak A can be attributed to a *sd* band hybridization of Fe and the main group element Z = Si, Ge. As a consequence of the weaker hybridization between Co/Fe and the main group element Z = Al, Ga the satellite peak A is broader for Co and absent in the Fe XAS spectra. B2 disorder (random occupation of the Mn and Z sublattice with these two elements) may lead to the loss of the hybridization peak.

CoFeMnZ (Z = Al, Ga) comprise two peaks indicated by A and B in the Mn spectra (Fig. 5.2 (a)) and a peak B in the Fe spectra (Fig. 5.2 (c)). An explanation for peak A and peak B could be multiplet effects stemming from oxidation of Mn and Fe. However, an oxidation is unlikely as the sample was kept in UHV conditions after cleavage. No bulk contrast of oxygen was found in the EDX measurement. Instead, the Mn satellite peaks are attributed to a strong localization of Mn states and a corresponding by large contribution from multiplet effects caused by the configurational interaction of the core hole and the excited electron in the final state. [dG05] A similar effect has been observed in the case of Co_2MnZ (Z = Si, Al)(see Chap. 4 and Ref. [TKvdL$^+$08]).

The largest change with composition in the XMCD spectra occurs for Mn in Fig. 5.2 (b). CoFeMnZ has in the case of Z = Si, Ge larger asymmetries than that for Z = Al, Ga at the $L_{3,2}$ edge and a considerably more pronounced positive shoulder at 715 eV. The Fe and Co XMCD spectra in Fig. 5.2 (d) and (f) show no significant changes with replacing the main group element Z. Only the maxima at the $L_{3,2}$ edge appear sharper for Z = Si, Ge.

The variation of Z in CoFeMnZ has no large impact on the Co and Fe magnetic moments (see Tab. 5.1). In contrast, the increase in the valence electron number leads to a strong increase of the Mn magnetic moment. The replacing of the main group element Z = Al, Ga by the main group element Z = Si, Ge leads to an increase of the Mn magnetic moment and consequently an increase of the total magnetic moment by 1 μ_B/f.u. (see Fig. 5.3). The total magnetic moments resulting from XMCD are in good agreement with the measured SQUID results and the theoretical values.

In the case of Z = Si, Ge predictions from first principle GGA calculations assuming a perfect type I structure are in agreement with the experimentally determined element-specific magnetic moments. In contrast, these calculations predict an antiferromagnetically aligned Fe moment in the case of Z = Al, Ga which is not observed in the experiment. This indicates significant contributions from other structure types. Only in the case of Z = Si the structure analysis using XRD gives a closer hint on a prevailing type I structure with some contribution from type II. In order to quantify the disorder contribution, a detailed analysis of element-specific moments is performed for the case of CoFeMnSi.

Tab. 5.2 compares the element-specific moments for CoFeMnSi with theoretical values from Ref. [DLF$^+$09] for three different structure models. The structure models reflect a different occupation of the four sublattices in the

	μ	Co	Fe	Mn
Z = Al	μ_{spin}	0.77 ± 0.02	0.91 ± 0.02	0.96 ± 0.02
	μ_{orb}	0.07 ± 0.01	0.07 ± 0.01	0.06 ± 0.01
	$\mu_{\text{spin}}^{\text{GGA}}$	0.81	−0.13	2.44
Z = Ga	μ_{spin}	0.85 ± 0.02	0.72 ± 0.02	1.05 ± 0.02
	μ_{orb}	0.03 ± 0.01	0.02 ± 0.01	0.09 ± 0.01
	$\mu_{\text{spin}}^{\text{GGA}}$	0.77	−0.15	2.60
Z = Si	μ_{spin}	0.88 ± 0.02	0.72 ± 0.02	2.22 ± 0.02
	μ_{orb}	0.06 ± 0.01	0.03 ± 0.01	0.09 ± 0.01
	$\mu_{\text{spin}}^{\text{GGA}}$	0.88	0.52	2.70
Z = Ge	μ_{spin}	0.82 ± 0.02	0.82 ± 0.02	1.95 ± 0.02
	μ_{orb}	0.06 ± 0.01	0.02 ± 0.01	0.04 ± 0.01
	$\mu_{\text{spin}}^{\text{GGA}}$	0.86	0.50	2.71

Table 5.1: Element-specific magnetic spin moment μ_{spin} (μ_B per atom) and orbital moment μ_{orb} (μ_B per atom) for CoFeMnZ (Z = Al, Ga; Si, Ge) alloys as calculated from the sum rules and from first principle GGA calculations. For the number of unoccupied $3d$ states the values $N_h(\text{Fe}) = 3.4$, $N_h(\text{Mn}) = 4.5$, and $N_h(\text{Co}) = 2.5$ and for Mn a jj-mixing correction factor $c_{jj} = 1.5$ were assumed. Theoretical values a calculated by G. H. Fecher (AK Felser).

	μ_{Co}	μ_{Fe}	μ_{Mn}	μ_{Si}	μ_{tot}
Type I	0.878	0.576	2.649	−0.067	4.006
TypeII	0.931	2.517	0.591	−0.010	3.959
Type III	1.786	1.804	1.898	−0.055	5.332
XMCD	0.88	0.72	2.22		3.82

Table 5.2: Theoretical magnetic spin moment μ_{spin} (μ_B per atom) and total magnetic moment μ_{spin} (μ_B per formula unit) for CoFeMnSi in the three nonequivalent superstructures from Ref. [DLF$^+$09] as labeled. Experimental magnetic moments measured by XMCD are given for comparison.

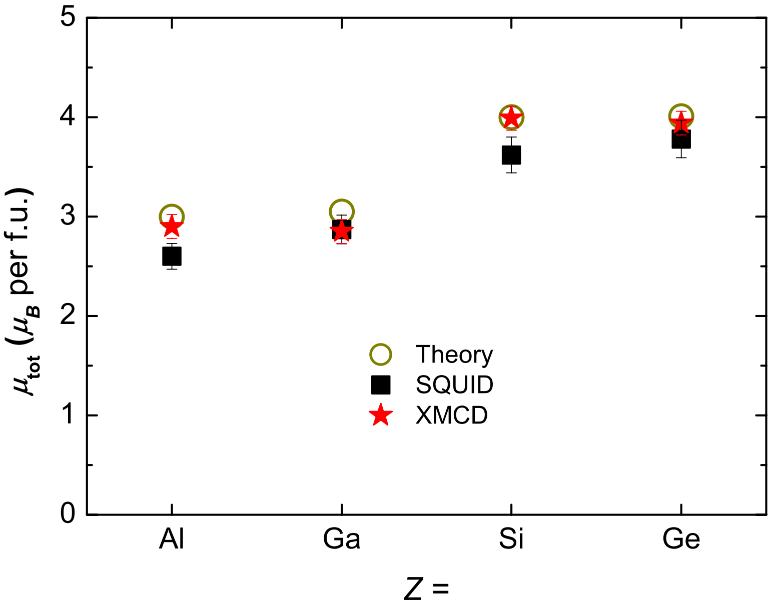

Figure 5.3: Total magnetic moments $\mu_{\rm tot}$ for CoFeMnZ (Z = Al, Ga; Si, Ge) measured at 300 K with SQUID (measured by V. Alijani (AK Felser)) and XMCD. Theoretical magnetic moments are given for comparison.

LiMgPdSn-Typ structure with the four elements of the quaternary compound (see Fig. 5.1). For the type I structure the Fermi energy lies in an energy gap of 0.75 eV in the spin-down states (shown in Fig. 5.5). The electronic structure of the type II structure is similar to that of type I, but the Fermi energy lies in a pseudogap. Therefore, the CoFeMnSi compound with type I or type II structure is a half-metallic or nearly half-metallic ferromagnet. The type III compound is a metallic ferromagnet with a large DOS value at E_F in the spin-down channel.

The sublattice occupation has a large effect on the size of the magnetic moments in particular on the ratio of the Mn and Fe moment. The best agreement of the experimental and theoretical results can be found for the type I structure in Tab. 5.2. Structure type III can be excluded by comparing the theoretical and experimental Co magnetic moment and the total magnetic moment. The most indicative number for distinguishing between the type I and II structure models which result in similar average magnetization values is the ratio of Mn and Fe moments with predicted values of 4.60 (0.23) for model I (II). The experimental value of 3.08 is close to the value of model I. In the following it is assumed that disorder involves exclusively structure type I and II with the Mn and Fe moments as given in Tab. 5.2. With the volume fraction r for structure type I one obtains average Mn (Fe) moments

$$\bar{\mu}_i = r \cdot \mu_i^{\rm I} + (1-r) \cdot \mu_i^{\rm II} \ , \quad i = {\rm Mn, Fe}. \tag{5.1}$$

The ratio of the averaged Mn and Fe magnetic moments

$$\frac{\bar{\mu}_{\rm Mn}}{\bar{\mu}_{\rm Fe}} = \frac{r \cdot \mu_{\rm Mn}^{\rm I} + (1-r) \cdot \mu_{\rm Mn}^{\rm II}}{r \cdot \mu_{\rm Fe}^{\rm I} + (1-r) \cdot \mu_{\rm Mn}^{\rm II}} \ , \tag{5.2}$$

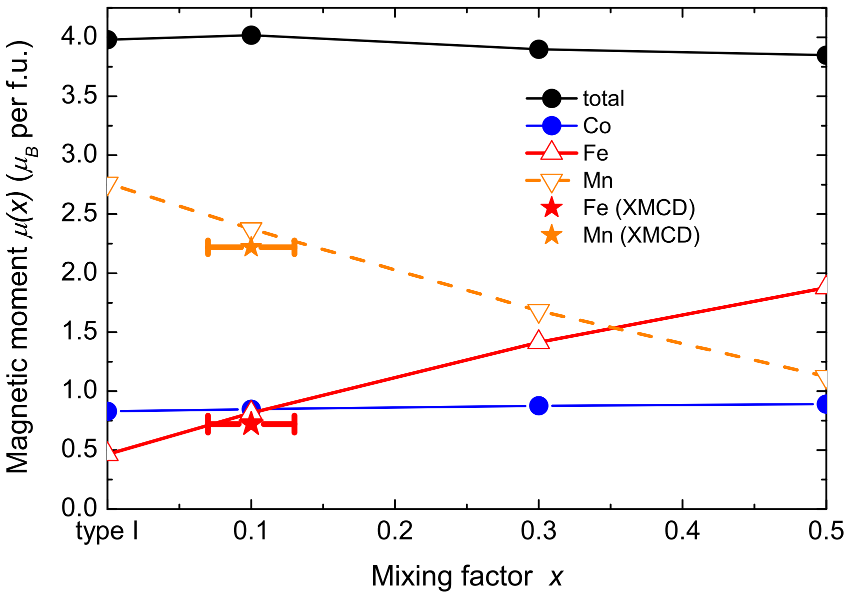

Figure 5.4: Theoretical calculated magnetic moments for CoFeMnSi depending on the contribution of the type II structure (x) compared with the XMCD results. Theoretical values are calculated by G. H. Fecher (AK Felser).

must equal the experimental value of 3.08. From the equation we obtain a volume fraction $r = 0.89$, indicating a disorder on the order of 11%. An alternative approach is a direct comparison of theoretical calculated moments for various types of disorder with the experimental data. The disorder cannot be varied continuously but a large unit cell can be used. [JFB$^+$09] The result is shown in Fig. 5.4. The total magnetization is nearly independent on the contribution of the type II structure x. The Fe moment increases and the Mn moment decreases with increasing x. A comparison with the experimental data indicates a contribution of $x = 0.1$ in good agreement with the analytical discussion above.

5.4 Spin-resolved unoccupied density of states

The self-consistent electronic structure calculation of the partial density of states (PDOS) for the type I CoFeMnSi structure in Fig. 5.5 show that the lower boundary of the minority band gap near E_F is given by the Co and Fe states. Therefore, an experimental determination of the element-specific Co, Fe (and Mn) density of states is essential. CoFeMnZ (Z = Al, Ga; Si, Ge) compounds exhibit a calculated electronic structure which is typical for a fully spin-polarized half-metallic ferromagnetic Heusler compound (see also Fig. 5.5).

Experimental data for the spin-resolved unoccupied Mn, Fe, and Co PDOS are shown in Figs. 5.6, 5.7, and 5.8 as derived from the corresponding L_3 edge XAS/XMCD data. For the calculation the spin-resolved unoccupied PDOS $D^{\uparrow(\downarrow)}(1 - f_F)$ (Eq. 2.10) was used. This procedure has been applied before only for the case of Co in Co_2YZ Heusler alloys (see Chap. 4). In this case an

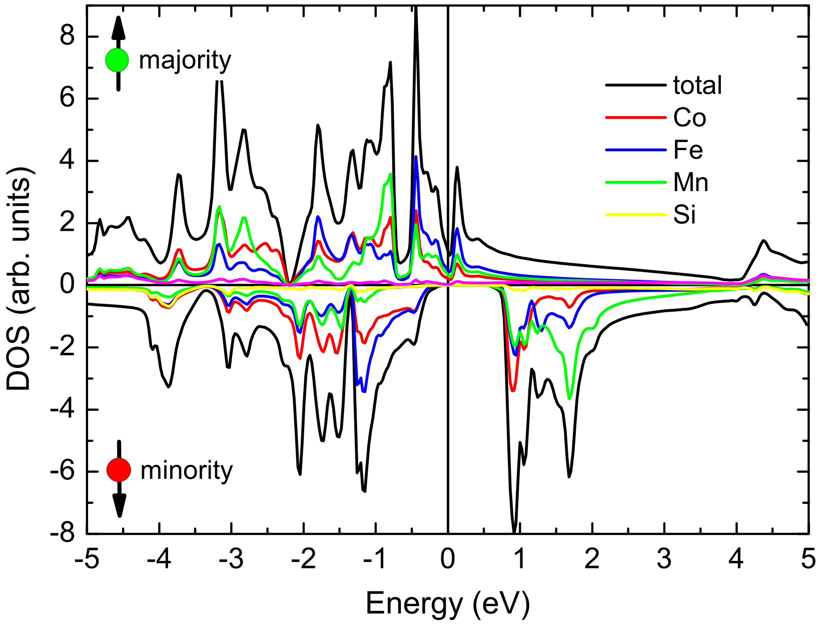

Figure 5.5: Spin-resolved PDOS for CoFeMnSi using *ab initio* calculations according to Ref. [DLF$^+$09]. Theory calculated by G. H. Fecher (AK Felser).

electron correlation effect causes a shift of the majority PDOS of $\Delta E_c = 0.5$ eV with respect to the minority states for the Co data. The position of the Fermi energy was derived from the initial increase in the majority states considering the energy shift of ΔE_c.

For Mn and Fe the value for ΔE_c is set to zero. The Mn and Fe majority PDOS comprises localized states at E_F both for majority and minority states in contrast to the Co PDOS. Because of the life-time broadening of the XAS spectra, the experimental spectra are deconvoluted with a Lorentzian function with a width of $\Gamma = 0.35$ eV.

For all three Co, Fe, and Mn elements in CoFeMnZ (Z = Si, Ge) the comparison of theoretical and experimental results for the minority PDOS reveals a fair agreement considering life-time broadening. In particular, the PDOS minority maxima agree well. This observation confirms the assumption of $\Delta E_c = 0.5$ eV in the case of Co and $\Delta E_c = 0$ eV in the case of Fe and Mn. The same values of ΔE_c were assumed in the case of Z = Al, Ga. In the case of Z = Al, Ga the experimental minority PDOS for Fe and Co are shifted to somewhat larger energies compared to theoretical values. This might be attributed to a residual B2 disorder in these compounds, as also observed by X-ray diffraction.

As expected from the XAS spectra, the unoccupied PDOS shown in Figs. 5.6, 5.7, and 5.8 of the isoelectronic compounds Z = Al, Ga and Z = Si, Ge behave pairwise similarly. The increase in the Co minority PDOS shows a steeper slope than the Fe and Mn minority PDOS. The smaller slope in the Mn PDOS fits well with theoretical GGA calculations showing a much broader feature of 1.5 eV width for Mn compared to 0.2 eV in the case of Co.

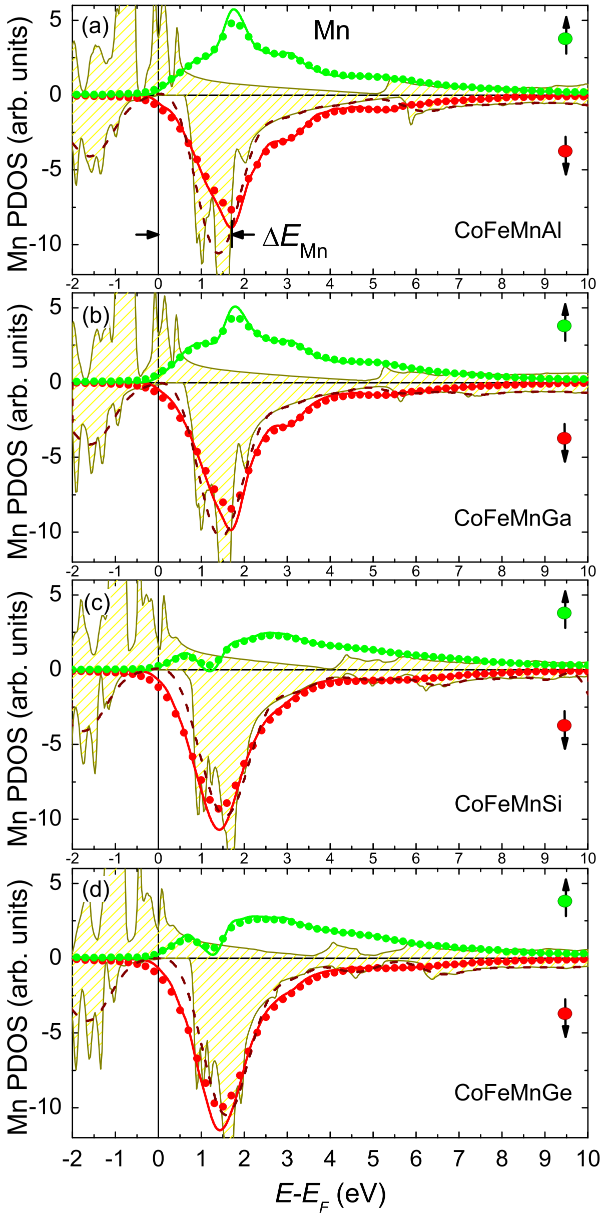

Figure 5.6: Spin-resolved Mn PDOS calculated from the XAS/XMCD data (dots) measured at the Mn L_3 edge for CoFeMnZ (Z = Al, Ga; Si, Ge) samples as indicated in the figure. Full lines show the deconvoluted data. Data from theoretical *ab initio* calculations are indicated by a yellow patterned area. Theoretical data are calculated by G. H. Fecher (AK Felser). The dashed lines show the smoothed theoretical data of the minority PDOS.

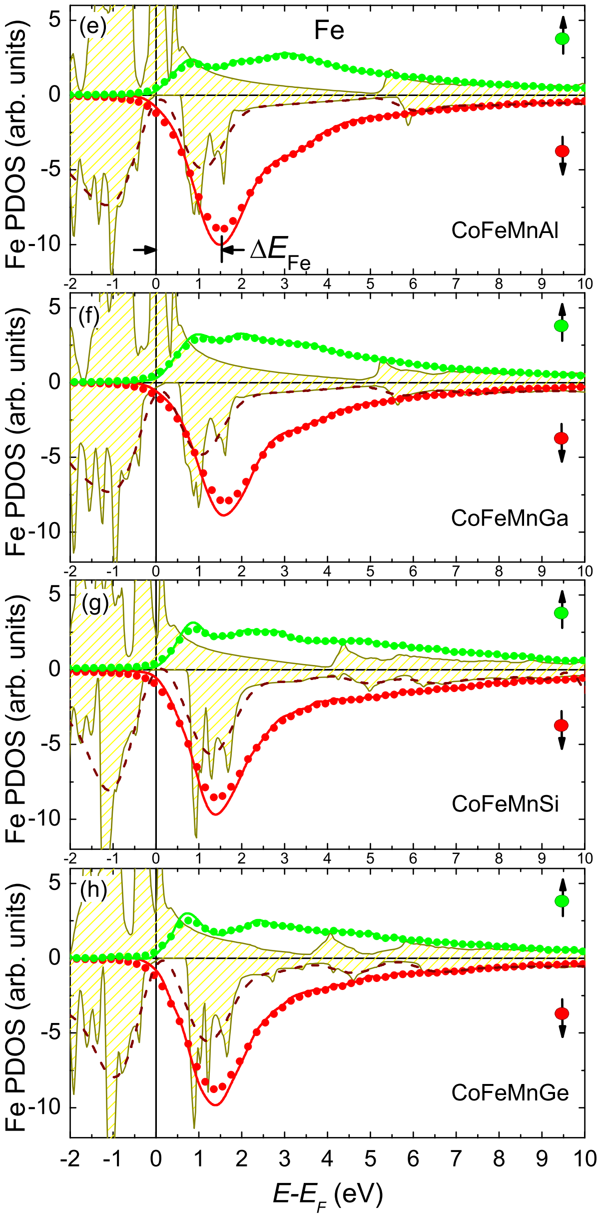

Figure 5.7: Spin-resolved Fe PDOS calculated from the XAS/XMCD data (dots) measured at the Fe L_3 edge for CoFeMnZ (Z = Al, Ga; Si, Ge) samples as indicated in the figure. Full lines show the deconvoluted data. Data from theoretical *ab initio* calculations are indicated by a yellow patterned area. Theoretical data are calculated by G. H. Fecher (AK Felser). The dashed lines show the smoothed theoretical data of the minority PDOS.

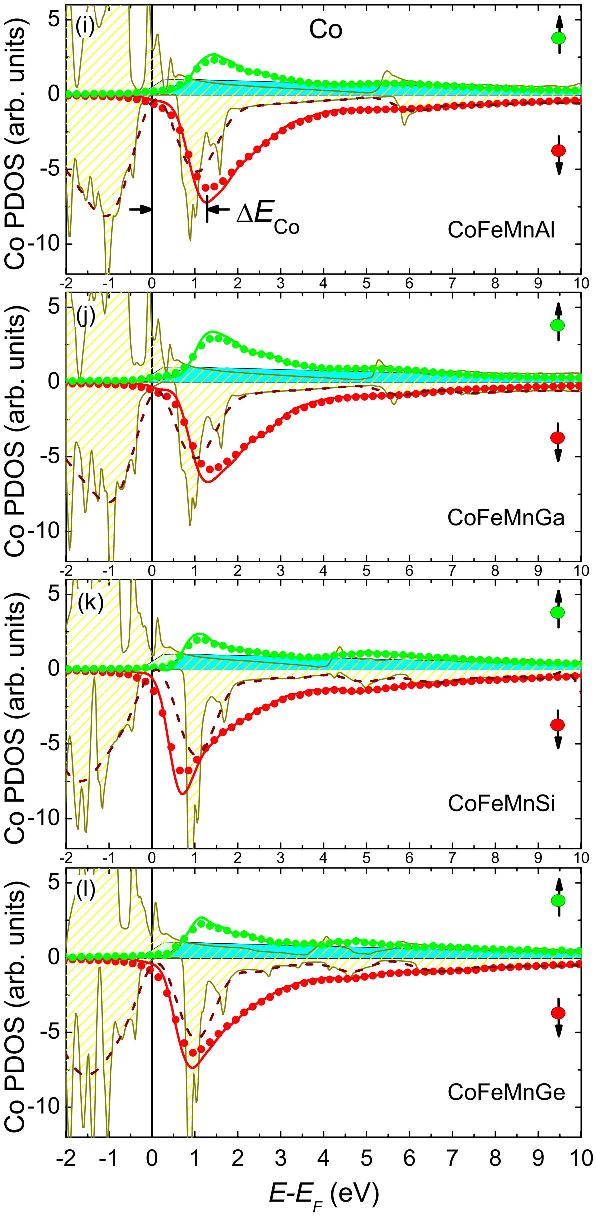

Figure 5.8: Spin-resolved Co PDOS calculated from the XAS/XMCD data (dots) measured at the Co L_3 edge for CoFeMnZ (Z = Al, Ga; Si, Ge) samples as indicated in the figure. Full lines show the deconvoluted data. Data from theoretical *ab initio* calculations are indicated by a yellow patterned area. Theoretical data are calculated by G. H. Fecher (AK Felser). The dashed lines show the smoothed theoretical data of the minority PDOS. Full filled areas indicate the function used for approximation of the Co itinerant band as measured (blue) and shifted by ΔE_c (light blue).

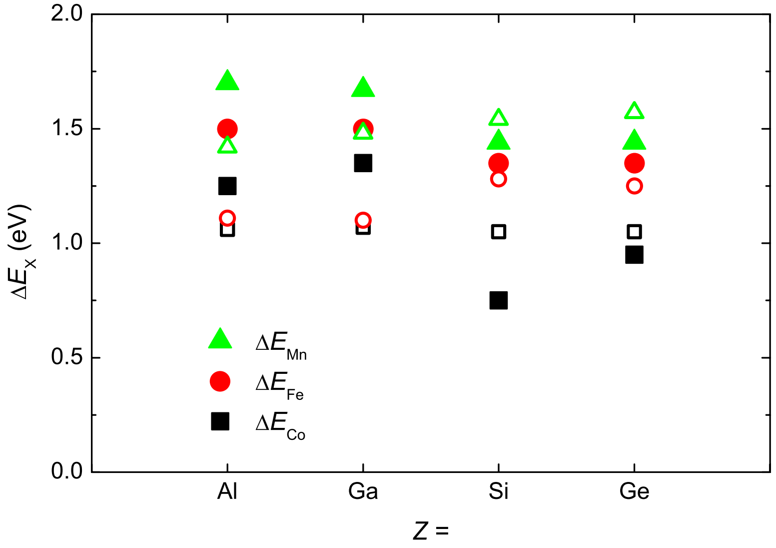

Figure 5.9: Element-specific values for ΔE_X (X = Mn, Fe, and Co) as defined in Figs. 5.6, 5.7, and 5.8 for CoFeMnZ (Z = Al, Ga; Si, Ge). Theoretical values are denoted for comparison with open symbols. Theoretical values are calculated by G. H. Fecher (AK Felser).

The experimental majority Co PDOS shows a flat line, except for a small peak near 1 eV above E_F, expected from theoretical calculations. In contrast, the Fe and even more the Mn majority PDOS reveal a rich structure that has no correspondence in the theoretical majority PDOS. A prominent difference between the Co, Mn, and Fe PDOS is the stronger localization of electronic states in the latter case (see below) according to calculations. These localized states lead to multiplet effects splitting a single transition into a number of absorption peaks. For the case of Mn in Co_2MnSi and Rh_2MnSi this has been explicitly shown by comparison to an atomic model. [KKE$^+$09,dG05] Therefore, one can attribute the rich structure of the majority Fe and Mn PDOS to the occurrence of these multiplet effects. The ground-state GGA calculations do not consider these final-state effects, and hence it is no surprise that theory and experiment do not agree in this case. Although not obvious, these multiplet effects might also alter the minority PDOS and an interpretation of the Mn and Fe PDOS has to be done with care.

The difference between the energy position of the minority maximum and the Fermi energy $\Delta E_X = E^X_{v,max} - E_F$ (X = Mn, Fe, and Co) depends on Z as summarized in Fig. 5.9. Assuming a rigid band model the replacing of Z = Al, Ga by Z = Si, Ge shifts the Fermi energy from the minority band gap in the Co, Fe, and Mn PDOS spectra toward the conduction band edge. The additional valence electron fills majority states at the Fermi energy. According to the rigid band model, one would expect that the shift of the Fermi energy increases with decreasing majority PDOS at E_F. The Co PDOS shows the smallest value at E_F, and the observed change of ΔE_X from main group element III (Z = Al, Ga) to group IV (Z = Si, Ge) is largest for Co. Therefore, our experimental observation is in agreement with the rigid band model. In contrast, the theoretical calculations show no significant changes of ΔE_X with changing Z. The GGA calculations show a large increase in minority states at 1 eV above E_F for all elements. In the case of Co the minority maximum increases with respect to the second maximum at 1.7 eV for replacing Al by Si. Considering life-time broadening this feature leads to a shift. The theoretical PDOS is smoothened for considering dynamic correlation effects (see dashed line in Figs. 5.6, 5.7, and 5.8). ΔE_X resulting from this procedure fits considerably better to the experimental values and is summarized in Fig. 5.9.

Pronounced discrepancies still remain for the case of Z = Al, Ga with a systematically larger experimental value of ΔE_{X} compared to theory. A possible reason is the occurrence of B2 disorder in this case, while theory considers a perfectly ordered atomic structure. However, a previous study on epitaxial films revealed a decrease of ΔE_{Co} instead of an increase with an increase in disorder for $\mathrm{Co_2Fe(Al_{1-x}Si_x)}$. [KKS$^+$09]

5.5 Summary

Element-specific magnetic moments and the element-specific spin-resolved DOS were presented of the quaternary CoFeMnZ (Z = Al, Ga; Si, Ge) alloy using XMCD. A comparison of calculated moments with the evaluated Co, Fe, and Mn magnetic moments clearly allows one to distinguish between various structure models confirming the proposed LiMgPdSn-Typ structure in the case of Z = Si with predicted half-metallicity from Refs. [DLF$^+$09, AOF$^+$11]. Exchange of the main group element from group III (Z = Al, Ga) by those from group IV (Z = Si, Ge) causes an increase in the Mn magnetic moment of 1 μ_B/f.u.. From XAS/XMCD the element-specific spin-resolved unoccupied PDOS was derived for Co, Fe, and Mn, which can be directly compared to *ab initio* GGA calculations. A shift of the spectral weight with replacing the Z = Al, Ga main group element by Z = Si, Ge explained by the rigid band model was found similar to the case of $\mathrm{Co_2Mn(Ga_{1-x}Ge_x)}$ (Chap. 4). The largest shift of the Fermi energy with respect to the half-metallic band gap is observed for the Co PDOS due to the small density of states in the majority band. The good agreement between theoretical and experimental results considering final state effects confirms that the quaternary LiMgPdSn-Typ ferromagnets provide a class of promising materials for spintronic devices with high spin polarization. Therefore, with an improved sample preparation a design of a half-metallic ferromagnet with CoFeMnZ (Z = Si and, especially, Z = Ge) seems to be possible.

Chapter 6

Temperature dependent properties of Mn_2VAl and Co_2FeAl thin films

6.1 Motivation

Spintronic devices consisting of tunneling magnetoresistors (TMR) that exploit the high spin polarization of half-metallic ferromagnetic Heusler alloys have been fabricated [KTHR04, SHO+06, IHiM+08, WSS+08, SSW+09, TIMS09] confirming the concept of half-metallic ferromagnets at low temperatures. However, the strong temperature dependence of the effective spin polarization is not fully understood, yet. The temperature dependence of the electronic states in half-metals might contribute to the strong decrease in the spin polarization and its experimental investigation is highly interesting. In a single-particle model changes in the electronic structure are only expected in the vicinity of the Fermi energy due to thermally excited occupation of previously unoccupied states which is in agreement with a recent high energy photoemission study for a half-metallic Co_2MnSi/MgO interface. [MKM+09] Instead, a model beyond the single-particle picture of the local density approximation considering finite-temperature many-body effects [CSA+08, CAKL09] results in a considerable temperature dependence of the density of states.

Mn_2VAl, and Co_2FeAl are predicted to be half-metallic comprising a band gap in the majority spin band [GÖSA07] and in the minority spin band [FKW+05], respectively. The half-metallicity of Mn_2VAl is predicted to be rather robust against a small degree of local disorder and an intermixing between V and Al atoms should still results in an almost half-metallic behavior. [GÖSA07] Recently, an advanced local density approximation plus dynamical mean field (LDA+DMFT) approach [CAKL09] predicted the occurrence of additional states in the majority band gap caused by many-body effects. Indeed, at present there is no experimental proof that Mn_2VAl is a half-metallic ferromagnet. Reports on half-metallic ferromagagnetic properties of Co_2FeAl are controversial. [WFK+06] Using LDA calculations Ref. [MNS04] reported a spin polarization of just 30 % in both disordered B2 and ordered $L2_1$ structures. Using a similar calculation scheme Ref. [GDP02] reported a reduction of magnetization from an integer value (in μ_B per formula unit), indicating that Co$_2$FeAl is not a half-metal. Magnetic tunneling junctions with Co$_2$FeAl electrodes showed large TMR values of up to 330 % at room temperature and even 700 % at 10 K, indicating a high effective spin polarization. [WSS$^+$09]

In this chapter, the temperature dependence of XAS/XMCD spectra and the spin-resolved DOS will be discussed for Co$_2$FeAl, and Mn$_2$VAl Heusler alloys. It will be shown that the temperature dependence cannot be explained by standard single particle models.

Spin-resolved photoemission [WPK$^+$05,SJK$^+$06] appearance potential spectroscopy, [KRBD05] and scanning tunneling spectroscopy can directly probe the spin polarization at a half-metal surface. However, these methods have no access to the crucial buried interfaces in spintronic devices. In contrast, XAS/XMCD provides an element-specific information of near-surface and bulk properties as discussed in Chap. 2.1.

6.2 Element-specific magnetic properties

6.2.1 Mn$_2$VAl

Fig. 6.1 shows the experimental results for the Mn$_2$VAl films at the V, and Mn L$_{3,2}$ absorption edges. A temperature dependent change of XAS/XMCD spectra can not be directly recognized. XAS absorption spectra (Fig. 6.1 (a), and (c)) show features similar to those observed in other metallic compounds. [SWB04] Surface and bulk sensitive measurements are similar to each other and no traces of oxide-induced multiplet features are visible as in the case of Ref. [KKN$^+$09]. This is an evidence that the Mn derived states have an itinerant character for Heusler compounds (X_2YZ) with Mn at the X position.

Mn, and V magnetic moments are antiparallel oriented to each other showing a positive slope in V XMCD spectra (Fig. 6.1 (b)), and a negative slope in Mn XMCD spectra (Fig. 6.1 (d)) at first. Therefore, Mn$_2$VAl is a ferrimagnetic Heusler alloy. Comparing the TEY and TM XMCD data, one can see a large variance of the spectra explained by the information depth. The TEY data provides an information at the buried interface (information depth of 2.5 nm) and the TM data through the whole film thickness. The TEY XMCD spectra with maxima being nearly half as large as the TM XMCD spectra indicate a strong decrease of the magnetic moment at the surface.

The origin of the reduced interface magnetization is unclear. One might speculate that it is caused by a reduced atomic order at the Heusler/Al interface. Films deposited at room temperature without annealing do show a strongly reduced atomic and magnetic order in the bulk of the films. This fact gives a hint that the order and magnetism is correlated. Certainly, one also expects, that half-metallicity is destroyed by disorder. Therefore, the interface region is expected to be metallic instead of half-metallic.

Using the sum rule analysis the magnetic moments for Mn$_2$VAl were calculated from the XMCD data and summarized in Tab. 6.1. The largest total magnetic moment μ_{XMCD} is found for the transmission measurement at low

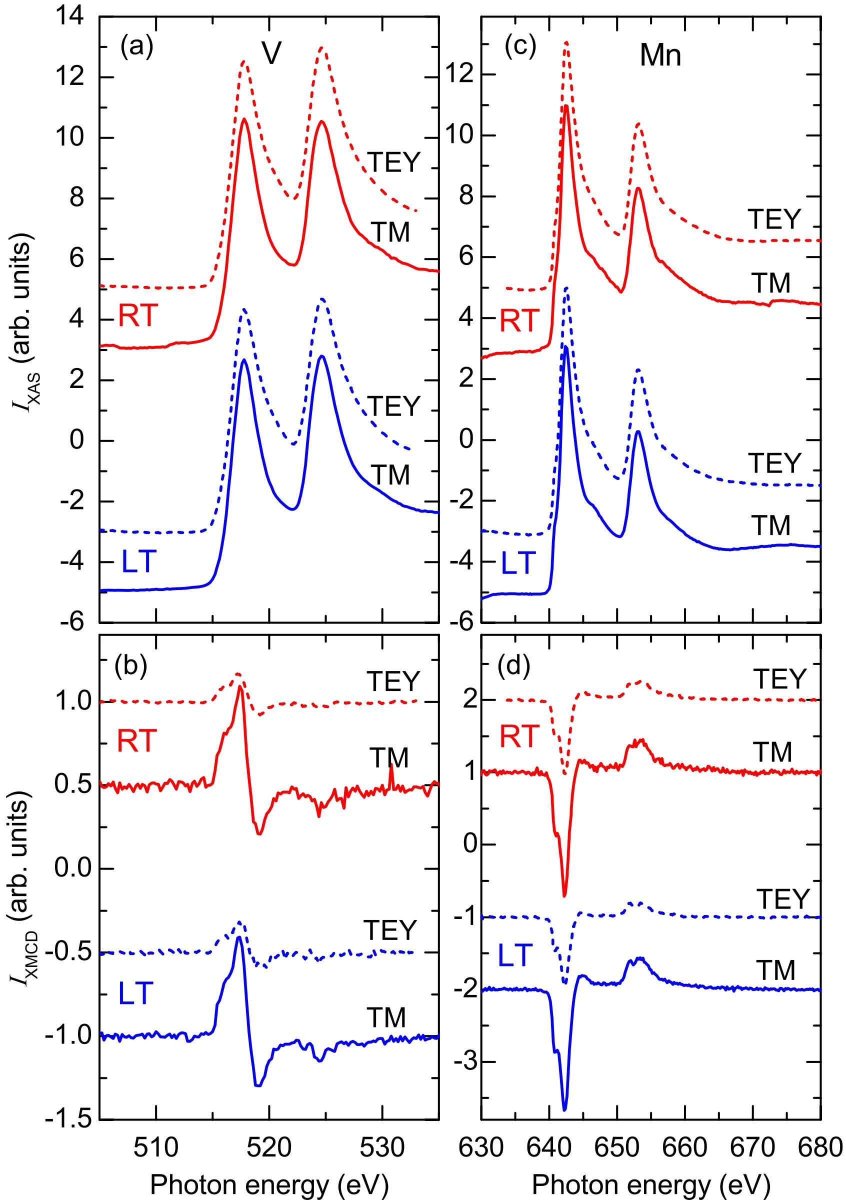

Figure 6.1: (a), and (c) X-ray absorption spectra I_{XAS} for Mn$_2$VAl measured at the V, and Mn L$_{3,2}$ edges averaged from intensities I^+ and I^- for magnetization direction parallel and antiparallel to the X-ray polarization. Full lines show the results for the transmission (TM) and dashed lines for the total electron yield (TEY) measurements at room temperature (RT = 300 K) and low temperature (LT = 120 K). (b), and (d) corresponding XMCD spectra $I_{\mathrm{XMCD}} = I^+ - I^-$.

	μ	Mn	V	$\mu_{\mathrm{Mn}}/\mu_{\mathrm{V}}$
TM, RT	μ_{spin}	1.03 ± 0.10	-0.95 ± 0.10	-1.08
	μ_{orb}	0.04 ± 0.05	-0.02 ± 0.05	
	μ_{XMCD}	1.17 ± 0.45		
TM, LT	μ_{spin}	1.14 ± 0.10	-0.90 ± 0.10	-1.27
	μ_{orb}	0.03 ± 0.05	-0.01 ± 0.05	
	μ_{XMCD}	1.43 ± 0.45		
TEY, RT	μ_{spin}	0.47 ± 0.10	-0.20 ± 0.10	-2.35
	μ_{orb}	0.02 ± 0.05	-0.03 ± 0.05	
	μ_{XMCD}	0.75 ± 0.45		
TEY, LT	μ_{spin}	0.48 ± 0.10	-0.22 ± 0.10	-2.18
	μ_{orb}	0.07 ± 0.05	-0.03 ± 0.05	
	μ_{XMCD}	0.85 ± 0.45		

Table 6.1: Element-specific magnetic spin moment μ_{spin} (μ_B per atom) and orbital moment μ_{orb} (μ_B per atom) for Mn$_2$VAl at room temperature (RT = 300 K), and low temperature (LT = 120 K) as calculated from the sum rules. The total moment μ_{XMCD} (μ_B per formula unit) results from weighted sum of the atomic moments. For the number of unoccupied $3d$ states the values $N_h(\mathrm{Mn}) = 4.5$ with additional jj-mixing correction factor 1.5, and $N_h(\mathrm{V}) = 8$ with additional jj-mixing correction factor 3 were assumed.

temperature in good accordance to the previously reported data (Ref. [WP99]) revealing atomic moments of 1.5 μB/atom for Mn and -0.9 μB/atom for V. *Ab initio* calculations from Ref. [GÖSA07] confirm the existence of the ferrimagnetic state comprising atomic moments that agree with the TM XMCD experiment. The Curie temperature of Mn$_2$VAl is far above room temperature at about 760 K. [WP99]

6.2.2 Co$_2$FeAl

Experimental XAS/XMCD results for Co$_2$FeAl measured at the Fe, and Co L$_{3,2}$ absorption edges are shown in Fig. 6.2. The spectra are looking similar for the TEY and TM data an no signs of oxidation are seen. For the low temperature (LT = 150 K) only the Co L$_3$ edge is prominent.

Co$_2$FeAl is ferromagnetic with a large magnetization of nearly 5 μ_B/f.u. as summarized in Tab. 6.2 in accordance with the predicted half-metallic properties in Ref. [FKW$^+$05]. Noticeable are the slightly larger magnetic moments for the TEY measurements maybe due to an improved local order and stoichiometry at the interface in contrast to the case of Mn$_2$VAl.

The epitaxial Co$_2$FeAl thin film is optimized for TMR devices as mentioned in Chap. 3. For TMR junctions the quality of the interface between the two ferromagnetic materials and the tunnel barrier is of utmost importance to guarantee a high spin polarization. [HAJ09]

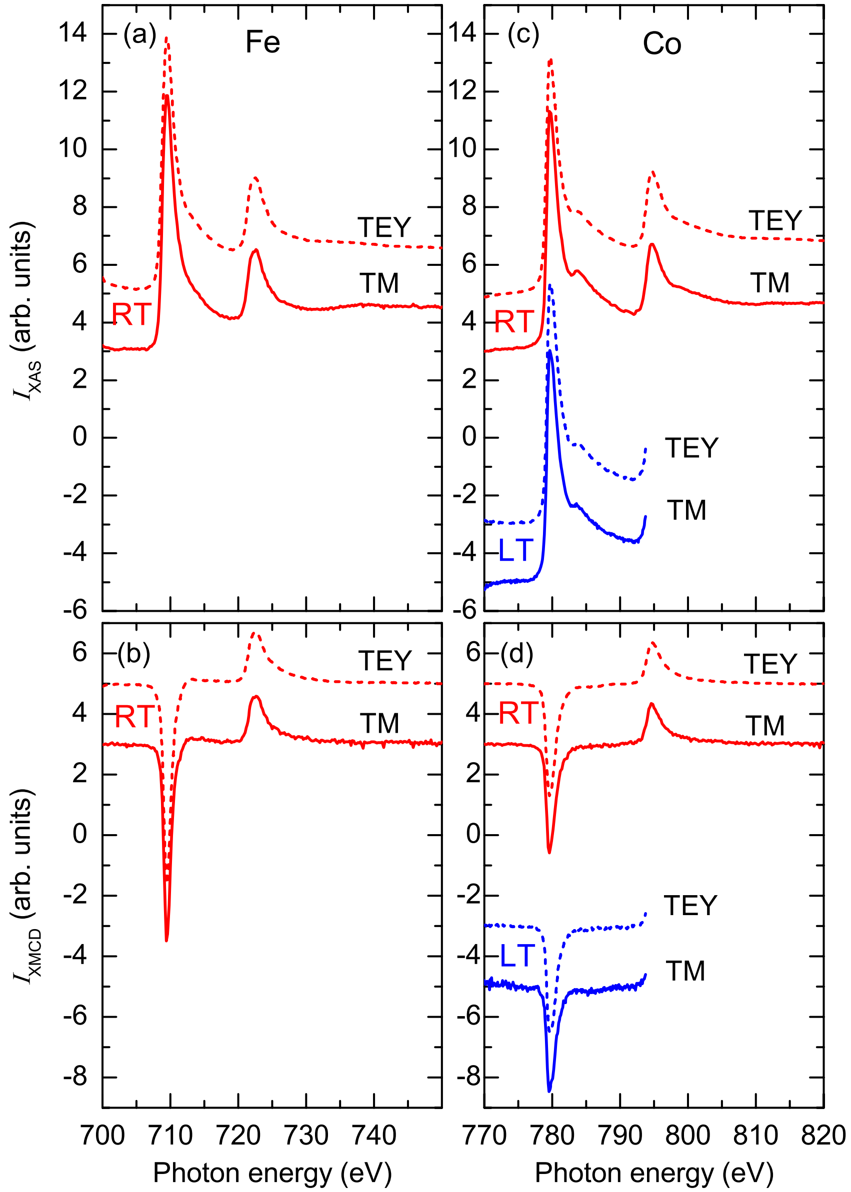

Figure 6.2: (a), and (c) X-ray absorption spectra I_{XAS} for Co$_2$FeAl measured at the Fe, and Co L$_{3,2}$ edges averaged from intensities I^+ and I^- for magnetization direction parallel and antiparallel to the X-ray polarization. Full lines show the results for the transmission (TM) and dashed lines for the total electron yield (TEY) measurements at room temperature (RT = 300 K) and low temperature (LT = 120 K). (b), and (d) corresponding XMCD spectra $I_{\text{XMCD}} = I^+ - I^-$.

	μ	Co	Fe	$\mu_{\text{Mn}}/\mu_{\text{V}}$
TM, RT	μ_{spin}	1.10 ± 0.02	2.05 ± 0.10	-0.54
	μ_{orb}	0.10 ± 0.02	0.07 ± 0.05	
	μ_{XMCD}	4.52 ± 0.23		
TEY, RT	μ_{spin}	1.14 ± 0.02	2.18 ± 0.10	-0.52
	μ_{orb}	0.10 ± 0.02	0.01 ± 0.05	
	μ_{XMCD}	4.67 ± 0.23		

Table 6.2: Element-specific magnetic spin moment μ_{spin} (μ_B per atom) and orbital moment μ_{orb} (μ_B per atom) for Co$_2$FeAl at room temperature (RT = 300 K), and low temperature (LT = 120 K) as calculated from the sum rules. The total moment μ_{XMCD} (μ_B per formula unit) results from weighted sum of the atomic moments. For the number of unoccupied $3d$ states the values $N_h(\text{Co}) = 2.5$, and $N_h(\text{Fe}) = 3.5$ were assumed.

6.3 Spin-resolved unoccupied density of states

6.3.1 Mn$_2$VAl

Experimental results for the Mn related PDOS in Mn$_2$VAl are visible in Fig. 6.3 (a), and (b) and compared to theoretical *ab initio* calculations (FLAPW+GGA) from Ref. [FKW$^+$05]. In the case of Mn$_2$VAl where the corresponding itinerant state is shifted far above E_F a correction of the majority Fermi energy is not necessary in contrast to Co-based Heusler alloys.

The minority states clearly reproduce the theoretical calculation considering the lifetime broadening of the spectral features. The large maximum at $E - E_F =$ 1.9 eV corresponds to the peak in the *ab initio* data at 1.7 eV. The pronounced shoulder closer to E_F is the remainder of the maximum in the theoretical data just below E_F. The pronounced maximum of the majority states observed at 2.2 eV above E_F is at variance with theory. This might be explained by static electron correlation effects that are not properly considered by the experimental PDOS evaluation procedure or by the theoretical calculation.

The majority state spectra are different for surface and bulk sensitive measurements. While the transmission data shown in Fig. 6.3 (b) reveal a decrease of the majority PDOS to almost zero at E_F for low temperatures, the TEY data show considerable spectral weight at E_F. This observation indicates half-metallic behavior for the bulk of the film with an energy gap in the majority DOS. In contrast the surface region of the film show normal metallic behavior.

A striking result is the pronounced temperature dependence of the bulk majority PDOS. Near E_F the in temperature rise to 300 K evokes a non-zero PDOS as shown in the inset of Fig. 6.3 (b). This change is clearly seen in the difference $D^{\downarrow}(300\text{ K}) - D^{\downarrow}(150\text{ K})$ that shows a maximum below E_F (see Fig. 6.3 (b)).

The temperature dependence cannot be explained by a thermal broadening of the Fermi function. Thermal broadening at 300 K is much smaller and would show an antisymmetric feature scheme below and above E_F. Such a temperature dependence is clearly absent for the case of the TEY related PDOS. The TEY

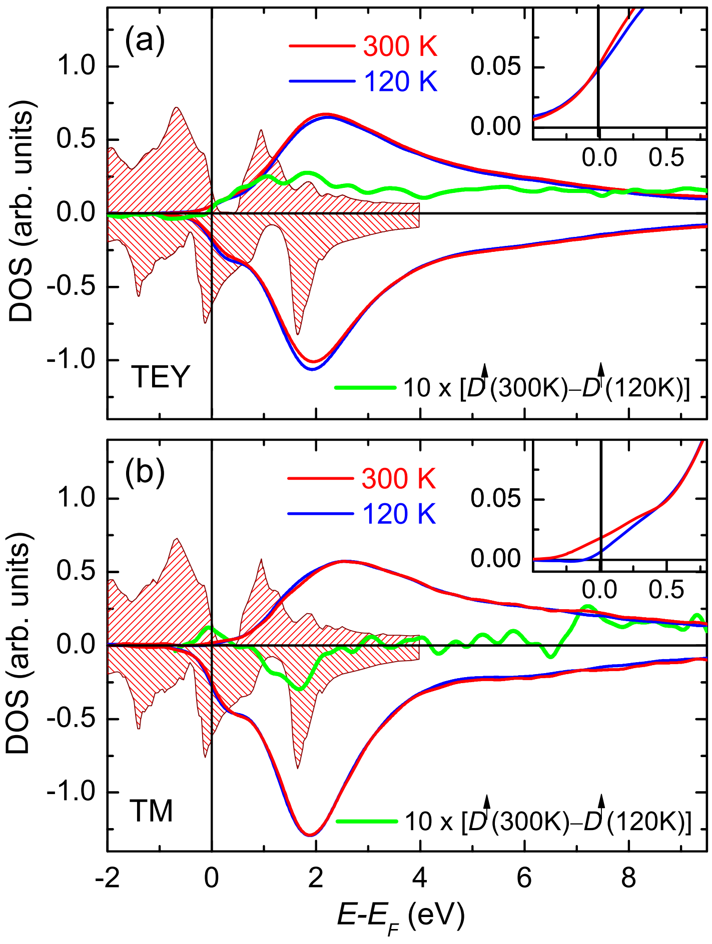

Figure 6.3: (a) Spin-resolved Mn PDOS calculated from the XAS/XMCD total electron yield (TEY) data measured at the Mn L$_3$ edge for Mn$_2$VAl. The difference $D^{\uparrow}(300\text{K}) - \text{D}^{\uparrow}(120\text{K})$ of the low- and high-temperature minority PDOS (dashed line) is tenfold enhanced, emphasizing the temperature induced spectral changes near the minority band gap. Theoretical *ab initio* calculations from Ref. [CAKL09] are indicated by the red area. The inset shows the magnified energy region near the Fermi energy E_F for the majority states. (b) Corresponding data for the spin-resolved Mn PDOS derived from the transmission (TM) data.

related PDOS (Fig. 6.3 (a)) shows a homogeneous temperature dependence as indicated by the energy independent difference. This remaining constant difference can be attributed to the strong temperature dependence of the interface magnetization resulting in an overall decrease of the XMCD signal.

6.3.2 Co$_2$FeAl

Fig. 6.4 (a), and (b) show the interface and bulk sensitive results similarly evaluated from the TM, and TEY data of the epitaxial Co$_2$FeAl film. For Co$_2$FeAl, the onset of the majority states appears at E'_F (see Fig. 6.4), which is a consequence of the fact that an itinerant $3d$-t_2 band dominates the unoccupied majority states near E_F. [FFB07] The different core hole screening for the itinerant and localized states produces an energy shift 0.5 eV for the onset of majority states.

The small X-ray intensity caused by the higher energy resolution chosen for this experiment produces increased noise of the TM data. In contrast to the Mn$_2$VAl film, measurements with lower resolution show clearly that the difference between TEY and TM data is almost negligible for this sample. This fact is attributed to the optimized preparation procedure for Co$_2$FeAl films. Hence, the electronic properties of the bulk and interface are nearly identical.

A large maximum of the minority PDOS at $E - E_F = 0.9$ eV followed by a weak shoulder at 1.2 eV and a second peak at 5 eV is observed. The position of the minority maximum is in good agreement with theory for this sample in contrast to the Co$_2$FeAl films investigated earlier [KKS$^+$09] where the maximum was shifted closer to E_F probably due to reduced local atomic order.

The difference of the minority PDOS $D^{\downarrow}(300\text{ K}) - D^{\downarrow}(150\text{ K})$ (Fig. 6.4 (a)) indicates a maximum value above E_F. The strong temperature dependence cannot be explained by a thermal broadening of the Fermi function. A similar difference of the PDOS might be inferred in the case of the transmission data as well (Fig. 6.4 (b)), despite the reduced signal-to-noise ratio. In both cases the maximum of the difference occurs 200 meV above E_F.

XAS/XMCD fully measures the unoccupied part of the PDOS. Thus, the observed small effect which is enhanced by the core hole correlation [IK05] corresponds to a tiny change in the spin polarization at E_F in good agreement with the recently observed small temperature dependence of the TMR effect for Co$_2$FeAl based tunnel junctions. [WSS$^+$09] In addition, the majority PDOS reveals a redistribution of the state occupancy at 0.8 eV above E_F (0.3 eV above E'_F), which is emphasized by the insets in Fig. 6.4 (a), and (b).

6.4 Temperature induced states

The increase in spectral weight with maximum just below the Fermi energy for the case of the TM data in Mn$_2$VAl with a majority band gap (see Fig. 6.3 (b)) is in qualitative agreement with the model of nonquasiparticle (NQP) states, calculated for real systems using LDA+DMFT. [CAKL09] The observed decrease in the majority PDOS above E_F agrees with the predicted half-metallic properties of Mn$_2$VAl. As up to now no experimental results of non half-metallic

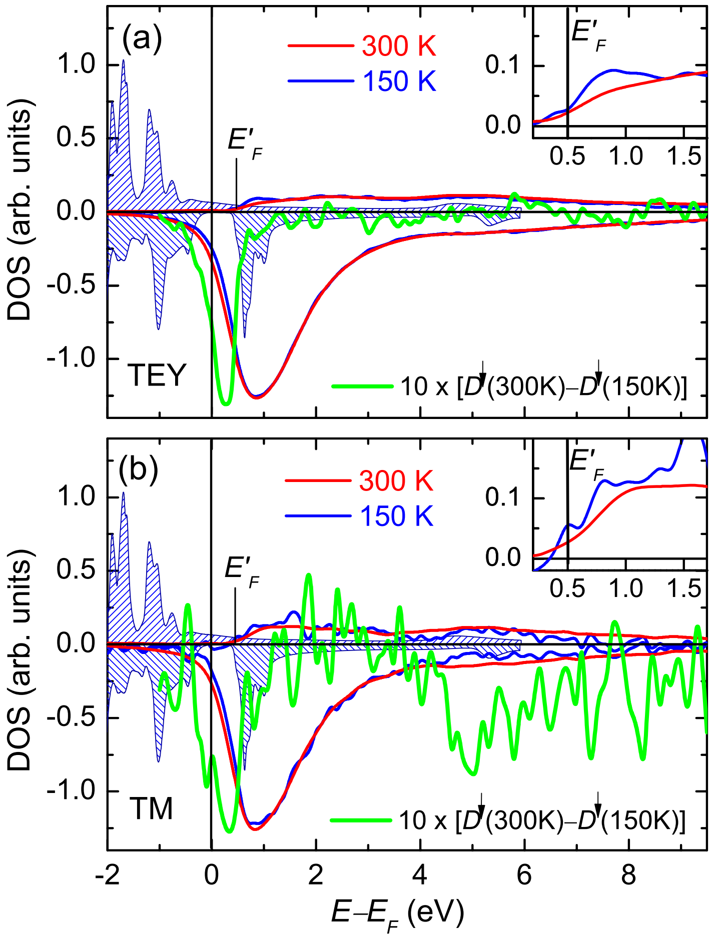

Figure 6.4: (a) Spin-resolved Co PDOS calculated from the XAS/XMCD total electron yield (TEY) data measured at the Co L_3 edge for Co_2FeAl. The difference $D^{\downarrow}(300\text{ K}) - D^{\downarrow}(150\text{ K})$ of the low- and high-temperature minority PDOS (dashed line) is tenfold enhanced, emphasizing the temperature induced spectral changes near the minority band gap. Theoretical *ab initio* calculations from Ref. [FKW$^+$05] are indicated by the blue area. The inset shows the magnified energy region near the Fermi energy E_F for the majority states indicating additional spectral changes. (b) Corresponding data for the spin-resolved Co PDOS derived from the transmission (TM).

properties of Mn$_2$VAl were reported, one may assume that the Mn$_2$VAl film is half-metallic in the bulk fulfilling the precondition for the existence of NQP states.

At the interface, the magnetization is clearly decreased and moreover shows a stronger temperature dependence. This can be attributed to difference to a less ordered structure at the interface probably due to a nonstoichiometric composition in this region originating from the large diffusion coefficient of Mn. Please note, that the films were optimized for large magnetization and structural properties measured by bulk-sensitive methods. The interface disorder obviously leads to an increased majority PDOS at E_F combined with a strong reduction in spin polarization. In this case no extra peak appears at E_F with increasing temperature.

The remaining temperature dependence of the spectra can be explained by a temperature induced spin mixing (spin fluctuations) according to a Heisenberg model. The absence of temperature-induced DOS changes beyond the single particle model is expected for a normal metal. Thus, for the case of Mn$_2$VAl all available experimental observations are consistent with the model of NQP states.

As shown before, in the case of Co$_2$FeAl an unexpected change of the PDOS with increasing temperature both for interface and bulk related data is observed (see Fig. 6.4). In the minority PDOS an extra peak appears slightly above E_F as predicted by the nonquasiparticle model. [CSA$^+$08] However, for Co$_2$FeAl conflicting results in respect to half-metallic ferromagnetic properties have been reported. This is a crucial point since half-metallicity is supposed to be a necessary condition for the emergence of NQP states. The PDOS observed in this work is not conclusive for a determination of half-metallicity in this sample due to the lifetime broadening of XAS in combination with the close vicinity of E_F and the upper band edge.

Although Ref. [FKW$^+$05] predicted Co$_2$FeAl to be half-metallic, other *ab initio* calculations resulted in a normal metal behavior with E_F crossing the conduction band edge. [MNS04] Ref. [MNS04] reported a spin polarization of just 30 % which was confirmed by a measurement of the spin polarization using magnetic tunneling junctions with an Al-O barrier (Refs. [OMS$^+$05], and [SEN$^+$10] considered as a good approximation of Jullière's model. The high TMR ratio reported in Ref. [WSS$^+$09] can be explained by coherent tunneling [WLK$^+$10] and is therefore consistent with a normal metal behavior of Co$_2$FeAl. The reported spin polarization measurements have determined spin polarization at the topmost Heusler layer near an interface. It is known that the surface spin polarization strongly depends on the atomic order and interface termination. The larger information depth of 2.5 nm for TEY data could lead to different results. This argument still opens the possibility that the Co$_2$FeAl film might be half-metallic and that the model of NQP states is a valid model to explain the results even though it is not compulsory.

In the following a short summary of the theory for NQP states as described in Ref. [KIC$^+$08, CAKL09] will be given: For half-metallic ferromagnets with a gap in the majority spin band NQP states appear just below the Fermi energy, while for half-metals with a gap in the minority spin band they occur just above

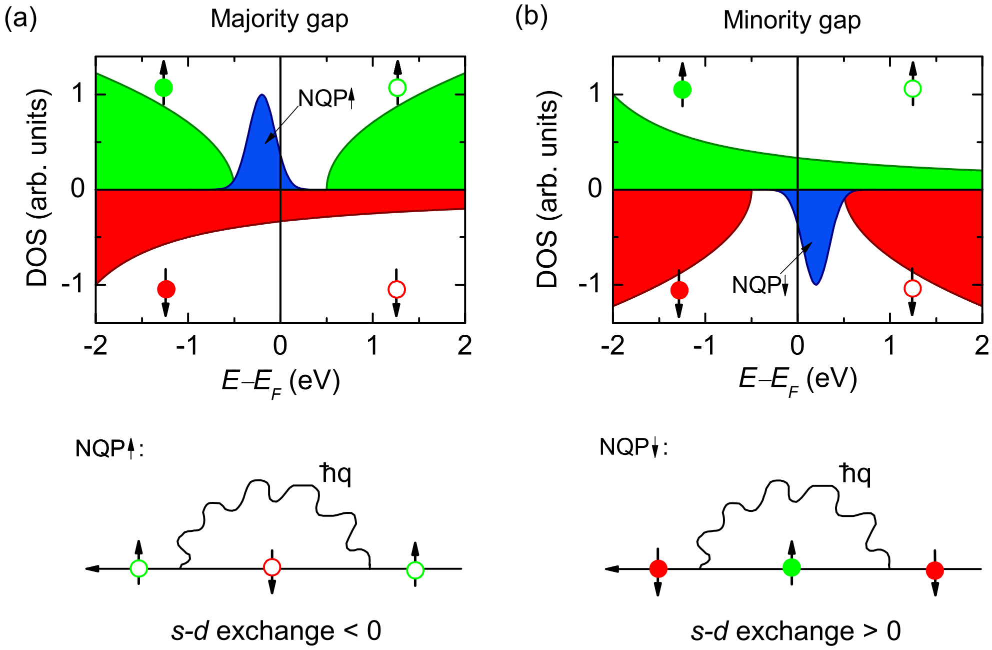

Figure 6.5: Schematic spin-resolved DOS in the single quasiparticle model of a ferromagnetic half-metal with the band gap in the majority (a) and minority (b) spin states. The additional spectral weight from NQP states is indicated by a Gaussian function with the maximum below (a) and above (b) the Fermi energy.

the Fermi energy as sketched in Fig. 6.5 (a), and (b).

In half-metallic ferromagnets with the band gap lying in the majority spin states and *s*-*d* exchange parameter < 0 the ferromagnetic ground state is non saturated and zero-point magnon fluctuations are allowed. Occupied minority spin states can be superposed with majority electron states plus magnons to conserve the total spin projection. Thus, occupied majority electron NQP states occur below E_F. For the *s*-*d* exchange parameter > 0 the band gap appears in the minority electron band. In this case, a superposition of the majority electron excitations plus virtual magnon states leads to NQP states in the majority band above E_F conserving the total spin projection. The spectral weight of the NQP states increases with increasing temperature and their tail crosses the Fermi energy.

Further experimental observations in conflict with the NQP model exist. Temperature induced spectroscopic changes observed for majority states of Mn_2VAl at 1.5 eV above E_F and Co_2FeAl at 0.3 eV above E_F are not reproduced by the NQP model. [CSA+08] Moreover, the predicted temperature dependence of the DOS originating from NQP states is very small compared to observation here. [CSA+08] A recent high energy photoemission study of the half-metallic Heusler alloy Co_2MnSi investigated in Ref. [MKM+09] found no temperature dependence of the valence band spectrum, which is inconsistent with the NQP model. On the other hand, the photoemission study might not be in full conflict with our results as the interaction with the core hole during the X-ray absorption process essentially enhances the spectral weight of the NQP-induced changes in the PDOS according to LDA+DMFT calculations. [IK05] This makes XAS measurements more sensitive to NQP states compared to photoemission.

Thus, at present the model of NQP states explains the experimental observations for Mn$_2$VAl while in the case of Co$_2$FeAl the precondition of half-metallicity is probably not fulfilled and spectral features in addition to the NQP model occur. Therefore, the XAS/XMCD experimental work cannot justify the NQP model as the exclusive explanation for the observed temperature-induced spectral changes. Probably more detailed LDA+DMFT calculations for Co$_2$FeAl including B2 order instead of L2$_1$ order would clarify if compounds close to half-metallicity showed temperature dependencies beyond the single particle model. Further experimental work providing a better empirical basis for the occurrence of an unexpected temperature dependent DOS is required. As an alternative explanation one might consider phonon-induced interactions [MLH$^+$07] or a temperature dependent exchange splitting [BGK$^+$99]. Also structural changes below the detection limit of X-ray diffraction should be taken into account.

6.5 Summary

Temperature dependent XAS/XMCD measurements have been performed for Mn$_2$VAl, and Co$_2$FeAl thin film samples. Mn$_2$VAl is a ferrimagnet with strongly reduced magnetic moments at the surface resulting from local disorder. The magnetic moment in bulk meets to theoretical *ab initio* calculations. In contrast, surface and bulk magnetic moments in ferromagnetic Co$_2$FeAl are nearly equal and agree well with *ab initio* calculations. Moreover, temperature induced changes in the spin-resolved DOS of two Heusler compounds that cannot be explained by thermal excitations within a single particle model are discussed. A temperature induced spectral change in the PDOS for Mn$_2$VAl for which theory predicted a majority band gap at E_F is shown. A spectral change is also observed for Co$_2$FeAl for which theory predicted a minority band gap or at least a pronounced minimum of the minority PDOS at E_F. In the case of Mn$_2$VAl the spectral changes include a peak like increase in the partial DOS just below E_F and for Co$_2$FeAl just above E_F. These features are consistent with model of non-quasiparticle states. The spectral weight of the NQP states increase with increasing temperature and their tail crosses the Fermi energy leading to depolarization. Admittedly, in the case of Co$_2$FeAl more details of our experimental results are partly inconsistent with the predictions of the NQP model. Moreover, previously reported results suggest that Co$_2$FeAl is not a true half-metallic ferromagnet which is considered as a necessary condition for the NQP model. Hence, the experimental results do not unambiguously justify the observation of NQP states. Further progress in the understanding of many-body effects is needed to explain the reported results.

Chapter 7

Angular dependence of XMCD spectra for Ni_2MnGa films

7.1 Motivation

Ferromagnetic shape memory alloys (SMA) are a class of materials where magnetic anisotropy is of utmost importance. A magnetically induced strain of about 10 % by the rearrangement of twin variants in the martensitic phase is possible. [Ots98, ASU02] Epitaxial SMA films are an important first step for the fabrication of micro-actuators based on free standing films. [PKE$^+$08, HTB$^+$08, THB$^+$09] The driving force for the rearrangement of twin variants is delivered by the magnetic anisotropy energy. [O'H98, EANN02, KRH$^+$10] Therefore, an understanding of the electronic structure [OMS$^+$08] and in particular of the microscopic origin of the magnetic anisotropy [CGB$^+$10, UHN$^+$09] is of great interest.

Models relating the magnetic crystal anisotropy to the atomic orbital moment anisotropy have been successfully used to phenomenologically explain surface anisotropy in ultrathin films. [WSN$^+$95, DGvdL$^+$97, Bru89] According to these models the orbital moment component parallel to the magnetization is partly suppressed when the magnetization vector is forced along the magnetic hard axis. Recently, however, orbital moment measurements on Au/Co/Au films showed a maximum value along the hard axis, in contrast with previous experience and indicating that the orbital moment anisotropy is not proportional to the magnetic anisotropy. [ASE$^+$07] This observation was attributed to the large spin-orbit interaction within the Au at the interface.

Another puzzling result of *ab initio* theory is the increase of the orbital moment for hard axis magnetization in Ni_2MnGa. [GEOR08] Therefore, an experimental observation of spin and orbital anisotropies for bulk systems, where interface effects can be neglected, is indispensable for establishing a thorough understanding of magnetic anisotropy.

In this chapter, epitaxial thin films are studied with predominant itinerant electron states. The spectroscopic information obtained by angle-resolved XMCD reveals a distinct information on the electronic states that are relevant for the anisotropy energy. It provides an experimental support for a simple

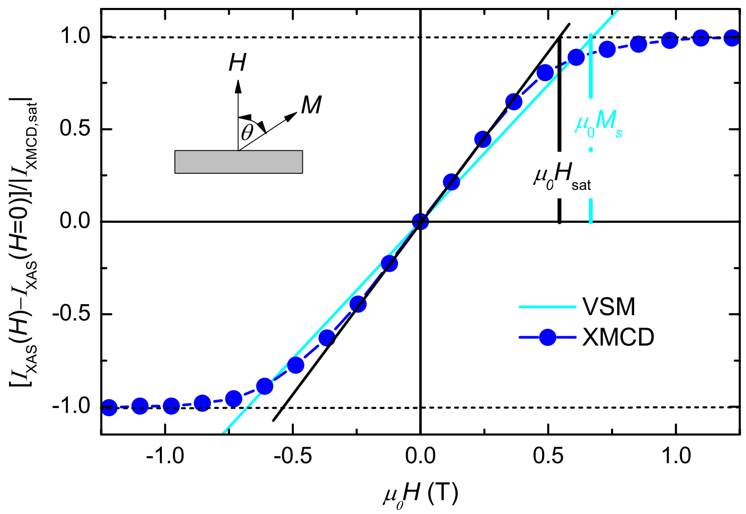

Figure 7.1: X-ray absorption $I_{\text{XAS}}(H)$ from the transmission (TM) data versus external field H applied perpendicular to the film surface (dots). The zero field value $I_{\text{XAS}}(H=0)$ was subtracted and the difference was normalized to the saturation value $|I_{\text{XMCD,sat}}| = |I_{\text{XAS}}(+H_{max}) - I_{\text{XAS}}(H=0)| = |I_{\text{XAS}}(-H_{max}) - I_{\text{XAS}}(H=0)|$ measured at high magnetic field $\mu_0 H_{max} = 1.2$ T. The cross section of the initial susceptibility (black line) with the saturation value indicates the saturation field H_s. The initial susceptibility determined by VSM, if only the shape anisotropy field $M_s = J_s/\mu_0$ is present, is drawn for comparison (light blue line). The VSM measurement was perfomed by T. Eichhorn (AK Felser).

model of magnetic anisotropy in Ni$_2$MnGa based on the anisotropy of atomic orbitals in a tetragonally distorted system in combination with spin-orbit coupling. Specific spectroscopic anisotropies in the XMCD spectra will be related to contributions in the DOS function originating from high-symmetry points at the Brillouin-zone boundary. [Stö99]

7.2 Magnetic anisotropy

Exploiting the magneto-optical contrast of XMCD the out-of-plane magnetic anisotropy was measured by-hard axis magnetization loop as shown in Fig. 7.1. The magnetization loop was determined at the Mn L$_3$ absorption edge providing the largest magnetic contrast. The X-ray absorption signal $I_{\text{XAS}}(H)$ was measured at constant right circular polarization varying the external field applied perpendicular to the surface in steps of approx. 0.1 T. The value $I_{\text{XAS}}(H=0)$ measured at zero external field was subtracted and the signal was normalized to the maximum value $|I_{\text{XMCD,sat}}|$ measured at an applied magnetic field $\mu_0 H_{max} = 1.2$ T.

Neglecting interface anisotropies the out-of-plane uniaxial anisotropy energy

$$f(\theta) = L\cos^2(\theta) \tag{7.1}$$

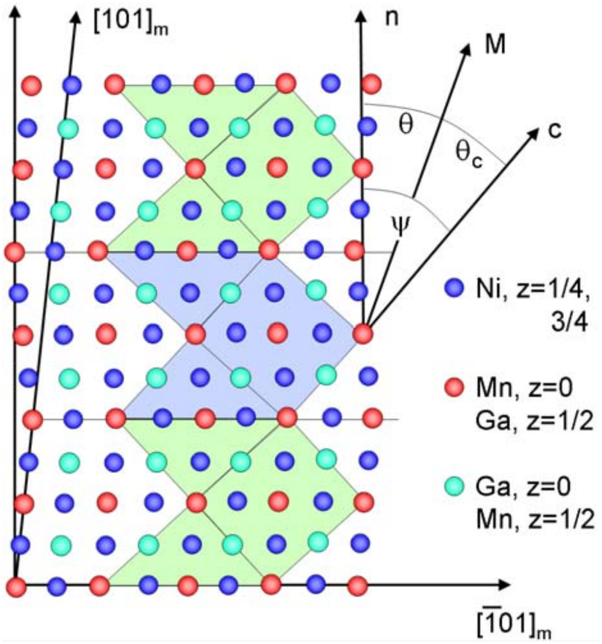

Figure 7.2: (c) Structural model of the martensitic phase ($T < T_m$) with position of the (101) twin planes parallel to the film surface along the Ni$_2$MnGa[010] axis.

can be written as a sum of shape anisotropy and crystal anisotropy according to $L = J_s^2/2\mu_0 + K_v$ with J_s being the saturation magnetization, K_v the bulk anisotropy constant and θ the angle between magnetization vector and surface normal. From the saturation field H_s an experimental result for the out-of-plane anisotropy constant K_v is obtained that is related to L by $H_s = 1/J_s \cdot \partial^2 f(\pi/2)/\partial\theta^2 = 2L/J_s$. This leads to the equation $H_s = J_s/\mu_0 + 2K_v/J_s$. The anisotropy constant $K_v = H_{anis}J_s/2 = -3.7 \times 10^4$ Jm^{-3} can be calculated with the values of the saturation magnetization $J_s = \mu_0 M_s = 0.675$ T determined by VSM magnetometer and the saturation field $\mu_0 H_s = 0.537$ T determined from the XMCD hard axis loop (see Fig. 7.1). This results in a crystal anisotropy field $\mu_0 H_{anis} = \mu_0 H_s - J_s = -0.138$ T defined by $H_{anis} = 2K_v/J_s$.

The negative sign of the crystal anisotropy field indicates the direction of the magnetic easy axis being out-of-plane (perpendicular to the surface). Assuming that the anisotropy is exclusively caused by the Ni related states the anisotropy per Ni atom e_{Ni} can be calculated from K_v according to $e_{Ni} = K_v a_c^3/8 = -5.7$ μeV assuming that the volume value a_c^3 in the cubic and martensitic phase is equal. The volume of the cubic unit cell (lattice constant $a_c = 0.581$ nm) is determined by X-ray diffraction and discussed in Chap. 3.4.3. The value 8 accounts for the eight Ni atoms in the Heusler unit cell. The magnetic out-of-plane anisotropy constant is in agreement with previously reported results for epitaxial Ni$_2$MnGa films [CGB$^+$10, GRC$^+$09], but an order of magnitude smaller than values for bulk single crystals [OA02].

This discrepancy can be explained by taking into account the eight different oriented variants (explained in Chap. 3.4.3). The origin of the magnetic anisotropy is the c/a ratio being smaller than one, resulting in an easy axis along the shorter c-axis within each twin variant. Because the length scale of the twin variant structure is much larger than the magnetic exchange length, the magnetization is homogeneous within the film. Therefore, the variant structure (Fig. 7.2) results in the measured out-of-plane anisotropy. The anisotropy in an individual twin variant can be calculated by

$$f_v(\theta', \phi') = K_c \cos^2 \theta' + K_b \sin^2 \theta' \sin^2 \phi' \tag{7.2}$$

with the polar angle θ' and azimuthal angle ϕ' of the magnetization vector with respect to the c and a axis of the individual variant. The crystal anisotropy constants K_c and K_b are related to the c and b axis. For averaging the magnetic anisotropy of the first set of variants a rotation of the magnetization within the plane has to be considered that is described by the polar angle θ (see Fig. 7.2) between the film normal and the magnetization vector. Thus, Eq. 7.2 simplifies to $f_v(\theta', \phi' = 0) = K_c \cos^2 \theta'$. Because the $[\bar{1}01]_m$ axis deviates by only a small angle 9.74° from the MgO[010] axis, the azimuthal tilt can be neglected and Eq. 7.2 can be applied to the set of two twin variants shown in Fig. 7.2. Averaging over the two twin variants tilted by $\pm\psi$ by using the transformation $\theta' = \theta \pm \psi$ leads to an averaged free energy

$$f(\theta, 0) = K_c(\cos^2 \psi) + K_b \sin^2 \psi \sin^2 \phi \tag{7.3}$$

The angle ψ between the c axis and the film normal is given by $\psi = \arctan(c/a)$.

A further set of four variants exists by rotating the azimuthal angle of $\phi = 90°$. For these variants the small azimuthal tilt of 9.74° is neglected, too. For the case $\theta = 0°$ (out-of-plane magnetization), the free energy is the same as in the case discussed before and one obtains $f(0, \pi/2) = f(0, 0) = K_c \cos^2 \psi$. For $\theta = \pi/2$ (in-plane magnetization) the magnetization vector is directed parallel to the b axis, $[010]_m$, and one obtains $f(\pi/2, \pi/2) = f_v(\pi/2, \pi/2) = K_b$ according to Eq. 7.2. Therefore, the average anisotropy of this second set of variants can be described by

$$f(\theta, 0) = (K_c \cos^2 \psi - K_b) \cos^2 \theta + K_b. \tag{7.4}$$

The average over the two sets of variants (Eqs. 7.3 and 7.4) leads to the average total free energy

$$f(\theta, 0) = [(K_c(\cos^2 \psi - \frac{1}{2} \sin^2 \psi) - \frac{1}{2} K_b] \cos^2 \theta. \tag{7.5}$$

This averaging step cancels the first-order in-plane anisotropy because an azimuthal rotation by $\phi = 90°$ transforms the anisotropy of the first set of variants into the anisotropy of the second set and vice versa. A pure uniaxial anisotropy remains by neglecting higher-order anisotropies.

Including the experimental value $\psi = 42.3°$ in Eq. 7.5 leads to a crystal anisotropy $f(\theta, 0) = [0.32K_c - 0.5K_b]cos^2\theta$. Compared to Eq. 7.1, the relation $K_v = 0.32K_c - 0.5K_b$ links the single variant anisotropy constants, K_c, and K_b, to the experimentally measured crystal anisotropy constant K_v.

From the relation of the lattice constants $a > b > c$ one expects that K_b has an intermediate value according to $0 > K_b > K_c$. In the case of two equal easy axes, i.e. equivalent to a tetragonal symmetry with one long and hard axis as discussed by theory [EBK$^+$06, PKE$^+$08], it can be assumed that $K_b = K_c$. K_c is supposed to be negative because of the easy axis along the c axis of a single variant. The tetragonal symmetry assumption results in an effective anisotropy constant $K_v = -0.18K_c > 0$ with reversed sign in contradiction to the experimental result.

A more appropriate assumption is $K_b = 0.5K_c$ taking into account that b is approximated by $b = (a + c)/2$. A similar relation for K_b was experimentally observed in Ref. [KRH$^+$10] and explained by a 14-M superstructure based on subunit cells with tetragonal symmetry. From this assumption $K_v = 0.07K_c$ is obtained. The sign is conserved and the measured anisotropy constant K_c is an order of magnitude smaller than the anisotropy K_v of an individual variant.

In summary, a crystal anisotropy with an easy axis pointing out of the film plane is found that is outbalanced by the shape anisotropy resulting in an easy plane anisotropy of the film. The crystal anisotropy K_v averaged over the eight variants is comparatively small but exhibits an order of magnitude larger values in a single twin variant. Assuming $K_b = 0.5K_c$ for the anisotropy energies along the c and b axis with respect to the a axis of an individual twin variant one obtains a single variant anisotropy constant of $K_c = -0.53 \times 10^4$ Jm^{-3} corresponding to a single atom anisotropy of $e_{c,Ni} = -81$ μeV, which is in agreement with previous observations in Ref. [KRH$^+$10].

7.3 Angular dependent spectroscopical changes

Angular dependent X-ray magnetic circular absorption spectroscopy was performed in transmission for Ni$_2$MnGa. The external magnetic field of 1.22 T was applied parallel to the X-ray polarization vector. The XMCD results measured at the Ni L$_{3,2}$ edge for different angles (angle θ) between X-ray beam and surface normal are summarized in Fig. 7.3. The absorption spectra I_{XAS} were calculated from the transmitted intensity. For $T > T_m$ (austenite state) no variations of the spectra depending on angle θ are observed as expected for the cubic symmetry. The characteristic satellite peak at point A indicates the symmetry of the L2$_1$ ordered austenite state. Instead, in the martensitic state $T < T_m$ distinct changes in the spectra reveal the influence of the reduced crystal symmetry. Peak A is absent in the XAS spectra and a systematical variation of peak B, and C is visible. Peaks A, and B show a reduction with increasing angle θ between magnetization and surface normal. XAS/XMCD data at the Mn L$_{3,2}$ edge have also been measured and show no significant changes with incident angle above and below T_m. Thus the magnetic anisotropy is mainly caused by the Ni related electronic states as mentioned before, although the Mn spin moment is eight times larger [KPE$^+$09] than the Ni spin moment.

Effective magnetic spin moment μ_{spin} and orbital magnetic moment μ_{orb} resulting from the sum rule analysis for Ni are plotted in Fig. 7.4. For the martensitic state $T < T_m$ the orbital moment decreases with increasing angle θ. For $T > T_m$ no changes are observed. The spin moment is constant for both cases $T > T_m$, and $T < T_m$ revealing a minor effect from the magnetic dipole

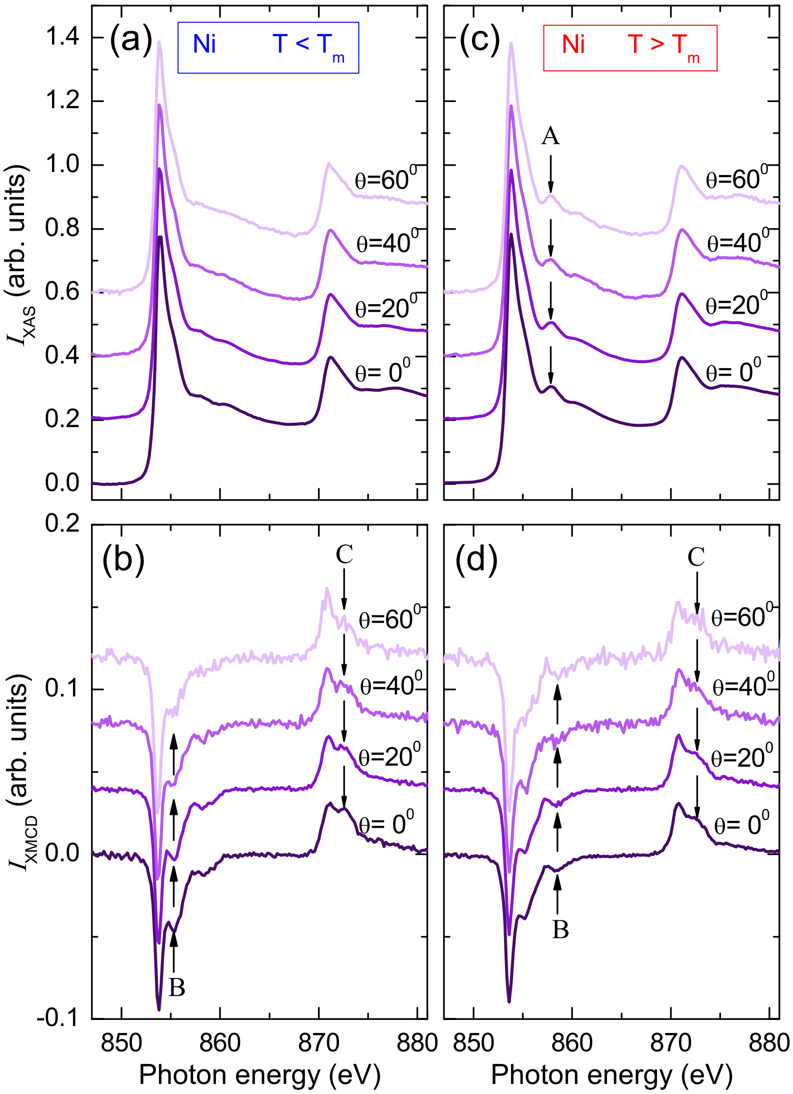

Figure 7.3: (a), and (b) X-ray absorption spectra of Ni$_2$MnGa at the Ni L$_{3,2}$ edge averaged from the transmitted X-ray intensity (I_{XAS}) measured at $T = 200$ K ($T < T_m$) and $T = 300$ K ($T > T_m$) for magnetization direction parallel (antiparallel) to the X-ray polarization, $I^{+(-)}$. The variation of the incidence angle between X-ray beam/magnetization and the surface normal is indicated in the figure. Peak A marks the satellite peak emerging in the austenitic state [JEKE07]. Spectra and arrows are shifted with an identical offset for clarity. (b) and, (d) Corresponding XMCD spectra, $I^+ - I^-$. Peaks B and C indicate angular dependent spectral changes caused by Ni d states with d_{xy} symmetry.

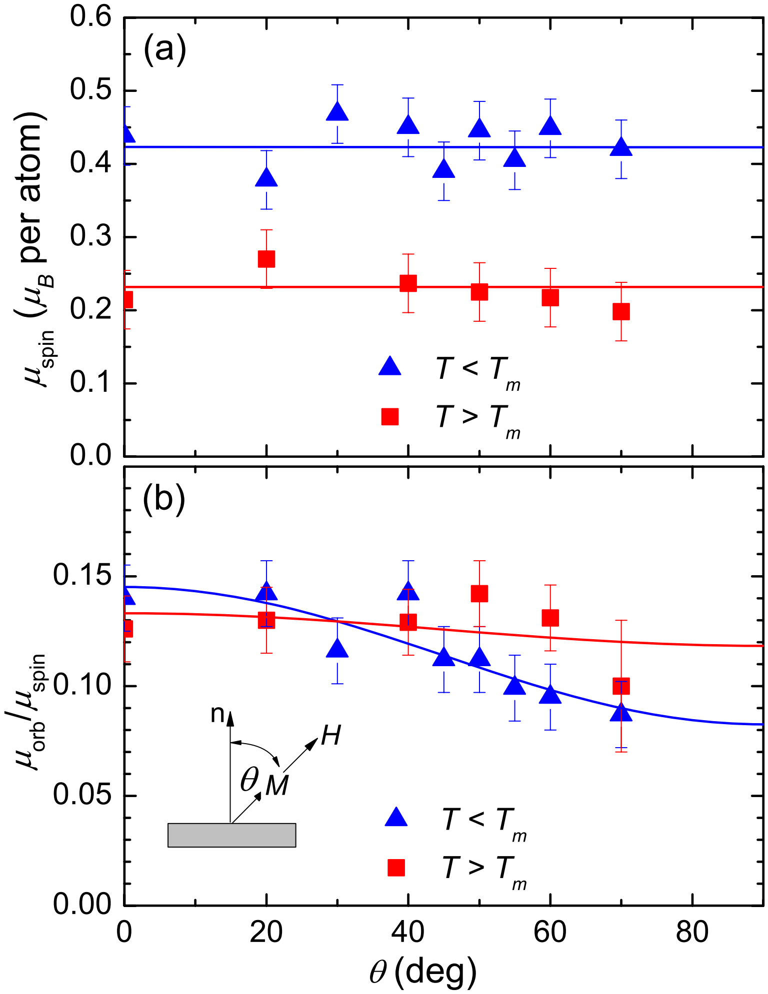

Figure 7.4: (a) Angular dependence of the effective spin moment μ_{spin} (μ_B per atom) resulting from the sum rule analysis at the Ni $L_{3,2}$ edge for Ni$_2$MnGa. The effective spin moment includes the magnetic dipole term. Horizontal lines indicate the corresponding mean value of the effective spin moment. (b) Orbital to spin moment ratio μ_{orb}/μ_{spin}. For the number of unoccupied d states the value of $N_h = 1.5$ for Ni was assumed. Full lines result from a fit to the function $\mu_{orb} = \mu_{orb}(0) - \Delta\mu_{orb} \sin^2 \theta$.

operator.

Now, the magnetic anisotropy e_{Ni} determined above can be compared with the anisotropy of the orbital magnetic moment Δm_{orb}. The negative sign of the crystal anisotropy is in qualitative agreement with the observed decrease in the orbital moment along the hard in-plane axis. A quantitative relation of the orbital moment variation Δm_{orb} and the magnetic anisotropy:

$$e_{\mathrm{Ni}} = -C\frac{\xi}{4\mu_B}\Delta m_{orb} \tag{7.6}$$

is discussed by Bruno [Bru89]. ξ denotes the spin-orbit coupling energy with a value of 50 meV in the case of Ni and C a constant depending on the band structure. C is estimated to be smaller than 1/5 in accordance to Ref. [Stö99]. Please note, that the same reduction factor for variant averaging applies for e_{Ni} and Δm_{orb}. Using the experimental values ($e_{\mathrm{Ni}} = -5.7$ μeV, and $\Delta m_{orb} = 0.026$ μ_B) in Eq. 7.6 one can calculate $C = 0.018$. This value is roughly an order of magnitude smaller than expected. Thus can be explained by a small exchange splitting relative to the bandwidth.

In Fig. 7.5 (b) spectroscopic changes in the Ni spectra with the magnetization angle are emphasized by plotting the difference of the XMCD signal, $I_{\mathrm{XMCD}}(0°) - I_{\mathrm{XMCD}}(60°)$, at normal incidence and at $\theta = 60°$. In a simple model one may interpret the difference as changes in the density of states at the Ni site. This interpretation is further supported by the fact that data at the L$_3$, and L$_2$ edge are similar but with opposite sign. The opposite sign of the spectral shape observed at the L$_3$ and L$_2$ edge is a direct hint that the angular dependence is due to the spin asymmetry rather than to the orbital asymmetry. The changes of the DOS are attributed to changes of the minority DOS because the featureless majority DOS remains mostly unchanged. For this reason, the angular dependence of the XMCD probes the angular dependence of the minority DOS. Please note, that the spin polarization of electrons is opposite at the L$_3$, and L$_2$ edge and in the usual notation the XMCD signal is negative at the L$_3$ edge (spin polarization $P_{\mathrm{L}_3} = 0.25$ at the L$_3$ edge and $P_{\mathrm{L}_2} = -0.5$ at the L$_2$ edge, see Chap. 2.1). A positive difference $I_{\mathrm{XMCD}}(0°) - I_{\mathrm{XMCD}}(60°) > 0$ at the L$_3$ edge (L$_2$ edge) indicates a stronger (weaker) absolute XMCD signal for the in-plane orientation and thus an increased (decreased) minority DOS for the magnetic field aligned in-plane the film.

The rotation of the magnetization affects the d states in a different way depending on the twin variant where the X-ray photon is absorbed. In the transmission XMCD experiment the measured signal results in an implicit average over the eight twin variants. Therefore, angular dependent spectroscopic changes in the Ni XMCD spectra in a single variant should be much more pronounced. Similar to the case of the magnetic anisotropy this average leads to an effective uniaxial anisotropy of the electronic states, which is equivalent to a tetragonal structure with the short axis directing along the film normal.

In Fig. 7.5 (a) a comparison with the calculation by Ayuela et al. [AEN02] (FLAPW code) is shown. The calculated DOS is plotted versus energy (for the L$_3$ and L$_2$ edge, respectively). The Fermi energy is set to zero (see top axis). For X-ray absorption, electrons are excited from the 2p states ($2p_{3/2}$ and

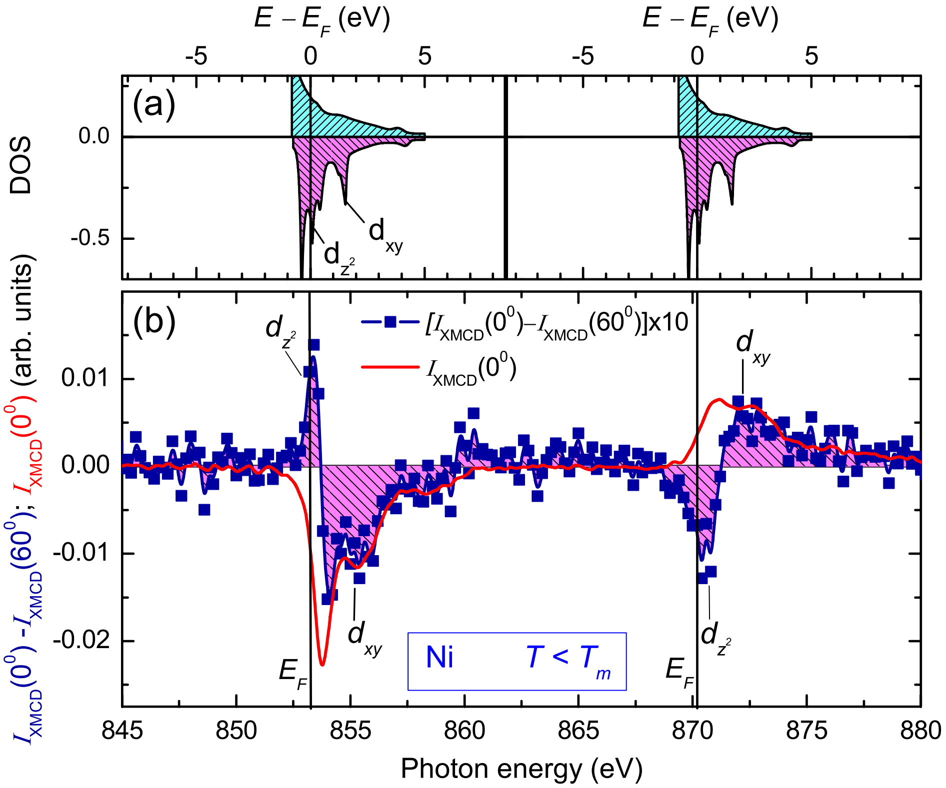

Figure 7.5: (a) Site spin-projected d electron state densities for Ni in the case of $c/a < 1$ resulting from *ab initio* calculations [AEN02] shifted along the energy axis for direct comparison to the experimental data. (b) Difference of the XMCD signal (dark blue squares) measured at $\theta = 60°$ and normal ($\theta = 0°$) incidence for $T < T_m$. Full red line shows for comparison the XMCD signal measured at normal incidence.

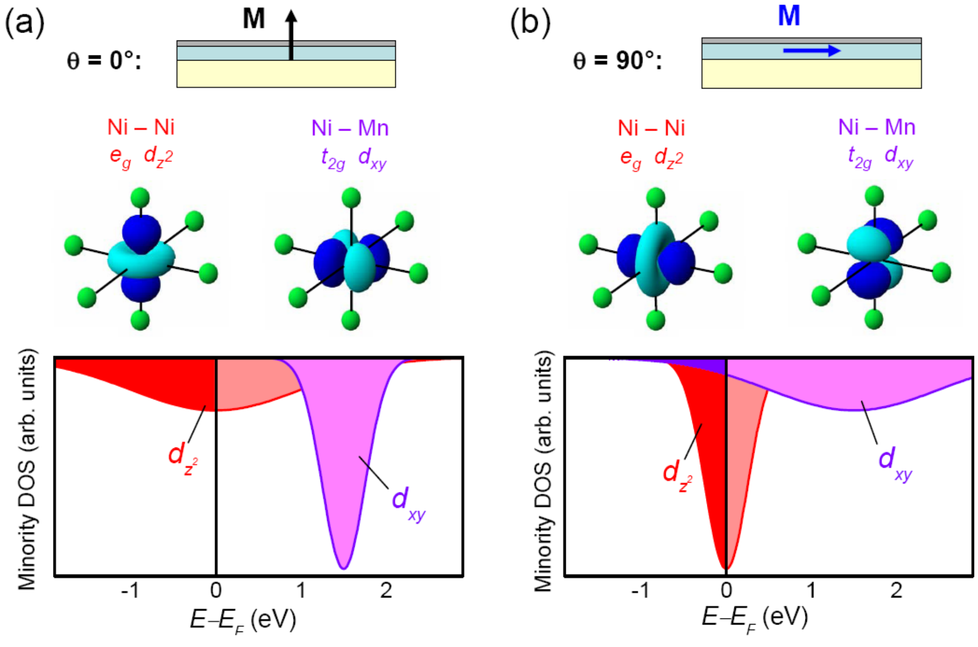

Figure 7.6: (a) Sketch of the orbital symmetry of electron states with $d_{3z^2-r^2}$ (d_{z^2}) and d_{xy} symmetry indicating the dominating contribution to the DOS maxima for out-of-plane magnetization direction (b) Corresponding sketch for in-plane magnetization direction.

$2p_{1/2}$ states) of Ni which are splitted by 16.9 eV due to the core shell spin-orbit coupling and thus lead to two well separated absorption edges L$_3$, and L$_2$. The binding energies E_b of the $2p$ states are 853.2 eV ($2p_{1/2}$) and 870.1 eV ($2p_{3/2}$). Thus a photon energy of $E_{ph} = h\nu$ excites electrons into unoccupied states above the Fermi energy at $E - E_F = E_{ph} - E_b$. In order to compare the XMCD signal with the calculated DOS the axis in Fig. 7.5 (a) has been arranged in such a way that the energy scale is identical but shifted by E_b for both absorption edges.

The experimental results in comparison with theory identifies the minority DOS maximum close to E_F with a $d_{3z^2-r^2}$ (d_{z^2}) state. The d_{z^2} state shows with its long axis parallel to the magnetization outlined in Fig. 7.6.

With out-of-plane magnetization (Fig. 7.6 (a)) the nearest neighbor atoms (Ni-Ni) are close-by because of the tetragonal distortion. Hence, the hybridization is large leading to a larger bandwidth explaining the smaller d_{z^2} peak. For the minority d_{xy} state at 1.5 eV above E_F the situation is opposite. The nearest neighbor atoms (Ni-Mn) are positioned at a larger distance. This leads to a weaker hybridization and to a larger d_{xy} peak because the electronic states are stronger localized at the atoms.

If the magnetization is rotated along the in-plane direction (Fig. 7.6 (a)), the d_{z^2} state hybridizes less with the neighboring atoms positioned at a larger distance. Accordingly, the bandwidth is smaller and the corresponding minority d_{z^2} peak is larger. For the minority d_{xy} states the peak decreases and the hybridization is larger due to the closed-by Ni-Mn atoms.

The larger bandwidth of states with d_{z^2} symmetry for $\theta = 0°$ positioned directly above the Fermi energy reflects an increase of states below E_F with lower kinetic energy due to the energetic broadening of these states. This reallocation of the these occupied states decreases the total energy of the system. This explains the occurrence of magnetic anisotropy with an easy axis along the perpendicular (short) axis. The magnetic quantum number of a state with d_{z^2} symmetry is zero and does not contribute to the orbital moment.

On the other hand, the increased bandwidth of the minority DOS for states with d_{xy} symmetry for $\theta = 90°$ reflects the increase of states below E_F. d_{xy} symmetry states have a non-zero magnetic quantum number. Therefore, an increase of the occupied minority DOS causes an increase of the minority orbital magnetic moment because the spin-orbit interaction favors parallel orbital and spin magnetic moments. This increased minority orbital moment causes a decreased total orbital magnetic moment, in fact, as measured for the in-plane magnetization (see also Fig. 7.4).

7.4 Summary

A change of the electron density of states in Ni$_2$MnGa is caused by the rotation of the magnetization vector with respect to the crystal lattice. A model absorption experiment was performed aligning the circular X-ray polarization and the magnetization with a large external field and varying the angle of incidence. By measuring XAS/XMCD in transmission mode any interface related effects are suppressed. The approach of a true bulk measurement of angular dependent X-ray absorption for epitaxial films provides access to both magnetic and electronic anisotropies. The control experiment of the same sample in the cubic phase shows at least an order of magnitude smaller magnetic and spectral anisotropies. As illustrated the bulk magneto-crystalline anisotropy in Ni$_2$MnGa is caused by a varying occupation of electron states with d_{z^2} symmetry located predominantly at the Ni atom. On the other hand, the Ni orbital moment anisotropy is due to a varying occupation of electron states with d_{xy} symmetry. The measurement of the DOS for different magnetization directions in metals provides an alternative pathway to understand spin-orbit coupling and magnetic anisotropy in materials with itinerant electron states.

Chapter 8

Concluding remarks

Within this thesis magnetic and electronic properties of Heusler alloys as polycrystalline bulk materials and in the form of epitaxial thin films were investigated. The focus lies on polycrystalline Co_2TiZ (Z = Si, Ge, Sn, and Sb), $Co_2(Mn_xTi_{1-x})Si$, $Co_2(Mn_xTi_{1-x})Ge$, $Co_2Mn(Ga_{1-x}Ge_x)$, $Co_2(Mn_xTi_{1-x})Sn$, and $Co_2(Mn_{0.5}Dy_{0.5})Sn$ bulk Heusler alloys and Mn_2VAl, Co_2FeAl, and Ni_2MnGa thin film samples. These Heusler compounds provide very interesting physical properties for future applications in the fields of spintronics, thermoelectrics and shape memory alloys. Currently, Heusler compounds are already being integrated in magnetic sensor devices based on tunnel magnetoresistance devices. Two spectroscopical key methods were used: Magnetic circular dichroism in X-ray absorption (XAS/XMCD) and energy dispersive X-ray spectroscopy in combination with a scanning electron microscope (SEM/EDX).

The SEM/EDX system was used to check the homogeneity and the stoichiometry of the bulk samples. Most of the samples show the desired homogeneous composition. However, $Co_2(Mn_xTi_{1-x})Si$, $Co_2(Mn_xTi_{1-x})Sn$, and $Co_2(Mn_{0.5}Dy_{0.5})Sn$ show a surprising phase decomposition, that is not easily detectable by X-ray diffraction alone. On the one hand the phase separation is unwanted for spintronic applications. On the other hand it can be utilized to improve material properties for thermoelectric applications. In the case of $Co_2(Mn_xTi_{1-x})Sn$, and especially, $Co_2(Mn_{0.5}Dy_{0.5})Sn$ which shows an enchanting decomposition pattern with sixfold symmetry opening a new way to optimize the thermal to conductive resistivity ratio as discussed in Chap. 3.

In Chap. 4 element-specific magnetic moments and the spin-resolved unoccupied density of states of polycrystalline Co_2TiZ (Z = Si, Ge, Sn, and Sb), $Co_2(Mn_xTi_{1-x})Si$ and $Co_2(Mn_xTi_{1-x})Ge$, $Co_2Mn(Ga_{1-x}Ge_x)$ Heusler alloys were investigated using XMCD. A small ($< 0.03\ \mu_B$/atom) Ti moment is oriented antiparallel and a large ($> 3\ \mu_B$/atom) Mn moment is oriented parallel to the Co moment of $\sim 1\ \mu_B$/atom in the ferrimagnetical $CoTiZ$ compounds. Orbital magnetic moments are increased for quaternary compounds compared to the corresponding ternary compounds with $x = 0$ or $x = 1$.

A detailed disentangling procedure to determine the unoccupied spin-resolved partial density of states from the XAS/XMCD data was discussed and applied to extract the unoccupied spin-resolved partial DOS at the Co atom from the XMCD data in the second part of Chap. 4. In the case of Co_2TiSi, Co_2TiGe and Co_2TiSn the Co minority DOS reveals a maximum at 0.5 eV above E_F and very low values at E_F in agreement with the expectation for half-metallic ferromagnetism. In contrast, Co_2TiSb shows a large minority DOS at the Fermi energy like a normal metal. A substitution of Ti by Mn in Co_2TiSi shifts the minority DOS maximum from 0.5 eV to 0.9 eV with respect to the Fermi energy. For the series $Co_2MnGa_{1-x}Ge_x$ a gradual shift of the minority DOS maximum was observed from 0.7 eV for $x = 1$ to 1.0 eV for $x = 0$, indicating half-metallic ferromagnetism for the whole series and was explained by the rigid band model.

In the series of half-metallic $Co_2(Mn_xTi_{1-x})Ge$ Heusler alloys, the element-specific magnetic moments remain almost independent on the composition. Therefore, a replacement of Ti by Mn results in an increase in magnetization. The increase in magnetization with increasing x follows the Slater-Pauling rule. The Fermi level decreases with respect to the minority band gap with increasing number of valence electrons. This counterintuitive behavior is qualitatively explained by a charge transfer model and quantitatively by *ab initio* band structure calculations.

The results, revealing the distribution of magnetic moments and the relative position of the Fermi energy as a function of the number of valence electrons, confirm the predicted possibility of tailoring the minority band gap using substitutional quaternary Heusler compounds.

Using XAS/XMCD element-specific magnetic moments and spin-resolved unoccupied PDOS were determined in Chap. 5 for Co, Fe, and Mn in the quaternary Heusler compounds CoFeMnZ (Z = Al, Ga; Si, Ge) with 1:1:1:1 composition. These compounds belong to a class of highly spin-polarized materials with cubic LiMgPdSn-Typ structure. Different structure models for the sublattice occupation leading to similar average magnetization values could be distinguished by comparison of element-specific moments with theory. The compounds form similar structures where Co, Fe, Mn, and Z occupy the X, X', Y, and Z sublattice of the related X_2YZ $L2_1$ Heusler structure, for which half-metallic behavior was predicted. The unoccupied partial DOS functions as derived from the XAS/XMCD spectra for Co, Fe, and Mn were compared to theoretical results. A good agreement was found for Co, and Fe, while Mn spectra reveal additional final state effects (multiplets). The many possible combinations in designing quaternary 1:1:1:1 Heusler compounds give enormous potential to tailor physical properties.

In Chap. 6 the temperature dependence of the element-specific magnetic moments and of the spin-resolved unoccupied PDOS in ferromagnetic Co_2FeAl, and ferrimagnetic Mn_2VAl epitaxial thin films on MgO(100) were discussed. Interface and bulk properties show different results in the case of Mn_2VAl, while they are equal in the case of Co_2FeAl. The bulk related PDOS shows an unexpected strong temperature dependence beyond the changes expected from the temperature dependence of the Fermi distribution function. An increase of spectral weight was observed for majority states with a maximum below the Fermi energy in the case of Mn_2VAl and for minority states with a maximum above the Fermi energy in the case of Co_2FeAl. This temperature dependence is tentatively explained by a many-particle electron-correlation effect. Reduced atomic order near the interface leads to smaller magnetic moments at the interface and suppresses the unexpected temperature dependence of the DOS for Mn_2VAl. In the case of Co_2FeAl no difference between bulk and interface related DOS spectra was observed.

Ni_2MnGa investigated in Chap. 7 is a smart magnetic shape memory alloy and can be deployed in microelectronical and micromechanical devices. Angular dependent transmission XAS/XMCD measurements on epitaxial $Ni_2MnGa(101)/MgO(001)$ magnetic shape memory films reveals an anisotropy in the Ni dichroism intensities for magnetization aligned parallel and perpendicular to the film plane. The anisotropy is related to an anisotropy of the orbital magnetic moment in agreement with the observed out-of-plane magnetocrystalline anisotropy. The spectral variation of the X-ray absorption could be traced back to changes in the spin-projected density of states when the magnetization vector is rotated from the easy to the hard magnetic axis. A density of states peak with $d_{3z^2-r^2}$ symmetry located at the Fermi energy for easy axis magnetization narrows when the magnetization is rotated into the hard axis, thus increasing the mean kinetic energy of the half-filled band. This is the origin of the large magnetic anisotropy in Ni_2MnGa, which is essential for the twin boundary motion resulting in a macroscopic strain.

The main spectroscopical method XAS/XMCD utilized in this thesis is an important experimental tool to characterize element-specific magnetic and electronic properties of intermetallic materials. In combination with theoretical models, as demonstrated in this work, the method generates an improved understanding of the complex physical properties of alloys. It was shown how this knowledge can be used to optimize the desired properties of advanced functional materials.

Bibliography

[AEN02] A. Ayuela, J. Enkovaara, and R. M. Nieminen. Ab initio study of tetragonal variants in Ni_2MnGa alloy. *J. Phys.: Condens. Matter*, 14:5325, 2002.

[AJ11] E. Arbelo-Jorge. *Band structure of Heusler compounds studied by photoemission and tunneling spectroscopy*. PhD thesis, Johannes Gutenberg-Universität Mainz, 2011.

[AOF$^+$11] V. Alijani, S. Ouardi, G. H. Fecher, J. Winterlik, S. S. Naghavi, X. Kozina, G. Stryganyuk, C. Felser, E. Ikenaga, Y. Yamashita, S. Ueda, and K. Kobayashi. Electronic, structural, and magnetic properties of the half-metallic ferromagnetic quaternary Heusler compounds CoFeMnZ (Z = Al, Ga, Si, Ge). *Phys. Rev. B*, 84:224416, 2011.

[ASE$^+$07] C. Andersson, B. Sanyal, O. Eriksson, L. Nordström, O. Karis, D. Arvanitis, T. Konishi, E. Holub-Krappe, and J. Hunter Dunn. Influence of Ligand States on the Relationship between Orbital Moment and Magnetocrystalline Anisotropy. *Phys. Rev. Lett.*, 99:177207, Oct 2007.

[ASU02] N. Lanska A. Sozinov, A. A. Likhachev and K. Ullakko. Giant magnetic-field-induced strain in NiMnGa seven-layered martensitic phase. *Appl. Phys. Lett.*, 80:1746, 2002.

[BASY05] L. V. Bekenov, V. N. Antonov, A. P. Shpak, and A. N. Yaresko. Electronic structure and excited-state properties of Co_2TiSn and Co_2ZrSn from ab initio calculations. *Condens. Matter Phys.*, 8:565–577, 2005.

[BFB$^+$10] J. Barth, G. H. Fecher, B. Balke, S. Ouardi, T. Graf, C. Felser, A. Shkabko, A. Weidenkaff, P. Klaer, H. J. Elmers, H. Yoshikawa, S. Ueda, and K. Kobayashi. Itinerant half-metallic ferromagnets Co_2TiZ (Z=Si, Ge, Sn): Ab initio calculations and measurement of the electronic structure and transport properties. *Phys. Rev. B*, 81:064404, 2010.

[BFB$^+$11] J. Barth, G. H. Fecher, B. Balke, T. Graf, A. Shkabko, A. Weidenkaff P. Klaer, M. Kallmayer, H.-J. Elmers, H. Yoshikawa,

S. Ueda, K. Kobayashi, and C. Felser. Anomalous transport properties of the half-metallic ferromagnets Co_2TiSi, Co_2TiGe and Co_2TiSn. *Phil. Trans. R. Soc. A*, 369:3588, 2011.

[BFF07] B. Balke, G. H. Fecher, and C Felser. Structural and magnetic properties of $Co_2FeAl_{1-x}Si_x$. *Appl. Phys. Lett.*, 90:242503, 2007.

[BFKF06] B. Balke, G. H. Fecher, H. C. Kandpal, and C. Felser. Properties of the quaternary half-metal-type Heusler alloy $Co_2Mn_{1-x}Fe_xSi$. *Phys. Rev. B*, 74:104405, 2006.

[BGK$^+$99] M. Bode, M. Getzlaff, A. Kubetzka, R. Pascal, O. Pietzsch, and R. Wiesendanger. Temperature-Dependent Exchange Splitting of a Surface State on a Local-Moment Magnet: Tb(0001). *Phys. Rev. Lett.*, 83:3017, 1999.

[Bia82] A. Bianconi. Multiplet splitting of final-state configurations in x-ray-absorption spectrum of metal VO_2: Effect of core-hole-screening, electron correlation, and metal-insulator transition. *Phys. Rev. B*, 26:2741, 1982.

[Bru89] P. Bruno. Tight-binding approach to the orbital magnetic moment and magnetocrystalline anisotropy of transition-metal monolayers. *Phys. Rev. B*, 39:865, 1989.

[BSM$^+$01] P. Blaha, K. Schwarz, G. K. H. Madsen, D. Kvasnicka, and J. Luitz. *WIEN2k, An Augmented Plane Wave + Local Orbitals Program for Calculating Crystal Properties.* Karlheinz Schwarz, Techn. Universitaet Wien, Wien, Austria, 2001.

[BWF$^+$08] B. Balke, S. Wurmehl, G. H. Fecher, C. Felser, and J. Kübler. Rational design of new materials for spintronics: Co_2FeZ (Z = Al, Ga, Si, Ge). *Sci. Technol. Adv. Mater.*, 9:014102, 2008.

[CAKL09] L. Chioncel, E. Arrigoni, M. I. Katsnelson, and A. I. Lichtenstein. Majority-spin nonquasiparticle states in half-metallic ferrimagnet Mn_2VAl. *Phys. Rev. B*, 79:125123, 2009.

[CFF$^+$09] S. Chadov, G. H. Fecher, C. Felser, J. Minár, J. Braun, and H. Ebert. Electron correlations in $Co_2Mn_{1-x}Fe_xSi$ Heusler compounds. *J. Phys. D*, 42:2009, 2009.

[CGB$^+$10] V. A. Chernenko, V. Golub, J. M. Barandiarán, O. Y. Salyuk, F. Albertini, L. Righi, S. Fabbrici, and M. Ohtsuka. Magnetic anisotropies in Ni-Mn-Ga films on MgO(001) substrates. *Appl. Phys. Lett.*, 96:042502, 2010.

[CIL$^+$95] C. T. Chen, Y. U. Idzerda, H.-J. Lin, N. V. Smith, G. Meigs, E. Chaban, G. H. Ho, E. Pellegrin, and F. Sette. Experimental Confirmation of the X-Ray Magnetic Circular Dichroism Sum Rules for Iron and Cobalt. *Phys. Rev. Lett*, 75:152, 1995.

[Cow81] R. D. Cowan. *The theory of atomic structure and spectra*. Los Alamos Series in Basic and Applied Sciences, Berkeley: University of California Press, 1981.

[CPR06] X.-Q. Chen, R. Podloucky, and P. Rogl. Ab initio prediction of half-metallic properties for the ferromagnetic Heusler alloys $\mathrm{Co_2}M\mathrm{Si}$ (M=Ti,V,Cr). *J. Appl. Phys.*, 100:113901, 2006.

[CSA+08] L. Chioncel, Y. Sakuraba, E. Arrigoni, M. I. Katsnelson, M. Oogane, Y. Ando, T. Miyazaki, E. Burzo, and A. I. Lichtenstein. Nonquasiparticle States in $\mathrm{Co_2MnSi}$ Evidenced through Magnetic Tunnel Junction Spectroscopy Measurements. *Phys. Rev. Lett.*, 100:086402, 2008.

[CTAW93] P. Carra, B. T. Thole, M. Altarelli, and X. Wang. X-ray circular dichroism and local magnetic fields. *Phys. Rev. Lett.*, 70:694–697, 1993.

[dG05] F. de Groot. Multiple effects in X-ray spectroscopy. *Coordination Chemistry Reviews*, 249:31, 2005.

[dGFTS90] F. M. F. de Groot, J. C. Fuggle, B. T. Thole, and G. A. Sawatzky. 2p x-ray absorption of 3d transition-metal compounds: An atomic multiplet description including the crystal field. *Phys. Rev. B*, 42:5459, 1990.

[dGK08] Frank de Groot and Akio Kotani. *Core Level Spectroscopy of Solids*. CRC Press, 2008.

[DGvdL+97] H. A. Dürr, G. Y. Guo, G. van der Laan, J. Lee, G. Laufhoff, and J. A. C. Bland. Element-Specific Magnetic Anisotropy Determined by Transverse Magnetic Circular X-ray Dichroism. *Science*, 277:213, 1997.

[DLF+09] X. Dai, G. Liu, G. H. Fecher, C. Felser, Y. Li, and H. Liu. New quarternary half metallic material CoFeMnSi. *J. Appl. Phys.*, 105:07E901, 2009.

[EANN02] J. Enkovaara, A. Ayuela, L. Nordström, and R. M. Nieminen. Magnetic anisotropy in $\mathrm{Ni_2MnGa}$. *Phys. Rev. B*, 65:134422, 2002.

[EB97] A. Elshabini and F. D. Barlow. *Thin film technology handbook*. New York: McGraw-Hill, 1997.

[Ebe99] H. Ebert. Fully Relativistic Band Structure Calculations for Magnetic Solids - Formalism and Application. In H. Dreysee, editor, *Electronic Structure and Physical Properties of Solids. The Use of the LMTO Method*, volume 535 of *Lecture Notes in Physics*, page 191. Springer-Verlag, Berlin, Heidelberg, 1999.

[Ebe05] H. Ebert. The Munich SPR-KKR package, Version 3.6, 2005.

[EBK$^+$06] P. Entel, V. D. Buchelnikov, V. V. Khovailo, A. T. Zayak, W. A. Adeagbo, M. E. Gruner, H. C. Herper, and E. F. Wassermann. Modelling the phase diagram of magnetic shape memory Heusler alloys. *J. Phys. D*, 39:865, 2006.

[EFJ$^+$05] K. W. Edmonds, N. R. S. Farley, T. K. Johal, G. van der Laan, R. P. Campion, B. L. Gallagher, and C. T. Foxon. Ferromagnetic moment and antiferromagnetic coupling in (Ga,Mn)As thin films. *Phys. Rev. B*, 71:064418, 2005.

[EFV$^+$03] H. J. Elmers, G. H. Fecher, D. Valdaitsev, S. A. Nepijko, A. Gloskovskii, G. Jakob, G. Schönhense, S. Wurmehl, T. Block, C. Felser, P. C. Hsu, W. L. Tsai, and S. Cramm. Element-specific magnetic moments from core-absorption magnetic circular dichroism of the doped Heusler alloy $Co_2Cr_{0.6}Fe_{0.4}Al$. *Phys. Rev. B*, 67:104412, 2003.

[Eic11] T. Eichhorn. *Microstructure of epitaxial thin films of the ferromagnetic shape memory alloy* Ni_2MnGa. PhD thesis, Johannes Gutenberg-Universität Mainz, 2011.

[EMP01] H. Ebert, J. Minár, and V. Popescu. Magnetic Dichroism in Electron Spectroscopy. In K. Baberschke, M. Donath, and W. Nolting, editors, *Band-Ferromagnetism*, volume 580 of *Lecture Notes in Physics*, page 371. Springer-Verlag, Berlin, Heidelberg, 2001.

[ES75] J. L. Erskine and E. A. Stern. Calculation of the M_{23} magneto-optical absorption spectrum of ferromagnetic nickel. *Phys. Rev. B*, 12:5016–5024, 1975.

[FBO$^+$07] G. H. Fecher, B. Balke, S. Ouardi, C. Felser, G. Schönhense, E. Ikenaga, J.-J. Kim, S. Ueda, and K. Kobayashi. High energy, high resolution photoelectron spectroscopy of $Co_2Mn_{1-x}Fe_xSi$. *J. Phys. D*, 40:1576, 2007.

[FFB07] C. Felser, G. H. Fecher, and B. Balke. Spintronics: A Challenge for Materials Science and Solid-State Chemistry. *Angew. Chem. Int. Ed.*, 46:668, 2007.

[FKW$^+$05] G. H. Fecher, H. C. Kandpal, S. Wurmehl, J. Morais, H.-J. Lin, H. J. Elmers, G. Schönhense, and C. Felser. Design of magnetic materials: the electronic structure of the ordered, doped Heusler compound $Co_2Cr_{1-x}Fe_xAl$. *J. Phys.: Condens. Matter*, 17:7237, 2005.

[Fri62] J. Friedel. Sur la structure electronique et les proprietes magnetiques des métaux et alliages de transition. *J. Phys. Radium*, 23:501, 1962.

[GBB+10] T. Graf, J. Barth, C. G. F. Blum, B. Balke, C. Felser, P. Klaer, and H. J. Elmers. Phase-separation-induced changes in the magnetic and transport properties of the quaternary Heusler alloy $Co_2Mn_{1-x}Tix$Sn. *Phys. Rev. B*, 82:194420, 2010.

[GBN+05] J. Grabis, A. Bergmann, A. Nefedov, K. Westerholt, and H. Zabel. Element-specific x-ray circular magnetic dichroism of Co_2MnGe Heusler thin films. *Phys. Rev. B*, 72:024437, 2005.

[GCW+09] T. Graf, F. Casper, J. Winterlik, B. Balke, G. H. Fecher, and C. Felser. Crystal Structure of New Heusler Compounds. *Z. Anorg. Allg. Chem.*, 635:976, 2009.

[GD08] M. Gilleßen and R. Dronskowski. A Combinatorial Study of Full Heusler Alloys by First-Principles Computational Methods. *Journal of Computational Chemistry*, 30:1290, 2008.

[GDG+02] P. Gambardella, S. S. Dhesi, S. Gardonio, C. Grazioli, P. Ohresser, and C. Carbone. Localized Magnetic States of Fe, Co, and Ni Impurities on Alkali Metal Films. *Phys. Rev. Lett.*, 88:047202, 2002.

[GDP02] I. Galanakis, P. H. Dederichs, and N. Papanikolaou. Slater-Pauling behavior and origin of the half-metallicity of the full-Heusler alloys. *Phys. Rev. B*, 66:174429, 2002.

[GEOR08] M. E. Gruner, P. Entel, I. Opahle, and M. Richter. Ab initio investigation of twin boundary motion in the magnetic shape memory Heusler alloy Ni_2MnGa. *J. Mater. Sci*, 43:3825, 2008.

[GFP11] T. Graf, C. Felser, and S. S. P. Parkin. Simple rules for the understanding of Heusler compounds. *Progress in Solid State Chemistry*, 39:1, 2011.

[GH07] Z. Gercsi and K. Hono. Ab initio predictions for the effect of disorder and quarternary alloying on the half-metallic properties of selected Co_2Fe-based Heusler alloys. *J. Phys.: Condens. Matter*, 19:326216, 2007.

[GKB+10] T. Graf, P. Klaer, J. Barth, B. Balke, H. J. Elmers, and C. Felser. Phase separation in the quaternary Heusler compound $CoT_{(1-x)}Mn_xSb$ - A reduction in the thermal conductivity for thermoelectric applications. *Scripta Materialia*, 63:1216, 2010.

[GMD06] I. Galanakis, Ph. Mavropoulos, and P. H. Dederichs. Electronic structure and Slater-Pauling behaviour in half-metallic Heusler alloys calculated from first principles. *J. Phys. D*, 39:765, 2006.

[Goe05] E. Goering. X-ray magnetic circular dichroism sum rule correction for the light transition metals. *Philosophical Magazine*, 85:2895–2911, 2005.

[GÖSA07] I. Galanakis, K. Özdogan, E. Sasioglu, and B. Aktas. Doping of Mn_2VAl and Mn_2VSi Heusler alloys as a route to half-metallic antiferromagnetism. *Phys. Rev. B*, 75:092407, 2007.

[GRC$^+$09] V. Golub, K. M. Reddy, V. Chernenko, P. Müllner, A. Punnoose, and M. Ohtsuka. Ferromagnetic resonance properties and anisotropy of Ni-Mn-Ga thin films of different thicknesses deposited on Si substrate. *J. Appl. Phys.*, 105:07A942, 2009.

[HAJ09] C. Herbort, E. Arbelo, and M. Jourdan. Morphology and magnetoresistance of $Co_2Cr_{0.6}Fe_{0.4}Al$-based tunnelling junctions. *J. Phys. D*, 42:084006, 2009.

[Heu03] F. Heusler. Über magneische Manganlegierungen. *dt. phys. Geselschaft*, 5:219, 1903.

[HHHJ06] M. C. Hickey, A. Husmann, S. N. Holmes, and G. A. C. Jones. Fermi surfaces and electronic structure of the Heusler alloy Co_2TiSn. *J. Phys.: Condens. Matter*, 18:2897, 2006.

[HKN$^+$10] R. Huber, P. Klemm, S. Neusser, B. Botters, A. Wittmann, M. Weiler, S.T.B. Goennenwein, C. Heyn, M. Schneider, P. Bönie, and D. Grundler. Advanced techniques for all-electrical spectroscopy on spin caloric phenomena. *Solid State Communications*, 150:492, 2010.

[HRS04] M. A. Hermann, W. Richter, and H. Sitter. *Epitaxy - Physical principles and technical implementations.* Heidelberg: Springer-Verlag, 2004.

[HTB$^+$08] O. Heczko, M. Thomas, J. Buschbeck, L. Schultz, and S. Fähler. Epitaxial Ni–Mn–Ga films deposited on $SrTiO_3$ and evidence of magnetically induced reorientation of martensitic variants at room temperature. *Appl. Phys. Lett.*, 92:072502, 2008.

[IAKI82] S. Ishida, S. Akazawa, Y. Kubo, and J. Ishida. Band theory of Co_2MnSn, Co_2TiSn and Co_2TiAl. *Journal of Physics F: Metal Physics*, 12:1111, 1982.

[IdGST09] H. Ikeno, F. M. F. de Groot, E. Stavitski, and I. Tanaka. Multiplet calculations of $L_{2,3}$ x-ray absorption near-edge structures for 3d transition-metal compounds. *J. Phys.: Condens. Matter*, 21:104208, 2009.

[IHiM$^+$08] T. Ishikawa, S. Hakamata, K. i. Matsuda, T. Uemura, and M. Yamamoto. Fabrication of fully epitaxial $Co_2MnSi/MgO/Co_2MnSi$ magnetic tunnel junctions. *J. Appl. Phys.*, 103:07A919, 2008.

[IIT$^+$08] K. Inomata, N. Ikeda, N. Tezuka, R. Goto, S. Sugimotoand M. Wojcik, and E. Jedryka. Highly spin-polarized materials and devices for spintronics. *Sci. Technol. Adv. Mater.*, 9:014101, 2008.

[IK05] V. Yu. Irkhin and M. I. Katsnelson. Non-quasiparticle states in the core level spectra of ferromagnetic semiconductors and half-metallic ferromagnets. *Eur. Phys. J. B*, 43:479, 2005.

[JE07] G. Jakob and H. J. Elmers. Epitaxial films of the magnetic shape memory material. *Journal of Magnetism and Magnetic Materials*, 310:2779, 2007.

[JEKE07] G. Jakob, T. Eichhorn, M. Kallmayer, and H. J. Elmers. Correlation of electronic structure and martensitic transition in epitaxial Ni_2MnGa films. *Phys. Rev. B*, 76:174407, 2007.

[JFB$^+$09] V. Jung, G. H. Fecher, B. Balke, V. Ksenofontov, and C. Felser. Electronic structure, magnetic properties and order-disorder phenomena in $Co_2Mn_{1-x}Fe_x$ Al. *J. Phys. D*, 42:084007, 2009.

[JHKF] C. G. F. Blum J. H. Kohlhepp, H. Swagten and C. Felser.

[Jul75] M. Jullière. Tunneling between ferromagnetic films. *Physics Letters A*, 54:225, 1975.

[JYM$^+$10] C. M. Jaworski, J. Yang, S. Mack, D. D. Awschalom, J. P. Heremans, and R. C. Myers. Observation of the spin-Seebeck effect in a ferromagnetic semiconductor. *Nature Materials*, 9:898, 2010.

[Kal11] M. Kallmayer. *Röntgenabsorptionsspektroskopie und magnetischer Röntgenzirkulardichroismus an dünnen Heusler-Filmen.* PhD thesis, Johannes Gutenberg-Universität Mainz, 2011.

[KE98] K. Koepernik and H. Eschrig. Full-potential nonorthogonal local-orbital minimum-basis band-structure scheme. *Phys. Rev. B*, 59:1743, 1998.

[KEB$^+$06] M. Kallmayer, H. J. Elmers, B. Balke, S. Wurmehl, F. Emmerling, G. H. Fecher, and C. Felser. Magnetic properties of $Co_2Mn_{1-x}Fe_xSi$ Heusler alloys. *J. Phys. D: Appl. Phys.*, 39:786, 2006.

[KFF07] H. C. Kandpal, G. H. Fecher, and C. Felser. Calculated electronic and magnetic properties of the half-metallic, transition metal based Heusler compounds. *J. Phys. D*, 40:1507, 2007.

[KIC$^+$08] M. I. Katsnelson, V. Yu. Irkhin, L. Chioncel, A. I. Lichtenstein, and R. A. de Groot. Half-metallic ferromagnets: From band structure to many-body effects. *Rev. Mod. Phys.*, 80:315, 2008.

[KKB$^+$08] F. Khelfaoui, M. Kohl, J. Buschbeck, O. Heczko, S. Fähler, and L. Schultz. A fabrication technology for epitaxial Ni-Mn-Ga microactuators. *Eur. Phys. J. Special Topics*, 158:167, 2008.

[KKE$^+$09] P. Klaer, M. Kallmayer, H. J. Elmers, L. Basit, J. Thöne, S. Chadov, and C. Felser. Localized magnetic moments in the Heusler alloy Rh_2MnGe. *J. Phys. D*, 42:084001, 2009.

[KKG$^+$08] M. Kohl, B. Krevet, T. Grund, J. Barth, D. Auernhammer, and F. Khelfaoui. Engineering Aspects of Shape Memory Film Actuators and Sensors. *Advances in Science and Technology*, 59:119, 2008.

[KKN$^+$09] T. Kubota, K. Kodama, T. Nakamura, Y. Sakuraba, M. Oogane, K. Takanashi, and Y. Ando. Ferrimagnetism in epitaxially grown Mn_2VAl Heusler alloy investigated by means of soft x-ray magnetic circular dichroism. *Appl. Phys. Lett.*, 95:222503, 2009.

[KKS$^+$09] M. Kallmayer, P. Klaer, H. Schneider, E. Arbelo-Jorge, C. Herbort, G. Jakob, M. Jourdan, and H. J. Elmers. Spin-resolved unoccupied density of states in epitaxial Heusler-alloy films. *Phys. Rev. B*, 80:020406(R), 2009.

[KKW$^+$07] H. C. Kandpal, V. Ksenofontov, M. Wojcik, R. Seshadri, and C. Felser. Electronic structure, magnetism and disorder in the Heusler compound Co_2TiSn. *J. Phys. D*, 40:1587, 2007.

[Kla] P. Klaer. *Röntgenzirkulardichroismus an Heusler-Volumenproben*, Diplomarbeit, Johannes Gutenberg-Universität Mainz, 2008.

[KPE$^+$09] M. Kallmayer, P. Pörsch, T. Eichhorn, H. Schneider, C. A. Jenkins, G. Jakob, and H. J .Elmers. Compositional dependence of element-specific magnetic moments in Ni_2MnGa films. *J. Phys. D*, 10342:084008, 2009.

[KRBD05] H. Kolev, G. Rangelov, J. Braun, and M. Donath. Reduced surface magnetization of NiMnSb(001). *Phys. Rev. B*, 72:104415, 2005.

[KRH$^+$10] S. Kaufmann, U. K. Rößler, O. Heczko, M. Wuttig, J. Buschbeck, L. Schultz, and S. Fähler. Adaptive Modulations of Martensites. *Phys. Rev. Lett.*, 104:145702, 2010.

[KTHR04] S. Kämmerer, A. Thomas, A. Hütten, and G. Reiss. Co_2MnSi Heusler alloy as magnetic electrodes in magnetic tunnel junctions. *Appl. Phys. Lett.*, 85:79, 2004.

[Küb83] J. Kübler. Formation and coupling of magnetic moments in Heusler alloys. *Phys. Rev. B*, 28:1745, 1983.

[Küb84] J. Kübler. First principle theory of metallic magnetism. *Physica B+C*, 127:257, 1984.

[Kuc02] W. Kuch. Abbildende magnetische Mikrospektroskopie. Habilitationsschrift, Matin-Luther-Universität Halle-Wittenberg, 2002.

[LLBS05] S. C. Lee, T. D. Lee, P. Blaha, and K. Schwarz. Magnetic and half-metallic properties of the full-Heusler alloys Co_2TiX X=(Al,Ga;Si,Ge,Sn;Sb). *J. Appl. Phys.*, 97:10C307, 2005.

[LMC$^+$09] C. Liu, C. K. A. Mewes, M. Chshiev, T. Mewes, and W. H. Butler. Origin of low Gilbert damping in half metals. *Appl. Phys. Lett.*, 95:022509, 2009.

[MIK$^+$03] K. Miyamoto, K. Ioria, A. Kimura, T. Xie, M. Taniguchi, S. Qiao, and K. Tsuchiya. Soft X-ray magnetic circular dichroism of Heusler-type alloy Co_2MnGe. *Solid State Communications*, 128:163, 2003.

[mis] The calculations have been performed with the program MISSING 1.1 by Riccardo Gusmeroli and Claudia Dallera and with the program CTM4XAS by Eli Stavitski and Frank de Groot. Both codes are based on Cowan's Hartree-Fock atomic code. http://www.tcd.ie/Physics/People/Cormac.McGuinness/Cowan/.

[MKI$^+$04] K. Miyamoto, A. Kimura, K. Iori, K. Sakamoto, T. Xie, T. Moko, S. Qiao, M. Taniguchi, and K. Tsuchiya. Element-resolved magnetic moments of Heusler-type ferromagnetic ternary alloy Co_2MnGe. *J. Phys.: Condens. Matter*, 16:S5797, 2004.

[MKM$^+$09] K. Miyamoto, A. Kimura, Y. Miura, M. Shirai, M. Ye, Y. Cui, K. Shimada, H. Namatame, M. Taniguchi, Y. Takeda, Y. Saitoh, E. Ikenaga, S. Ueda, K. Kobayashi, and T. Kanomata. Absence of temperature dependence of the valence-band spectrum of Co_2MnSi. *Phys. Rev. B*, 79:100405(R), 2009.

[MLH$^+$07] I. Matsuda, C. Liu, T. Hirahara, M. Ueno, T. Tanikawa, T. Kanagawa, R. Hobara, S. Yamazaki, S. Hasegawa, and K. Kobayashi. Electron-Phonon Interaction and Localization of Surface-State Carriers in a Metallic Monolayer. *Phys. Rev. Lett.*, 99:146805, 2007.

[MNS04] Y. Miura, K. Nagao, and M. Shirai. Atomic disorder effects on half-metallicity of the full-Heusler alloys $Co_2(Cr_{1-x}Fe_x)Al$: A first-principles study. *Phys. Rev. B*, 69:144413, 2004.

[MSW$^+$11] M. Meinert, J. Schmalhorst, H. Wulfmeier, G. Reiss, E. Arenholz, T. Graf, and C. Felser. Electronic structure of fully epitaxial Co_2TiSn thin films. *Phys. Rev. B*, 83:064412, 2011.

[NSI99] R. Nakajima, J. Stöhr, and Y. U. Idzerda. Electron-yield saturation effects in L-edge x-ray magnetic circular dichroism spectra of Fe, Co, and Ni. *Phys. Rev. B*, 59:6421–6429, 1999.

[OA02] R. C. O'Handley and S. M. Allen. *Encyclopedia of Smart Materials.* Wiley, New York, 2002.

[ÖAGS07] K. Özdogan, B. Aktas, I. Galanakis, and E. Sasioglu. Influence of mixing the low-valent transition metal atoms (Y, Y*= Cr, Mn, Fe) on the properties of the quaternary $Co_2[Y_{1-x}Y_x{}^*]Z$ (Z= Al, Ga, Si, Ge, or Sn) Heusler compounds. *J. Appl. Phys.*, 101:073910, 2007.

[O'H98] R. C. O'Handley. Model for strain and magnetization in magnetic shape-memory alloys. *J. Appl. Phys.*, 83:3263, 1998.

[Ohn10] H. Ohno. A window on the future of spintronics. *Nature Materials*, 9:952, 2010.

[OMS$^+$05] S. Okamura, A. Miyazaki, S. Sugimoto, N. Tezuka, and K. Inomata. Large tunnel magnetoresistance at room temperature with a Co_2FeAl full-Heusler alloy electrode. *Appl. Phys. Lett.*, 86:232503, 2005.

[OMS$^+$08] C. P. Opeil, B. Mihaila, R. K. Schulze, L. Mañosa, A. Planes, W. L. Hults, R. A. Fisher, P. S. Riseborough, P. B. Littlewood, J. L. Smith, and J. C. Lashley. Combined experimental and theoretical investigation of the premartensitic transition in Ni_2MnGa. *Phys. Rev. Lett.*, 100:165703, 2008.

[ÖSAG06] K. Özdogan, E. Sasioglu, B. Aktas, and I. Galanakis. Doping and disorder in the Co_2MnAl and Co_2MnGa half-metallic Heusler alloys. *Phys. Rev. B*, 74:172412, 2006.

[Ots98] K. Otsuka. *Shape Memory Materials.* Cambridge University Press, Cambridge, England, 1998.

[PBE96] J. P. Perdew, K. Burke, and M. Ernzerhof. *Phys. Rev. Lett.*, 77:3865, 1996.

[PCF02] S. Picozzi, A. Continenza, and A. J. Freeman. Co_2MnX (X =Si, Ge, Sn) Heusler compounds: An *ab initio* study of their structural, electronic, and magnetic properties at zero and elevated pressure. *Phys. Rev. B*, 66:094421, 2002.

[PCF04] S. Picozzi, A. Continenza, and A. J. Freeman. Role of structural defects on the half-metallic character of Co_2MnGe and Co_2MnSi Heusler alloys. *Phys. Rev. B*, 69:094423, 2004.

[PKE$^+$08] P. Pörsch, M. Kallmayer, T. Eichhorn, G. Jakob, H. J. Elmers, C. A. Jenkins, C. Felser, R. Ramesh, and M. Huth. Suppression of martensitic phase transition at the Ni_2MnGa film surface. *Appl. Phys. Lett.*, 93:022501, 2008.

[Rei85] Ludwig Reimer. *Scanning electron microscopy.* Springer, 1985.

[RKTH07] A. Rajanikanth, D. Kande, Y. K. Takahashi, and K. Hono. High spin polarization in a two phase quaternary Heusler alloy $Co_2MnAl_xSn_{1-x}$. *J. Appl. Phys.*, 101:09J508, 2007.

[RS08] D.C. Ralph and M.D. Stiles. Spin transfer torques. *Journal of Magnetism and Magnetic Materials*, 320:1190, 2008.

[Sch94] Peter Fritz Schmidt. *Praxis der Rasterelektronenmikroskopie und Mikrobereichsanalyse*. Expert-Verlag, 1994.

[SEN+10] O. Schebaum, D. Ebke, A. Niemeyer, Günter Reiss, J. S. Moodera, and A. Thomas. Direct measurement of the spin polarization of Co_2FeAl in combination with MgO tunnel barriers. *J. Appl. Phys.*, 107:09C717, 2010.

[SEW+08] J. Schmalhorst, D. Ebke, A. Weddemann, A. Hütten, A. Thomas, G. Reiss, A. Turchanin, A. Gölzhäuser, B. Balke, and C. Felser. On the influence of bandstructure on transport properties of magnetic tunnel junctions with $Co_2Mn_{1-x}Fe_xSi$ single and multilayer electrode. *J. Appl. Phys.*, 104:043918, 2008.

[SHO+06] Y. Sakuraba, M. Hattori, M. Oogane, Y. Ando, H. Kato, A. Sakuma, T. Miyazaki, and H. Kubota. Giant tunneling magnetoresistance in Co_2MnSi/Al-O/Co_2MnSi magnetic tunnel junctions. *Appl. Phys. Lett.*, 88:192508, 2006.

[SJK+06] H. Schneider, G. Jakob, M. Kallmayer, H. J. Elmers, M. Cinchetti, B. Balke, S. Wurmehl, C. Felser, M. Aeschlimann, and H. Adrian. Epitaxial film growth and magnetic properties of Co_2FeSi. *Phys. Rev. B*, 74:174426, 2006.

[SKS+04] J. Schmalhorst, S. Kämmerer, M. Sacher, G. Reiss, A. Hütten, and A. Scholl. Interface structure and magnetism of magnetic tunnel junctions with a Co_2MnSi electrode. *Phys. Rev. B*, 70:024426, 2004.

[SRK+06] M. Sargolzaei, M. Richter, K. Koepernik, I. Opahle, H. Eschrig, and I. Chaplygin. Spin and orbital magnetism in full Heusler alloys: A density functional theory study of Co_2YZ (Y = Mn,Fe; Z = Al,Si,Ga,Ge). *Phys. Rev. B*, 74:224410, 2006.

[SSO+12] M. Schwall, L. M. Schoop, S. Ouardi, B. Balke, C. Felser, P. Klaer, and H. J. Elmers. Thermomagnetic Properties Improved by Self-Organized Flower-Like Phase Separation of Ferromagnetic $Co_2Dy_{0.5}Mn_{0.5}Sn$. *Advanced Functional Materials*, 2012.

[SSW+09] R. Shan, H. Sukegawa, W. H. Wang, M. Kodzuka, T. Furubayashi, T. Ohkubo, S. Mitani, K. Inomata, and K. Hono. Demonstration of half-metallicity in Fermi-level-tuned Heusler alloy $Co_2FeAl_{0.5}Si_{0.5}$ at room temperature. *Phys. Rev. Lett.*, 102:246601, 2009.

[STK+10] Y. Sakuraba, K. Takanashi, Y. Kota, T. Kubota, M. Oogane, A. Sakuma, and Y. Ando. Evidence of Fermi level control in a half-metallic Heusler compound Co_2MnSi by Al-doping: Comparison of measurements with first-principles calculations. *Phys. Rev. B*, 81:144422, 2010.

[Stö95] J. Stöhr. X-ray magnetic circular dichroism spectroscopy of transition metal thin films. *Journal of Electron Spectroscopy and Related Phenomena*, 75:253, 1995.

[Stö99] J. Stöhr. Exploring the microscopic origin of magnetic anisotropies with X-ray magnetic circular dichroism (XMCD) spectroscopy - Condens. Matter. *Journal of Magnetism and Magnetic Materials*, 200:470, 1999.

[SWB04] A. Scherz, H. Wende, and K. Baberschke. Fine structure of X-ray magnetic circular dichroism for early 3 d transition metals. *Appl. Phys. A: Materials Science & Processing*, 78:843, 2004.

[SWW+87] G. Schütz, W. Wagner, W. Wilhelm, P. Kienle, R. Zeller, R. Frahm, and G. Materlik. Absorption of circularly polarized x-rays in iron. *Phys. Rev. Lett.*, 58:737–740, 1987.

[TCSvdL92] B. T. Thole, P. Carra, F. Sette, and G. van der Laan. X-ray circular dichroism as a probe of orbital magnetization. *Phys. Rev. Lett.*, 68:1943–1946, 1992.

[THB+09] M. Thomas, O. Heczko, J. Buschbeck, Y. W. Lai, J. McCord, S. Kaufmann, L. Schultz, and S. Fähler. Stray-Field-Induced Actuation of Free-Standing Magnetic Shape-Memory Films. *Adv. Materials*, 21:3708, 2009.

[TII+09] T. Taira, T. Ishikawa, N. Itabashi, K. i. Matsuda, T. Uemura, and M. Yamamoto. Spin-dependent tunnelling characteristics of fully epitaxial magnetic tunnel junctions with a Heusler alloy Co_2MnGe thin film and a MgO barrier. *J. Phys. D*, 42:084015, 2009.

[TIMS09] N. Tezuka, N. Ikeda, F. Mitsuhashi, and S. Sugimoto. Improved tunnel magnetoresistance of magnetic tunnel junctions with Heusler $Co_2FeAl_{0.5}Si_{0.5}$ electrodes fabricated by molecular beam epitaxy. *Appl. Phys. Lett.*, 94:162504, 2009.

[TISI07] N. Tezuka, N. Ikeda, S. Sugimoto, and K. Inomata. Giant Tunnel Magnetoresistance at Room Temperature for Junctions using Full-Heusler $Co_2FeAl_{0.5}Si_{0.5}$ Electrodes. *Jpn. J. Appl. Phys.*, 46:L454, 2007.

[TKvdL+06] N. D. Telling, P. S. Keatley, G. van der Laan, R. J. Hicken, E. Arenholz, Y. Sakuraba, M. Oogane, Y. Ando, and T. Miyazaki. Interfacial structure and half-metallic ferromagnetism in Co_2MnSi-based magnetic tunnel junctions. *Phys. Rev. B*, 74:224439, 2006.

[TKvdL+08] N. D. Telling, P. S. Keatley, G. van der Laan, R. J. Hicken, E. Arenholz, Y. Sakuraba, M. Oogane, Y. Ando, K. Takanashi, A. Sakuma, and T. Miyazaki. Evidence of local moment formation in Co-based Heusler alloys. *Phys. Rev. B*, 78:184438, 2008.

[TNMS05] A. Thiaville, Y. Nakatani, J. Miltat, and Y. Suzuki. Micromagnetic understanding of current-driven domain wall motion in patterned nanowires. *EPL*, 69(6):990, 2005.

[TSO+08] S. Tsunegi, Y. Sakuraba, M. Oogane, K. Takanashi, and Y. Ando. Large tunnel magnetoresistance in magnetic tunnel junctions using a Co_2MnSi Heusler alloy electrode and a MgO barrier. *Appl. Phys. Lett.*, 93:112506, 2008.

[TSS94] S. Tewari, R. Shah, and H. Song. Effect of magnetic field on the microstructure and macrosegregation in directionally solidified Pb-Sn alloys. *Metallurgical and Materials Transactions A*, 25:1535, 1994.

[UHK+96] K. Ullakko, J. K. Huang, C. Kantner, R. C. O'Handley, and V. V. Kokorin. Large magnetic-field-induced strains in Ni_2MnGa single. *Appl. Phys. Lett.*, 69:1966, 1996.

[UHKO97] K. Ullakko, J. K. Huang, V. V. Kokorin, and R. C. O'Handley. Magnetically controlled shape memory effect in Ni2MnGa intermetallics. *Scripta Materialia*, 36(10):1133 – 1138, 1997.

[UHN+09] M. A. Uijttewaal, T. Hickel, J. Neugebauer, M. E. Gruner, and P. Entel. Understanding the phase transitions of the Ni_2MnGa magnetic shape memory system from first principles. *Phys. Rev. Lett.*, 102:035702, 2009.

[UTH+08] K. Uchida, S. Takahashi, K. Harii, J. Ieda, W. Koshibae, K. Ando, S. Maekawa, and E. Saitoh. Observation of the spin Seebeck effect. *Nature*, 455:778, 2008.

[UYH+99] C. Uher, J. Yang, S. Hu, D. T. Morelli, and G. P. Meisner. Transport properties of pure and doped MNiSn (M =Zr, Hf). *Phys. Rev. B*, 59:8615, 1999.

[vJS04] I. Žutić, F. Jaroslav, and S. D. Sarma. Spintronics: Fundamentals and applications. *Rev. Mod. Phys.*, 76:323–410, 2004.

[WCvA+90] P. J. W. Weijs, M. T. Czyzyk, J. F. van Acker, W. Speier, J. B. Goedkoop, H. van Leuken, H. J. M. Hendrix, R. A. de Groot, G. van der Laan, K. H. J. Buschow, G. Wiech, and J. C. Fuggle. Core-hole effects in the x-ray-absorption spectra of transition-metal silicides. *Phys. Rev. B*, 41:11899, 1990.

[WFK+06] S. Wurmehl, G. H. Fecher, K. Kroth, F. Kronast, H. A. Dürr, Y. Takeda, Y. Saitoh, K. Kobayashi, H.-J. Lin, G. Schönhense, and

C. Felser. Electronic structure and spectroscopy of the quaternary Heusler alloy $Co_2Cr_{1-x}Fe_xAl$. *J. Phys. D*, 39:803, 2006.

[Whi06] George M. Whiteside. The origins and the future of microfluidics. *Nature*, 442:368, 2006.

[WJZ$^+$07] S. A. Wilson, R. P. J. Jourdain, Q. Zhang, R. A. Dorey, C. R. Bowen, M. Willander, Q. U. Wahab, M. Willander, S. M. Al-hilli, O. Nur, E. Quandt, C. Johansson, E. Pagounis, M. Kohl, J. Matovic, B. Samel, W. van der Wijngaart, E. W. H. Jager, D. Carlsson, Z. Djinovic, M. Wegener, C. Moldovan, R. Iosub, E. Abad, M. Wendlandt, C. Rusu, and K. Persson. New materials for micro-scale sensors and actuators: An engineering review. *Materials Science and Engineering: R: Reports*, 56(1–6):1, 2007.

[WLK$^+$10] W. Wang, E. Liu, M. Kodzuka, H. Sukegawa, M. Wojcik, E. Jedryka, G. H. Wu, K. Inomata, S. Mitani, and K. Hono. Coherent tunneling and giant tunneling magnetoresistance in Co_2FeAl/MgO/CoFe magnetic tunneling junctions. *Phys. Rev. B*, 81:140402, 2010.

[WP99] R. Weht and W. E. Pickett. Half-metallic ferrimagnetism in Mn_2VAl. *Phys. Rev. B*, 60:13006, 1999.

[WPK$^+$05] W. H. Wang, M. Przybylski, W. Kuch, L. I. Chelaru, J. Wang, Y. F. Lu, J. Barthel, H. L. Meyerheim, and J. Kirschner. Magnetic properties and spin polarization of Co_2MnSi Heusler alloy thin films epitaxially grown on GaAs(001). *Phys. Rev. B*, 71:144416, 2005.

[WSN$^+$95] D. Weller, J. Stöhr, R. Nakajima, A. Carl, M. G. Samant, C. Chappert, R. Mégy, P. Beauvillain, P. Veillet, and G. A. Held. Microscopic origin of magnetic anisotropy in Au/Co/Au probed with X-ray magnetic circular dichroism. *Phys. Rev. Lett.*, 75:3752, 1995.

[WSS$^+$08] W. Wang, H. Sukegawa, R. Shan, T. Furubayashi, and K. Inomata. Preparation and characterization of highly L2(1)-ordered full-Heusler alloy $Co_2FeAl_{0.5}Si_{0.5}$ thin films for spintronics device applications. *Appl. Phys. Lett.*, 92:221912, 2008.

[WSS$^+$09] W. Wang, H. Sukegawa, R. Shan, S. Mitani, and K. Inomata. Giant tunneling magnetoresistance up to 330% at room temperature in sputter deposited Co_2FeAl/MgO/CoFe magnetic tunnel junctions. *Appl. Phys. Lett.*, 95:182502, 2009.

[WSSI08] W. Wang, H. Sukegawa, R. Shan, and K. Inomata. Fabrication of fully epitaxial magnetic tunnel junctions using $L2_1$-ordered $Co_2FeAl_{0.5}Si_{0.5}$ electrodes and their tunneling magnetoresistance characteristics. *Appl. Phys. Lett.*, 93:122506, 2008.

[YIA$^+$02] A. Yamasaki, S. Imada, R. Arai, H. Utsunomiya, S. Suga, T. Muro, Y. Saitoh, T. Kanomata, and S. Ishida. Orbital angular momentum and interpretation of core-absorption magnetic circular dichroism on the band picture in Co-based Heusler alloys Co_2YSn (Y = Ti, Zr, and Nb). *Phys. Rev. B*, 65:104410, 2002.

[YMI$^+$06] M. Yamamoto, T. Marukame, T. Ishikawa, K. Matsuda, T. Uemura, and M. Arita. Fabrication of fully epitaxial magnetic tunnel junctions using cobalt-based full-Heusler alloy thin film and their tunnel magnetoresistance characteristics. *J. Phys. D*, 39:824, 2006.

Hiermit versichere ich, dass ich die vorliegende Dissertation selbständig verfasst und keine anderen als die angegebenen Hilfsmittel benutzt habe. Alle der Literatur entnommenen Stellen sind als solche gekennzeichnet.

Mainz, den 15. April 2012

Peter Klaer